Stability Transformation:
A Tool to Solve Nonlinear Problems

Detlef Pingel [1,•] Peter Schmelcher [1,2,*] Fotis K. Diakonos [3,†]

June 3, 2003

PACS number: 05.45.Ac, 02.60.Cb

keywords: periodic orbits, stabilization, chaos, nonlinear dynamics, strange attractor, iterated maps, root finding, Hamiltonian systems, Markov partitions, nonlinear partial differential equations

---

[1] Theoretische Chemie, Institut für Physikalische Chemie, INF 229, 69120 Heidelberg, Germany

[2] Physikalisches Institut, Philosophenweg 12, Universität Heidelberg, 69120 Heidelberg, Germany

[3] Department of Physics, University of Athens, GR-15771 Athens, Greece

• detlef.pingel@tc.pci.uni-heidelberg.de

* peter.schmelcher@tc.pci.uni-heidelberg.de

† fdiakono@cc.uoa.gr

Abstract

We present an analysis of the properties as well as the diverse applications and extensions of the method of stabilisation transformation. This method was originally invented to detect unstable periodic orbits in chaotic dynamical systems. Its working principle is to change the stability characteristics of the periodic orbits by applying an appropriate global transformation of the dynamical system. The theoretical foundations and the associated algorithms for the numerical implementation of the method are discussed. This includes a geometrical classification of the periodic orbits according to their behaviour when the stabilisation transformations are applied. Several refinements concerning the implementation of the method in order to increase the numerical efficiency allow the detection of complete sets of unstable periodic orbits in a large class of dynamical systems. The selective detection of unstable periodic orbits according to certain stability properties and the extension of the method to time series are discussed. Unstable periodic orbits in continuous–time dynamical systems are detected via introduction of appropriate Poincaré surfaces of section. Applications are given for a number of examples including the classical Hamiltonian systems of the hydrogen and helium atom, respectively, in electromagnetic fields. The universal potential of the method is demonstrated by extensions to several other nonlinear problems that can be traced back to the detection of fixed points. Examples include the integration of nonlinear partial differential equations and the numerical determination of Markov–partitions of one-parametric maps.

Contents

1 Introduction

1.1 General remarks on nonlinear systems

The manifestations of nonlinearity and their extraction is the thread running through this reviewing article. Nonlinearity is best understood when opposed to its negation: Linearity. Mathematically spoken the latter implies the properties of additivity and homogeneity. A consequence of linearity is linear superposition: With two solutions ψ and χ both fulfilling the same linear equation a linear superposition of ψ and χ also fulfils it. Therefore an infinity of solutions can be constructed once a finite set of solutions is known. In nonlinear systems the superposition principle is lost. Two different solutions of the system are rarely related to each other and can in particular not be utilised to construct additional solutions: Generally, each solution has to be determined individually in an elaborate procedure.

Pure linearity is a rare case in the mathematical description of physical systems. Hardly any authentic model of a real system is purely linear. One may object that the particularly important example of quantum mechanics is an exception, since quantum mechanical wave functions obey the superposition principle. However, this principle comes along with the infinite dimensionality of the systems description in terms of wave functions, which is a problem of at least the same weight (any nonlinear, finite-dimensional system can be mapped to a linear, infinite-dimensional system by appropriate transformations). A linearisation of a nonlinear process can describe the behaviour of a system correctly at most locally in phase space. In other words, nonlinear systems are generic in nature, whereas linear dependences appear to be exceptions.

An appealing reason to study nonlinear dynamics is the rich variety of surprising phenomena and the extremely complex behaviour possessing no counterpart in linear systems. Examples are strange attractors, bifurcation routes, fractal structures and solitary solutions. The enormous complexity of the underlying structures is an essential difference between linear and nonlinear systems: Linear objects are generally easy to be classified. Contrary to this, the abundance of diverse nonlinear phenomena is not easily describable in a systematic way. So far, no general method is available to predict the qualitative properties of a nonlinear system in advance. For example, it is often not possible to judge a priori whether a dynamical system will display regular or chaotic dynamics. In the nonlin-

ear case a description by dividing the system into parts which are treated independently is generally not possible. The notorious difficulties in approaching and understanding nonlinear systems is in contrast to their ubiquity in nature. An enormous variety of scientific disciplines, covering among others mathematics, physics, biology, chemistry, engineering sciences, medicine and fields such as political economy and business management use nowadays extensively tools available in the theory of nonlinear systems.

A multitude of textbooks dealing with nonlinear systems in general and chaotic dynamics in particular have been published up to now (see, for example, refs. [1–21]). Some books and journal articles are more mathematically oriented [4, 7, 9, 11, 16, 22–26], while others illustrate mainly the physical concepts [1–3, 5, 6, 8, 10, 12–15, 18–21]. In addition, a considerable number of pioneering articles have been published in the literature (see e.g. refs. [27–29] and refs. [24, 30–33]). In view of the vast literature this compilation can not be considered complete.

Classical dynamical systems are composed of a phase space (state space) and a dynamical law describing the evolution of the phase space coordinates in time as an initial value problem. The nature of the law may in general be deterministic or random, the time development may be discrete (maps, providing an iterative law) continuous (flow given by a differential equation) resulting in discrete and continuous trajectories (orbits) of the system, respectively. Phase space, too, may be discrete (e.g. state space of a dice), countably or uncountably infinite (e.g. phase space variables take integer or continuous numbers, respectively). The initial values of a deterministic autonomous system and the dynamical law specify the time evolution of the system uniquely. Likewise for time-dependent (non-autonomous) systems, time can be considered as an additional phase space coordinate.

Hamiltonian systems are, mathematically spoken, a very restricted class of dynamical systems: They are specified by a single scalar function (the Hamiltonian) [3, 18, 21, 22]. Its variables appear as canonically conjugated pairs, which implies an even dimension of phase space. Due to energy conservation, the dynamical evolution of a time independent system possessing N degrees of freedom is restricted to a $2N-1$-dimensional so-called energy shell. The phase space volume of a Hamiltonian system is preserved during time evolution, i.e. the corresponding Hamiltonian flow is incompressible (Liouville's theorem). This is

due to the basic property of Hamiltonian systems to be symplectic, i.e. the differential symplectic area is independent of time (for $N = 1$ degree of freedom preservation of phase space volume and time-independence of the differential symplectic area are equivalent). The existence of the so-called Poincaré integral invariant and the Poincaré-Cartan theorem are consequences of the symplectic structure of Hamiltonian phase space.

The notion map appears frequently in this review. It describes the dynamics of a time-discrete system $x_{i+1} = f(x_i)$ [30–32, 34, 35]. Being iterated, it yields a sequence $\{x_i\}$ (trajectory of the point x_0). Maps can be derived from a time-continuous flow either by a stroboscopic sampling (particularly useful if the system has an intrinsic periodicity with respect to time) or by a suitably defined Poincaré section (yielding the Poincaré map for autonomous systems). Due to their construction both types of maps are necessarily invertible [3, 22]. Essentially, every numerical algorithm for the time-propagation of a differential equation provides a time-discrete map, since the flow is approximated by finite size steps.

Dissipative chaotic systems typically develop a so-called strange attractor. The attractor is a set of points the dynamics relaxes to if one starts from a surrounding basin of attraction. Attractors can be as simple as a stable fixed point or a stable periodic orbit (limit cycle) and as complicated as the strange attractors possessing intrinsic sensitivity with respect to the initial conditions. The borders of the basin of attraction are generally given by the unstable manifolds of fixed points of the system and are interesting objects to study, since they mark the transition between regions showing qualitatively different dynamics.

Let us now briefly address the issue of chaoticity of a deterministic dynamical system. For a regular and deterministic system, the horizon of predictability in time scales linearly with the accuracy of the initial conditions. For chaotic systems, the long time behaviour is essentially unpredictable. Their horizon increases only with the logarithm of the accuracy, which is due to exponential divergence of neighbouring trajectories. In general, the following two conditions are considered to be essential for a system to exhibit chaos (see e.g. ref. [22]): The dynamical law f is chaotic on a compact invariant set S (e.g. the attractor of a dissipative system, see below), if f is transitive on S (i.e. there exists a point with a trajectory dense in S) and if f shows sensitive dependence on the initial conditions.

The well-known Lyapunov exponent measures the exponential divergence of trajectories that are infinitesimally close neighbours in the beginning. There are as many Lyapunov exponents as dimensions, but in case of positive exponents (exponential increase of small perturbations in a chaotic system) the largest exponent dominates the overall dynamics. They can be determined by the scaling of propagated trajectories either in phase space or in tangent space [36, 37]. Particularly Lyapunov exponents of fixed points and periodic orbits can be obtained from the eigenvalues of the stability matrix of the fixed point and the monodromy matrix of the periodic orbit, respectively.

Generically, a Hamiltonian system is neither completely regular nor completely chaotic, but shows a mixed phase space (see e.g. ref. [3, 5, 18]). This can best be understood when starting from a completely integrable (regular) system. In this case the phase space is composed of invariant tori (parametrised by action- and angle coordinates) which are the support for periodic or quasi-periodic dynamics. Chaotic dynamics appears when a perturbation leading to non-integrability is added. The tori break successively into island chains of unstable hyperbolic and elliptic fixed points, the latter forming successively smaller tori. Tori with a rational ratio of frequencies are destroyed for infinitely weak perturbation. In case the ratio is irrational, the hierarchy of their decomposition is governed by the KAM theorem. This way, a self-similar pattern of elliptic and hyperbolic fixed points is generated. The dynamically invariant sets of homoclinic intersections of the hyperbolic fixed points are the seeds for the chaotic dynamics. Depending on the initial values, one obtains regular or chaotic trajectories. Finally, assuming the perturbations to be strong enough, the chaotic trajectories may dominate the phase space. In systems with two degrees of freedom, the chaotic trajectories are captured between two irrational tori, and the resulting chaotic layer is confined to a small area in phase space. However, in systems with more than two degrees of freedom diffusion of these trajectories in the continuously connected area in between the invariant tori is possible. This so-called Arnold-diffusion of chaotic trajectories allows a chaotic overall dynamics even though tori are still present [13, 38].

1.2 Periodic orbit theory and applications

The role of unstable periodic orbits was first fully appreciated by Poincaré a century ago [28, 39, 40]. In the last two decades vast insight was gained into the theory of periodic orbits of chaotic dynamical systems. In some respect, they reflect the constituting invariant structure of the chaotic system, whereas the diffusive, ergodic time development of generic trajectories corresponds to the random features of the dynamics. Therefore, the set of periodic orbits can be called the deterministic skeleton of the chaotic system. In particular, it includes essential information about the spatial and temporal correlation of the dynamics. This is why properties of the corresponding system exceeding its random character can be obtained from this skeleton [41–44].

Periodic orbits play a major role in the theory of the quantisation of classically chaotic systems in the semiclassical regime, which is a prominent branch of research in quantum chaos. This field of science is referred to as "quantised chaos" [45], "quantum chaology" [46] or "type I quantum chaos" [47]. Objects of research are the signatures of classical chaos on the quantum level. Besides the above mentioned method of period orbit expansions to be discussed in the following, level dynamics (see e.g. refs. [48–52]) and random matrix theory (see e.g. refs. [53–55], applications include besides quantised versions of classically chaotic systems [6] energy level statistics of complicated atoms and nuclei [56], microwave cavities [57] and vibrating membranes and solids [58, 59]) are the main tools of research. The cardinal object of research in quantised chaos are bounded autonomous systems with a discrete energy spectrum. The ubiquity of systems with this property can not be over-estimated, keeping the fact in mind that, except from the field-free hydrogen atom and similar two-body systems, all atoms and molecules show chaotic dynamics on the level of their classical description. Although important features of classical chaos such as sensitive dependence on initial conditions do not appear in the corresponding quantised system, wave functions and energy spectra are strongly marked by the underlying chaotic dynamics. The results of quantised chaos are universal in two ways: Firstly, one of the most important results concern the universal behaviour of quantum systems with a classically chaotic counterpart that can e.g. be read off the fluctuation statistics of their energy levels. Secondly, results of quantum chaology are also valid for a vast range of other branches in physics like electrodynamics [57], acoustics [58, 59] and

hydrodynamics [60], not to mention atomic and molecular physics [61, 62]. When considering the quantum-mechanical energy spectrum, it becomes obvious that the approaches mentioned above apply to different scales of energy: Statistical measures as provided by random matrix theory describe short- and medium ranged correlations in the energy spectrum (such as nearest neighbour spacing distribution and spectral rigidity) related to universal properties in the regular and classically chaotic regime. In contrast to this, far-reaching correlations are related to specific non-universal properties of the corresponding system such as periodic orbits, quantitatively described by trace formulas in period orbit theory. Trace formulas were first derived for physical systems by Gutzwiller [63], with similar equations being derived earlier in a more mathematical context for dynamical systems [64, 65].

Let us briefly outline the derivation of the trace formula as described e.g. in ref. [43]. Other derivations can be found in e.g. refs. [6, 66–68]. The basic approach of the trace formula can be best understood as a tessellation of the phase space approximating the flow by its periodic skeleton. Each of the composing segments is centred on a periodic orbit with specific length, the corresponding size being determined by the stability properties of the orbit. Expectation values of observables along the flow [23, 69–74] are expressed in terms of the Frobenius-Perron operator [71, 75–77] describing the time evolution of the system. The sum over its spectral eigenvalues is related to the series expansion using the periodic orbits. In other words, the spectrum of eigenvalues is dual to the spectrum of periodic orbits, representing a fundamental duality of local and global properties. However, the resulting classical trace formula [41, 42, 78–80] has the disadvantage of being singular exactly at the eigenvalues of the Frobenius-Perron operator, which results in a small radius of convergence. This problem is removed by relating the trace formula to the spectral determinant (an infinite product formula) [81, 82], or to the dynamical zeta function (when considering expanding eigenvalues only). Both possess zeros at values for which the original trace formula is singular. Quite a number of studies deal with the mathematical properties of the dynamical zeta function [6, 17, 35, 54, 66, 83–111]. For the convergence of the trace formula the hyperbolicity assumption (all cycle stability eigenvalues are bound away from unity) is crucial: The analyticity of spectral determinants and dynamical zeta functions [112–117] for hyperbolic systems like the so-called Axiom-

A systems [24, 25] can be shown [115, 118, 119], which implies a rigorous treatment of traces and determinants. Gutzwiller derived a similar trace formula, starting from an appropriately defined level density operator for energy eigenstates [6, 120] instead of the Frobenius-Perron operator. The resulting trace formula contains properties of the periodic orbits such as their periods, their actions and Lyapunov exponents. Additionally Maslov indices are needed and obtained by inspection of turning points, focal points and caustics of the corresponding orbits [6, 67]. Basically, the trace formula can be applied "forwards" and "backwards". The "backward" application, i.e. the calculation of characteristics of periodic orbits starting from a given level density, has been successfully applied to e.g. the hydrogen atom in a magnetic field [121] and to the one-dimensional [60] and three-dimensional [122, 123] Helium atom. The much more important "forward" application of the trace formula turns out to be significantly more difficult due to: (i) the exponential proliferation of the number of periodic orbits with increasing period, (ii) generic inaccuracies in the course of the numerical finding of the periodic orbits and (iii) convergence problems of the trace formulae. Nevertheless, this theory has successfully been applied to a large number of systems, allowing the semiclassical description of many quantum mechanical properties such as level densities [62] or, as a particular example, quasi-Landau resonances in photo-absorption cross sections [124–126] (for a comprehensive overview, see e.g. refs. [6, 17, 127] and references therein). Further progress has been made e.g. in understanding the influence of the non-Coulombic core of the potential in atoms other than hydrogen [128, 129], concerning the role of so-called ghost orbits [130] (complex predecessors of orbits created near bifurcations) and discussing chaos in atoms in crossed fields ([131, 132] and references therein). Retaining only the shortest periodic orbits in the expansion in many cases turns out to be a good strategy to extract relevant information about the system [122, 123]. Cvitanović and collaborators found an appealing way to circumvent the convergence problems using sophisticated re-summation techniques: the so-called cycle expansions. They divided the contributions of the periodic orbits to the dynamical zeta function or to the spectral determinant into those originating from so-called fundamental orbits, i.e. orbits that can not be approximately composed (shadowed) by shorter ones, and corresponding curvature contributions [41, 42, 133]. The curvature expansions converge well if the completeness of the symbolic grammar of the system and its hyperbolicity

is guaranteed. Cycle expansions allow the evaluation of expectation values on basis of the shortest cycles and have been successfully applied to a variety of systems [30, 42, 133–141] including in particular systems in statistical mechanics [72, 83, 142, 143], scattering processes [144–147], deterministic diffusion [148–159], intermittent systems [160, 161], to spatio-temporal chaotic systems [162] such as the Kuramoto-Sivashinsky equation [163–166], to experimental time series [167–171] and to a large number of other dissipative systems to extract characteristic quantities of chaotic attractors (Lyapunov exponents, fractal dimensions, entropies etc.) The expansions are generally ordered with respect to the length of the orbits [41, 42, 137, 172, 173]. However, the symbolic dynamics might not be easy to obtain. Another problem can be the large number of periodic orbits necessary for the expansion, the required completeness and the slow convergence properties of the expansion [172, 173]. There are indications that an expansion with respect to the stability of the orbits shows improved convergence properties and works even for systems without a symbolic dynamics [174–176]. However, so far no rigorous theory of stability ordering has been developed.

The control of chaos [3, 177–186] is another important area of application of periodic orbit theory which has become very widespread and active in the past decade. In many situations it is desirable to control and guide a dynamical system which is originally chaotic onto a desired periodic trajectory applying only tiny perturbations. This way the system is prevented from following the undesired chaotic behaviour. Regular time dependence is relevant in many branches of engineering, medicine and science, e.g. for the design of fast-moving machines, steering gears of air planes and other devices exposed to turbulent flows as well as for the design of electronic and medical-technical devices such as cardiac pace makers. Since periodic orbits are dense in phase space, one of them can certainly be found close to any desired trajectory. The system is then controlled by following this orbit. Chaos control can be achieved either by feedback control or by non-feedback control. Non-feedback control changes the controlled orbit of the system and requires comparatively large perturbations [187–191]. The feedback control is the far more important approach (see e.g. refs. [3, 184, 192–205]). It utilises the fact that the controlled orbit is an unstable periodic orbit of the original system. The feedback applied to the system to steer it onto the desired periodic orbit vanishes when control is achieved

(in the absence of noise). Therefore the amplitude of the feedback signal is limited only by the noise level. The wide-spread OGY method, developed by Ott, Grebogi and Yorke ([3, 184, 204, 205], see in particular ref. [183] for a concise overview), uses small changes in the parameters of the system to make a particular periodic orbit stable. To this aim, targeting schemes to steer the chaotic trajectory are applied [197, 206]. Meanwhile, the OGY method and modifications of it have been applied to a multitude of mathematical and physical systems. Examples are as diverse as the stabilisation of a parametrically excited cantilever ribbon [192], of higher-order periodic orbits in a periodically driven diode resonator [207, 208] and other electronic circuits [209], of periodic orbits in chemical system [210–212] such as the control of chaos in the Belousov-Zhabotinsky reaction [212], the stabilisation of complex periodic waveforms of a chaotic multi-mode laser [213–215], the suppression of chaotic flow in a thermal convection loop [216] and in a microwave-pumped spin-wave-instability experiment [217], and stabilisation of cardiac arrhythmia [93, 218]. Meanwhile, also Hamiltonian systems with complex conjugated eigenvalues can be stabilised employing the OGY method [180–182] (for more applications, see ref. [183] and references therein). The method has been applied to systems with natural frequencies ranging from 10^{-2} Hz to 10^{5} Hz. Valuable modifications of it are reviewed e.g. in refs. [205, 208, 219–221]. The advantage of the OGY method is that it does not – except for the periodic orbit to be stabilised – require any a priori analytical knowledge of the system, thus successful applications to many physical experiments are possible. For a restricted class of systems a modified form even allows the detection of certain unstable periodic orbits with unknown position of a restricted class of systems [177–179]. However, the OGY method and related methods are discrete in time (they refer to the Poincaré map of the system), and are therefore sensitive to noise, leading to occasional bursts when the system is far from the controlled periodic orbit. This lack of robustness is also the reason why none of these techniques can be scaled up to significantly higher frequencies. In addition, the requirement of a computational analysis of the system at each crossing of the Poincare surface makes it difficult to apply the method to very fast systems.

A considerable amount of these drawbacks are absent in another class of chaos control methods, the time-delayed feedback control: Its characteristic is the continuous linear time-delayed feedback applied at each computational iteration in time. The application

of discrete changes of the parameters as in the OGY method, increasing the sensitivity to noise, is avoided.

An approach of this type attracting much attention is the one by Pyragas [222–226]. His method can be illustrated if applied to a set of ordinary nonlinear differential equations [198]:

$$\dot{y} = P(y, \mathbf{x}) + F(t), \quad \dot{\mathbf{x}} = \mathbf{Q}(y, \mathbf{x})$$

The scalar variable $y(t)$ represents the system output (such as a time series of experimental data), whereas the vector $\mathbf{x}(t)$ contains the remaining variables of the system which are either not available from observation or of no interest. The combined vector $\{y(t), \mathbf{x}(t)\}$ represents the complete state of the unperturbed system. In general, however, the above governing equations are unknown. The external continuous-time perturbation is denoted by $F(t)$. $F(t)$ is determined in such a way that it does not change the desired unstable periodic orbit of the system, but only its stability properties from unstable to stable. Various analytical forms of this perturbation have been looked at [198, 200, 201, 227]. The most promising ansatz for $F(t)$ from an experimental point of view is the use of the feedback-perturbation [198]. It can be applied to stabilise the system onto a periodic orbit $\tilde{y}(t)$ found before

$$F(t) \equiv F(y(t), \tilde{y}(t)) = K \cdot [y(t) - \tilde{y}(t)]$$

or by applying time-delay feedback in the form

$$F(t) \equiv F(y(t), y(t - \tau)) = K \cdot [y(t - \tau) - y(t)]$$

with K being an experimentally adjustable constant. Obviously, the perturbation vanishes on the unstable periodic orbit when the delay time τ matches its period T. This algorithm can be implemented straightforwardly in most experiments. The method has been successfully applied to non-autonomous as well as autonomous electronic devices with chaotic time dependence [201, 202, 222, 225] and to optical systems [215, 228].

The prominent advantages as compared to OGY control are that neither a computational analysis of the system nor the construction of a Poincaré map are necessary. Therefore application to fast systems is achievable. Furthermore, the knowledge of the position of the particular unstable periodic orbit is not necessary. A drawback of the

method is the limited range of the system parameters within which the control can be achieved [198]. This disadvantage can obviously partly cured by a variation of the method [229]: The feedback forcing is applied to the accessible parameters of the system instead of adding a feedback term to the governing equations of motion. This approach can be further generalised [203]: It can be shown that it is equivalent to the inclusion of information from infinitely many previous states of the system

$$F(t) = K\left((1-R)\sum_{m=1}^{\infty} R^{m-1}(y(t-m\tau)-y(t))\right)$$

with the additional parameter $0 \leq R < 1$ being available to the experimentalist. Stabilisation can be achieved over a wide range of parameter values with partly faster convergence only for particular values of K. Meanwhile, the sensitivity of this modified algorithm to noise [227], and its theoretical analysis [223] have been examined.

However, a general problem of the method by Pyragas and its modifications is that its theoretical basics are still not very well understood [230–232]. The parameters of the algorithm have to be adjusted very diligently. This applies to the amplitude K of the feedback-term as well as to the length of the period of the unstable periodic orbit. The values of these parameters are limited to a very narrow rage in order to achieve stabilisation. Additionally, only closed orbits with non-vanishing torsion seem to be detectable [233]. However, methods based on the delay-feedback control, adapted to individual systems, seem to be more successful (see e.g. refs. [234–236]).

2 Conventional approaches to localise periodic orbits

This section gives a brief overview of various methods occupied with the problem of locating periodic orbits in chaotic dynamical systems. In doing this, we omit the vast literature related to closed orbits in time series analysis as well as statistical methods such as recurrency search and concentrate on constructive methods, instead.

Due to the remarkable diversity and complexity of general dynamical systems, there are just a few purely mathematical papers dealing with the existence and the properties of periodic orbits on a general and global level [101].

2.1 Inverse iteration

Inverse iteration is a suitable method to locate unstable periodic orbits of one-dimensional maps, since these orbits are stable ones of the inverse map (and vice-versa). As the inverse map is multi-valued, a choice of the particular pre-image has to be taken at each backward iteration step. The sequence of the branches chosen represents the symbolic code of the particular orbit. Periodic orbits of higher dimensional systems, however, generally have both stable and unstable directions. Therefore, they stay unstable also when iterated backwards. To tackle these systems, essentially the equation $\mathbf{f}(\mathbf{r}) = 0$ has to be solved explicitly, requiring more refined techniques.

2.2 Bisection and more in one dimension

In many cases, the quest for periodic orbits in the phase space of the system can be posed as a fixed point problem of a generally highly nonlinear vector-valued function. This way, the problem is recast into the location of roots of an appropriately defined function. A series of approaches has been developed to tackle this question, in particular for one-dimensional systems. One of the most basic ones is the bisection method. It utilises the property of a continuous scalar function to have a root in an interval in which it changes sign. The function is evaluated at the midpoint of the interval and is used to replace the boundary point of the interval whichever has the same sign. The algorithm is unbeatably robust and the rate of convergence is linear (i.e. the uncertainty is scaled with a constant factor with each iteration step, sometimes also called “geometrical” or “exponential” rate

of convergence). Although the algorithm is guaranteed to converge as long as the interval contains at least one root, the determination of several different roots generally raises a problem.

Another algorithm converging faster than the bisection method, at least for well-behaved functions, is known as the secant and false position method, respectively [237]. Both methods determine the position of the root of a linear approximation of the function, given its values at two successive points. Of the three resulting points, the secant method retains the two most recent ones, whereas the false position method retains always the two best estimates with opposite sign from the function value, bracketing the root. The secant method converges faster, but also less safe than the false position method. Ridders' method [238] is a powerful, refined modification of the false position method. It evaluates the function at the midpoint of the interval bracketing the root and approximates it by an exponential function. The advantages are besides a fast rate of convergence of order $\sqrt{2}$ and a general robustness, that the trajectory is guaranteed to stay in the bracketing interval.

The Van Wijngaarden-Dekker-Brent method [239] combines the robustness of bracketing algorithms with the fast convergence of higher-order methods. It uses a quadratic interpolation to approximate the function, evaluated at three prior points. It accepts the estimate of the root only in case it is still contained in the interval. Otherwise, a bisection step is performed. This method is guaranteed to converge and is the recommended method of choice to determine roots of one-dimensional functions without having access to its derivative.

2.3 Bisection in multiple dimensions

Modifications of the aforementioned methods for higher-dimensional systems are rare. One exception is the continuation of the bisection method for locating zeros of a one-dimensional function to higher-dimensional systems, which was developed by M.N. Vrahatis [240–248]. The area in the N-dimensional phase space containing the fixed point to be located is surrounded by an irregular $2N$ polyhedron in such a way that each edge is intersected by exactly one $N-1$ dimensional manifold determined by the condition of the vanishing of one of the N coordinates. This polyhedron is then bisected in a controlled

way such that its above-mentioned defining feature is maintained. By performing this procedure iteratively, a fast convergence of the algorithm in the fixed point is achieved. What is more, the detection is independent of any stability properties of the fixed point and is guaranteed to succeed, as long as the initial polyhedron contains a fixed point. However, in case many fixed points cluster in small regions of phase space, the $2N$ vertices of the polyhedron have to be placed in the neighbourhood of a particular fixed point in order to locate it. Therefore, the method is less useful for the detection of complete sets of periodic orbits of a system, but proves to be valuable for "polishing up" a fixed point once its location in phase space is approximately known. The algorithm has successfully been applied to a number of nonlinear dynamical systems including the standard map [248], the driven Duffing oscillator [240], the Hénon map [241], molecular systems [242, 245, 247] and mathematically motivated functions [243]. Its convergence is fast and independent of the stability properties of the fixed point as well as the initial conditions. However, the possibilities to locate a complete set of closed orbits of the same length are limited.

A general remark on finding roots in higher dimensions is appropriate here: Generally, the various components of a vector-valued function, which have to vanish simultaneously in case of a root, are uncorrelated. The fluctuations of the signs of their individual components in phase space generally have no relation to zeros of the complete function, different to the one-dimensional case. This is why the detection of roots of higher-dimensional functions is much more elaborate compared to one-dimensional ones.

2.4 Newton algorithm

The algorithm named after Isaac Newton has become one of the most prevalent methods to calculate roots of a wide class of functions rapidly and in an approximate way [237, 249–251]. In 1669 Newton developed an algorithm to solve polynomial equations by solving what can in modern terms be called the linearisation of the equation for small increments of the independent variable [252]. However, this approach does not use the notion of derivative explicitly and refers to the special class of polynomial equations only. Furthermore, Newton did not consider the resulting equation as an iterative process, approximating the root step by step. The method was further developed by Raphson

[253], who avoided the substitutions present in Newton's approach. Later studies were done by Simpson, Mouraille (who first mentioned the importance and the difficulty of the choice of the initial point), Cauchy and Kantorovich [254].

The Newton method is a first order method, originating from a Taylor expansion up to linear order. It approximates the zero $f(r) = 0$ of the function $f(r)$ as the limit of the recurrence

$$r_{n+1} = r_n - \frac{f(r_n)}{f'(r_n)}$$

starting with an initial point r_0. The local convergence property is guaranteed: Newton's method will always converge if the initial point is sufficiently close to the root and if the root is not singular. The difficulty of the choice of the initial point is essentially the main drawback of the method [251]. A whole branch of mathematics emerged, giving theorems to optimise initial conditions that provide safe convergence of general numerical root-finding algorithms. The so-called point estimation theory, for example, which was first introduced for Newton's method [255], deals with domains of convergence and convergence conditions by using only information about the function at the initial point [256–259].

A constructive theorem of Kantorovich [254] yields estimates about the radius of convergence of Newton's method, if bounds for the derivatives of the functions are given. The convergence of the algorithm is quadratic, i.e. the number of reliable digits is doubled at each iteration. However, far from a root, the higher-order terms in the Taylor expansion become important and the algorithm generally produces meaningless results. This might in particular be the case if the search interval between the starting value and the root includes a horizontal asymptote or a local extremum of the function.

As mentioned above, the Newton algorithm is a first order method. Inclusion of second order terms of the Taylor expansion can generally increase the speed of convergence. A first attempt in this direction was done by E. Halley in 1694, resulting in the so-called Halley's method:

$$r_{n+1} = r_n - \frac{2f(r_n)f'(r_n)}{2f'(r_n) - f(r_n)f''(r_n)}$$

The Householder iteration [260] is a generalised approach of higher order:

$$r_{n+1} = r_n + (p+1)\left(\frac{(1/f)^{(p)}}{(1/f)^{(p+1)}}\right)_{r_n}$$

with p being an integer. For this method, the rate of convergence is of order $(p+2)$. The choice $p = 0$ restores Newton method with quadratic convergence, whereas $p = 1$

yields Halley's method with cubical convergence. For each of these methods, a favourable starting point is required. Another possible modification of the original method is to expand f in terms of powers of the step-size $h_n = -\frac{f(r_n)}{f'(r_n)}$ of the simple Newton algorithm [237] and to optimise the coefficients in order to minimise

$$f(r_{n+1}) = f(r_n + h_n + a_2^n \frac{h_n^2}{2!} + a_3^n \frac{h_n^3}{3!} + ...)$$

The multi-dimensional generalisation of the original Newton's method for solving the nonlinear equation

$$\mathbf{F}(\mathbf{r}) = 0 \tag{1}$$

with a higher-dimensional phase space is the following iteration

$$\mathbf{r}_{n+1} = \mathbf{r}_n - \mathbf{J}^{-1}(\mathbf{r}_n) \cdot \mathbf{F}(\mathbf{r}_n) \tag{2}$$

with the stability matrix

$$\mathbf{J}_{ij}(\mathbf{r}) = \frac{\partial F_i}{\partial r_j}(\mathbf{r}) \tag{3}$$

In particular for higher dimensions, the global convergence behaviour of the Newton algorithm is typically unpredictable. Generically, the basin of convergence is not even a continuously connected area. It is highly irregular, which is essentially due to the "bouncing-away to infinity" of the trajectory after a certain number of iteration steps. Especially when applying Newton's method to a polynomial of degree two or higher one obtains a rational map of the complex plane, resulting in a highly fractal Julia set in case of the existence of more than two roots [237, 261–263]. Nevertheless, the Newton method is unbeatably efficient for polishing up inaccurately determined zeros within a few steps.

The determination of the inverse stability matrix Eqn. (3) required to perform the Newton method Eqn. (2) can be avoided by numerically approximating this quantity [264]: The method of regula falsi includes the Euler-discretisation of the derivative matrix (assuming a linear approximation of the function) into the Newton algorithm. However, the convergence pattern is similar to that of the original Newton method, and additional numerical instabilities may arise. These drawbacks also appear when using a quadratic approximation of the function.

Another modification of the original algorithm are multidimensional secant methods such as Broyden's Method [265]. They reduce to the secant method in one dimension

[266]. Beside these, there are quite a few modifications of the original method, e.g. giving an individual adaption to particular functions, where the Newton algorithm alone would converge slowly or difficulties due to turning points are met [267]. Other variations concern the application to localisation of periodic orbits in chaotic systems [43, 268–274], including dissipative as well as Hamiltonian flows. This is mostly achieved by applying the algorithm to a suitably introduced Poincaré map (see below, section 6 and ref. [43] for details).

For applications to various Hamiltonian systems, the so-called monodromy method gained considerable attention [275–280]. In this approach, the particular banded form of the monodromy matrix of analytically given maps is taken advantage of. Iteration steps correspond to steps of the original Newton algorithm, but can be evaluated faster. This method is particularly suited to trace periodic orbits while varying a system parameter.

Another modification of the original method has been developed in order to locate periodic orbits of maps more easily [43]: As a periodic orbit of length p of a map is essentially a fixed point of the p times iterated map $f^{(p)}(r)$, it suffices to solve the equation $f^{(p)}(r) - r$ in order to detect the orbit. However, the function $f^{(p)}(r)$ generally is highly nonlinear and fluctuates excessively (see e.g. ref. [281]), which complicates the search for the roots. The periodic orbit is more easily found as the zero of the following vector function $\mathbf{F}$:

$$\mathbf{F}(\mathbf{r}) = \begin{pmatrix} r_1 \\ r_2 \\ \cdots \\ r_p \end{pmatrix} = \begin{pmatrix} r_1 - f(r_p) \\ r_2 - f(r_1) \\ \cdots \\ r_p - f(r_{p-1}) \end{pmatrix}$$

An iteration step of Newton's algorithm now takes the form:

$$\frac{d}{dr}\mathbf{F}(\mathbf{r})(\mathbf{r}' - \mathbf{r}) = -\mathbf{F}(\mathbf{r})$$

with $\frac{d}{dr}\mathbf{F}(\mathbf{r})$ being the $p \times p$ matrix (only non-vanishing entries are displayed)

$$\frac{d}{dr}\mathbf{F}(\mathbf{r}) = \begin{pmatrix} 1 & & & & & -f'(r_p) \\ -f'(r_1) & 1 & & & & \\ & -f'(r_2) & 1 & & & \\ & & & \ldots & & \\ & & & & 1 & \\ & & & & -f'(r_{p-1}) & 1 \end{pmatrix}$$

This matrix can generally be easily inverted. For details of this procedure, we refer to ref. [43].

As already mentioned, Newton's algorithm when applied to solve nonlinear equations generally has the property to have a relatively small radius of convergence. However, a more global convergence pattern can be obtained with the following variation of the method [237]. For the original Newton's method solving the nonlinear equation Eqn. (1) the iteration Eqn. (2) is performed. Thus, with approaching a root $\mathbf{F}(\mathbf{r}) = 0$, the scalar function $f = \mathbf{F} \cdot \mathbf{F}$ is minimised. The Newton step $\mathbf{r}_{new} = \mathbf{r}_{old} + \delta\mathbf{r}$ with $\delta\mathbf{r} = -\mathbf{J}(\mathbf{r})\mathbf{F}(\mathbf{r})$ is a descent direction for f:

$$\nabla f \cdot \delta\mathbf{r} = 2(\mathbf{F} \cdot \mathbf{J}) \cdot (-\mathbf{J}^{-1} \cdot \mathbf{F}) = -2\mathbf{F} \cdot \mathbf{F} < 0$$

This suggests the following strategy: At each iteration, it is checked whether a full Newton step reduces f. If this is the case, the convergence behaviour is regular and the step is performed. This way, a quadratic rate of convergence near the root is guaranteed. However, if f is not reduced, one back-traces along the Newton direction until an acceptable step (resulting in a decrease of the value of f) is reached. As the Newton step is a descent direction of f, it is guaranteed to find such a step [272].

2.5 Variational algorithms

Generally, relaxation methods work by iteratively minimising a suitably defined cost function [264]. It measures the deviation of the approximate p-periodic orbit $\tilde{\mathbf{r}} = (\tilde{r}_1, \tilde{r}_2, ..., \tilde{r}_p)$ of the n-dimensional map $x_{i+1} = f(x_i)$ from the exact one, e.g. of the form

$$E(\tilde{\mathbf{r}}) = \sum_{i=1}^{n} \left(\tilde{r}_i - f^{(p)}(\tilde{r}_i)\right)^2$$

Often in variational or relaxating algorithms, the step size of the propagated trajectory is linearly dependent on the value of the cost function. Non-variational methods like the Newton algorithm have an additional dependence also on other quantities of the system, such as its stability matrix. This is also the reason for a different numerical convergence behaviour: The Newton method converges super-exponentially and therefore faster than variational algorithms. However, the latter ones are much more stable due to their smaller step size, which is why they can be used to detect even long periodic with a relatively small extension of the linear neighbourhood. Another consequence is the large extension of the basins of attraction of the individual orbits. This property makes these procedures very attractive for numerical applications, since the speed of convergence of relaxation algorithms in the extensive areas of attraction is high due to the long distance of the trajectory to its final solution. The trajectory, once started even far away from the fixed point (the periodic orbit) quickly reaches its linear neighbourhood. Apart from the method of stability transformation discussed in this study, several other algorithms can be traced back to a variational ansatz.

A successful variational method to locate periodic orbits of a particular class of systems has been developed by O. Biham and W. Wenzel [282] and has been widely applied since [173, 283–296]. It can be applied to time-discrete systems (maps) that can be written as a one-dimensional recurrence equation $r_{i+1} = f(r_i, r_{i-1}, ..., r_{i-k})$, generally involving $(k+1) > 2$ time steps. The Hénon map

$$x_{i+1} = 1 - ax_i^2 + by_i \quad , \qquad y_{i+1} = x_i$$

is an example of a system with this property. The corresponding one-dimensional recurrence equation $f(r)$ has the following form

$$r_{i+1} = 1 - ar_i^2 + br_{i-1}$$

In order to calculate a closed orbit of length p, a p-dimensional vector field $\mathbf{v} = (v_1, v_2, ..., v_p)$ vanishing on the periodic orbit is introduced by

$$\frac{dr_i}{d\tau} = v_i = r_{i+1} - 1 + ar_i^2 - br_{i-1} \ , \qquad i = 1, ..., p$$

For fixed r_{i+1}, r_{i-1}, the equation $v_i = 0$ has two solutions for r_i, representing two extremal points of a local potential function

$$v_i = \frac{\partial}{\partial r_i} V_i(r) \ , \qquad V_i(r) = r_i(r_{i+1} - br_{i-1} - 1) + \frac{a}{3} r_i^3$$

The vector field $\mathbf{v}$ is now propagated in time τ - with an essential modification of the signs of its components:

$$\frac{dr_i}{d\tau} = \sigma_i v_i \ , \qquad \sigma_i = \pm 1 \ , \qquad i = 1, ..., p$$

The iteration starts with estimates for the periodic orbit $\{r_i,\, i = 1, ..., p\}$ as initial points. Within each step of the algorithm, all p points of the trajectory are varied, the size of the corresponding individual variations given by $\sigma_i v_i$. With the choice $\sigma_i = +1$ the flow is in direction of the local maximum of $V_i(r)$, for $\sigma_i = -1$ in direction of the local minimum. The initial directions of the p individual trajectories have to be put in by hand. The potential functions V_i are not bounded, therefore an initial guess too far from the exact orbit will lead to divergence. However, the basins of attraction of the periodic orbits are very large. For the Hénon map, their extension is of order 1 and thus exceeds by far the radius of convergence of Newton's method. What is more, it turns out that the directions σ_i, read as a binary code, are definitely related to the symbolic code of the periodic orbit that is approached. Therefore the detection of a periodic orbit, its symbolic code given, is possible with this algorithm. A modified version of the method even allows the detection of complex zeros of real functions [283]: All 2^p complex periodic orbits of length p of the real Hénon map can be localised [283]. The algorithm of O. Biham and W. Wenzel is in detail investigated in ref. [172]. However, some problems in the convergence process of the algorithm have been reported [172, 291, 297]: The evolution of the vector field $\mathbf{v}$ might not converge in a periodic orbit, but in a limit cycle [172]. However, this problem is remedied in the complex version of the algorithm [283]. Furthermore, it might happen that different symbolic sequences $\{\sigma_1, \sigma_2, ..., \sigma_p\}$ converge in the same periodic orbit (i.e. the initial guess has to be improved), or that certain periodic orbits are not detectable for certain parameter values of the Hénon map [291, 297].

Further methods for detection of periodic orbits based on the symbolic code have been invented [298, 299]. In these methods, deviations of the symbolic sequence (describing history and past of the trajectory) of the approximate periodic orbit with respect to the exact one act as guidelines for small corrections of the orbit along its stable and unstable directions. With this approach, detection of periodic cycles in a range of systems such as the Hénon map, the diamagnetic Kepler problem, the collinear Helium atom, different types of billiards and dissipative systems has been achieved.

As a result, methods based on a variational ansatz seem to be applicable to a larger class of systems and are straightforward to be implemented. This compensates the drawback of a slower speed of convergence. They generally make use of an artificial dynamics with help of a cost function, suitably defined on the phase space. The numerically elaborate calculations of e.g. stability matrices in tangent space is not necessary. In addition, these procedures are generally very robust. The most important advantage, however, is the large extension of the basins of attraction and the exquisite global convergence properties of the variational and relaxation algorithms.

3 The stability transformation method

3.1 Basic Theory

The method of stabilisation transformation (ST method) has been invented by P. Schmelcher and F.K. Diakonos [300, 301]. It is an iterative approach for the detection of unstable periodic orbits (POs) in chaotic dynamical systems. In this section we introduce the ST method in its original form. The dynamical system is given by the following time-discrete map

$$\mathbf{f}: \quad \mathbf{r}_{j+1} = \mathbf{f}(\mathbf{r}_j)$$

defined in n dimensions. We are interested in the unstable POs of length p of the chaotic system $\mathbf{f}$. These orbits are just the fixed points (FPs) of the p times iterated map $\mathbf{f}^{(p)}$:

$$\mathbf{f}^{(p)}: \quad \mathbf{r}_{j+1} = \mathbf{f}^{(p)}(\mathbf{r}_j)$$

How to detect the FPs of the map $\mathbf{f}^{(p)}$? In completely chaotic systems all FPs are unstable, which means that the stability matrices of the FPs have at least one eigenvalue with modulus larger than one. Its instability is the reason for the difficulty to localise the FP: The dynamics of the map is directed in such a way that a point in the neighbourhood of the unstable FP is at once repelled and mapped further away. The idea underlying the ST method is the following: *We seek a dynamical system* $\mathbf{s}$ *with fixed points at exactly the same positions as in the system* $\mathbf{f}^{(p)}$*. However, the stability of the FPs of* $\mathbf{s}$ *is altered in an advantageous way compared to* $\mathbf{f}^{(p)}$*: The transformed FPs of* $\mathbf{s}$ *are dissipatively stable.* At this point it becomes obvious how the transformed dynamical system $\mathbf{s}$ helps us to locate the POs of the original system since it is straightforward to find a dissipatively stable FP in the phase space: A trajectory sufficiently close to the FP is attracted and converges to the FP. A feasible approach to find the FPs of the system $\mathbf{s}$ is to propagate a *set* of given initial points by applying $\mathbf{s}$ and to collect all points in phase space obeying a certain convergence criterion. The latter points are stable FPs of $\mathbf{s}$ and by construction unstable FPs of the p–times iterated original system $\mathbf{f}^{(p)}$. Having provided the basic ideas let us now turn to their implementation. An ansatz for the construction of the stabilised system $\mathbf{s}$ reads as follows [300, 301]:

$$\mathbf{s}: \quad \mathbf{r}_{j+1} = \mathbf{s}(\mathbf{r}_j) = \mathbf{r}_j + \lambda \mathbf{C}[\mathbf{f}^{(p)}(\mathbf{r}_j) - \mathbf{r}_j] \tag{4}$$

The matrix $\mathbf{C}$ is constant, regular and real, with its entries still to be determined with the requirement that an unstable FP of $\mathbf{f}^{(p)}$ becomes stable in $\mathbf{s}$. The scalar quantity $0 < \lambda \ll 1$ is a parameter for the dynamical system $\mathbf{s}$. Its meaning will become transparent in the following. It is obvious that this ansatz meets the above-stated requirement of a one-to-one relation between the positions of the FPs of the system $\mathbf{f}^{(p)}$ and the system $\mathbf{s}$. However, we pay for the simple form of the ansatz (4) with the disadvantage that not all FPs can be stabilised applying a single transformation. For a fixed $\mathbf{C}$ and λ only a certain part of the FPs of the system $\mathbf{s}$ are stable, whereas the others retain their repelling character. Fortunately, this can be remedied by constructing not only one system $\mathbf{s}$, but a whole set $\mathbf{s}_1, \mathbf{s}_2, \mathbf{s}_3, ...$ of transformed systems:

$$\mathbf{s}_i : \quad \mathbf{r}_{j+1} = \mathbf{s}_i(\mathbf{r}_j) = \mathbf{r}_j + \lambda \mathbf{C}_i[\mathbf{f}^{(p)}(\mathbf{r}_j) - \mathbf{r}_j] \tag{5}$$

For each dynamical system $\mathbf{s}_i$ the corresponding matrix $\mathbf{C}_i$ takes on a different appearance. Consequently, for each of the systems $\mathbf{s}_i$ different sets of FPs are stabilised and can be detected. It is the aim to locate all FPs of the p-times iterated map $\mathbf{f}^{(p)}$ by a sophisticated construction of the set $\{\mathbf{s}_i\}$, i.e. by a suitable choice of the set of matrices $\{\mathbf{C}_i\}$. Schmelcher and Diakonos indicated [300, 301] that the following matrices allow a stabilisation of all FPs in the above described manner: The $n \times n$–matrices $\mathbf{C}_i$ have only one non-vanishing entry $+1$ or -1 in each row and column. There are exactly $2^n n!$ such matrices, i.e. we have to deal with the same number of stability transformed systems. The geometrical operations corresponding to these transformations form a group of spatial reflections and permutations. Our ansatz Eqn. (5) works *independently of the length p of the periodic orbits to be detected.* The length p affects only the iterate $\mathbf{f}^{(p)}$ of the map, but does not alter the number of necessary transformations or the form of the matrices $\mathbf{C}_i$. For a given system $\mathbf{f}$ one can therefore detect POs of in principle arbitrary length with the same set of matrices $\mathbf{C}_i$. In section 3.2 we will discuss the $\mathbf{C}_i$–matrices for two-dimensional systems in more detail.

The meaning of the parameter λ can be elucidated by deriving a corresponding equation for the stability matrices. Let $\mathbf{T}_f$ and $\mathbf{T}_{s_i}$ be the stability matrices of $\mathbf{f}$ and $\mathbf{s}_i$, respectively. From Eqn. (5) we obtain

$$\mathbf{T}_{s_i} = \mathbf{1} + \lambda \mathbf{C}_i(\mathbf{T}_f - \mathbf{1}). \tag{6}$$

Multiplication of $\mathbf{T}_f - \mathbf{1}$ by the matrix $\mathbf{C}_i$ has the following effect. A priori, the eigenvalues of $(\mathbf{T}_f - \mathbf{1})$ in Eqn. (6) can acquire any value. The product matrix $\mathbf{C}_i(\mathbf{T}_f - \mathbf{1})$ is supposed to have only eigenvalues possessing negative real part, given a properly chosen matrix $\mathbf{C}_i$. Scaling with a small positive parameter λ allows to make the eigenvalues of the matrix $\mathbf{C}_i(\mathbf{T}_f - \mathbf{1})$ in principle arbitrarily small. As a result, the eigenvalues of the matrix $\mathbf{1} + \lambda\mathbf{C}_i(\mathbf{T}_f - \mathbf{1})$ can be scaled to have only eigenvalues with absolute value less than one: This is exactly the property that defines a FP of a map to be stable. The close relation of the parameter λ to the magnitude of the eigenvalues of $\mathbf{T}_f$ is obvious: The larger the absolute value of the eigenvalues are, i.e. the more unstable the corresponding FP is, the smaller the value of λ has to be in order to achieve stabilisation. The instability of FPs of a PO increases with its length p, therefore the value of the parameter λ has to be reduced to localise increasingly longer POs.

At this point, it is necessary to point out that the notion "stabilisation of periodic orbits" is used in a different way in the context of the OGY control compared to the ST method. OGY control works by performing tiny changes of the parameters of the system. Contrary to this, the ST method is based on the construction of a new dynamical system with the POs having new stability properties. When working with the two methods, the stabilisation of orbits is therefore achieved in qualitatively different ways.

To detect FPs of a n–dimensional system $\mathbf{f}^{(p)}$, we proceed as follows: We generate the $2^n n!$ different stability transformed systems $\mathbf{s}_i$, using the different matrices $\mathbf{C}_i$. With each of these systems and a sufficiently small value of the parameter λ a set of suitably placed initial points (grid) is propagated. A certain number of trajectories, starting from the initial points, converge for each $\mathbf{s}_i$. These points of convergence are the FPs of the map $\mathbf{f}^{(p)}$. Of course it is possible to detect a particular FP more than once. The complete PO can be obtained by propagation of the individual FPs with the map $\mathbf{f}$.

An important issue for the numerical implementation of the algorithm is the question concerning the *existence of a minimal set* of the ST method. As discussed above, $2^n n!$ different stability transformed systems can be generated from a n-dimensional dynamical system $\mathbf{f}$. In two dimensions, as shall be shown in section 4, each FP is stable in two different transformed systems $\mathbf{s}_i$ and $\mathbf{s}_j$. One might conjecture that only half of the number of transformations is necessary. In fact it has been shown that in two-dimensional systems

only three stability transformations of the original set of eight are necessary to detect all FPs [300, 301], assuming that only saddle points, but no sources (repellors) are present. In case of the existence of sources, the minimal set has to be enlarged by an additional transformation. The three matrices of the minimal set for generic chaotic systems (no sources) read

$$\begin{pmatrix} 1 & 0 \\ 0 & 1 \end{pmatrix}, \quad \begin{pmatrix} -1 & 0 \\ 0 & 1 \end{pmatrix}, \quad \begin{pmatrix} 1 & 0 \\ 0 & -1 \end{pmatrix}$$

In ref. [300, 301] the minimal set has been determined analytically. In the framework of section 4, that contains a geometrical interpretation of the ST method, we shall derive a second minimal set. It is highly probable (and has been indicated by numerical investigations done so far, see sections 3.3,6.3.3) that also in the general case of higher dimensions the propagation of a set smaller than the above described one suffices for the localisation of all FPs of the system.

The excellent convergence properties of the stability transformed systems came into sight quite early and are already well documented [300, 301]. One of the most important advantages of the algorithm is the *large extension of the basins of attraction of the individual periodic orbits.* They reach far beyond the linear neighbourhood of the FPs and are simply connected areas. The second relevant advantage is the *fast convergence of the trajectories for larger distances from the periodic orbits.* These properties allow the detection of POs of a given length p with a number of initial points not significantly larger than the expected number of periodic points.

3.2 The matrices $\mathbf{C_i}$ for two-dimensional systems

Several of the dynamical systems discussed in this article are two-dimensional. Furthermore, the geometrical interpretation of the ST method as discussed in section 4 also refers to two dimensions. This is why we now provide a small survey of the 2×2 matrices used to stabilise two-dimensional systems.

There are eight matrices of the form originally required for the matrices $\mathbf{C}_i$. To label the individual indices, we replace the single running index i by a double one (k, σ). This might look unnecessary at first glance. However, when discussing the geometrical interpretation of the algorithm in section 4, this notation will have major advantages.

The symbol $\sigma = \pm$ indicates the sign of the determinant of the matrix $\mathbf{C}_{k\sigma}$. The index $k = 0...3$ labels all matrices $\mathbf{C}_{k\sigma}$ with determinants of the same sign. The eight matrices are given by

$$\mathbf{C}_{0+} = \begin{pmatrix} + & \cdot \\ \cdot & + \end{pmatrix}, \quad \mathbf{C}_{0-} = \begin{pmatrix} - & \cdot \\ \cdot & + \end{pmatrix}, \quad \mathbf{C}_{1+} = \begin{pmatrix} \cdot & + \\ - & \cdot \end{pmatrix}, \quad \mathbf{C}_{1-} = \begin{pmatrix} \cdot & - \\ - & \cdot \end{pmatrix},$$

$$\mathbf{C}_{2+} = \begin{pmatrix} - & \cdot \\ \cdot & - \end{pmatrix}, \quad \mathbf{C}_{2-} = \begin{pmatrix} + & \cdot \\ \cdot & - \end{pmatrix}, \quad \mathbf{C}_{3+} = \begin{pmatrix} \cdot & - \\ + & \cdot \end{pmatrix}, \quad \mathbf{C}_{3-} = \begin{pmatrix} \cdot & + \\ + & \cdot \end{pmatrix}$$

The entries are denoted by $''\cdot'' \equiv 0$, $''+'' \equiv +1$, and $''-'' \equiv -1$. The matrices $\{\mathbf{C}_{k\sigma} | k = 0...3; \sigma = \pm\}$ form a group with $\{\mathbf{C}_{k+} | k = 0, ..., 3\}$ being a subgroup of order 4. The multiplication table of this group is given in Table 1. The product of two matrices is

$$\mathbf{C}_{k''\sigma''} = \mathbf{C}_{k\sigma} \cdot \mathbf{C}_{k'\sigma'} \quad \text{with} \quad k'' = (k' + \sigma' k) \bmod 4, \quad \sigma'' = \sigma\sigma' \tag{7}$$

3.3 Numerical determination of the minimal set

The minimal set of the ST method necessary to detect all POs of a dynamical system can be determined analytically in two dimensions [300, 301]. Using geometrical considerations, a second minimal set of transformations shall be constructed in section 4 [302]. However, for higher dimensional systems an analytical investigation is not feasible, since the zeros of polynomials of degree higher than two have to be determined in closed form. The geometrical interpretation to be provided in section 4 is in principle more suitable to deal with these cases, since it does not rely on analytical derivations. However, in the form we will derive it for two-dimensional systems, it is not applicable in a straightforward way to systems of higher dimensions. Therefore numerical simulations are performed to provide evidence (but not rigorous proofs) for minimal sets of 3×3–matrices $\mathbf{C}_i$. When employed in the stabilisation transformations, these matrices are supposed to allow the stabilisation of all possible kinds of FPs in a three-dimensional dynamical system. The simulation is performed by firstly generating an ensemble of 10^7 nonsingular 3×3 matrices $\mathbf{S}_i$ with entries uniformly distributed in the interval $[-1, 1]$. Then we determine the set of matrices $\{\mathbf{C}_k\}'$ out of the complete set $\{\mathbf{C}_i\}$ for which the product matrix $\mathbf{C}_k\mathbf{S}_i$ for a

certain $\mathbf{S}_i$ possesses exclusively eigenvalues with negative real parts. Matrices from this set $\{\mathbf{C}_k\}'$ stabilise the original FP with stability matrix $\mathbf{S}_i$. Following this procedure for the complete set of stability matrices $\{\mathbf{S}_k\}$ we subsequently determine the smallest subset $\mathcal{S}$ such that every matrix $\mathbf{S}_i$ is stabilised by at least one matrix $\mathbf{C}_i \in \mathcal{S}$. Eqn. (8) shows the minimal set $\mathcal{S}$ of $\mathbf{C}_i$–matrices resulting from the simulation for three dimensions. Again, the entries are denoted by $''\cdot'' \equiv 0$, $''+'' \equiv +1$, and $''-'' \equiv -1$. The negative of each of the matrices $\mathbf{C}_i$, $i = 1, ..., 9$, i.e. $-\mathbf{C}_i$, is also included in the minimal set.

$$
\begin{pmatrix} + & \cdot & \cdot \\ \cdot & + & \cdot \\ \cdot & \cdot & + \end{pmatrix},
$$

$$
\begin{pmatrix} \cdot & + & \cdot \\ \cdot & \cdot & + \\ + & \cdot & \cdot \end{pmatrix},\ \begin{pmatrix} \cdot & - & \cdot \\ \cdot & \cdot & + \\ + & \cdot & \cdot \end{pmatrix},\ \begin{pmatrix} \cdot & + & \cdot \\ \cdot & \cdot & - \\ + & \cdot & \cdot \end{pmatrix},\ \begin{pmatrix} \cdot & + & \cdot \\ \cdot & \cdot & + \\ - & \cdot & \cdot \end{pmatrix}, \tag{8}
$$

$$
\begin{pmatrix} \cdot & \cdot & + \\ + & \cdot & \cdot \\ \cdot & + & \cdot \end{pmatrix},\ \begin{pmatrix} \cdot & \cdot & - \\ + & \cdot & \cdot \\ \cdot & + & \cdot \end{pmatrix},\ \begin{pmatrix} \cdot & \cdot & + \\ - & \cdot & \cdot \\ \cdot & + & \cdot \end{pmatrix},\ \begin{pmatrix} \cdot & \cdot & + \\ + & \cdot & \cdot \\ \cdot & - & \cdot \end{pmatrix}
$$

It is an interesting feature that the matrices in the minimal set, except for the signs of the entries, describe complete permutations of period 3: The action of the matrix on a vector implies its components to be either mapped onto themselves or to be permuted cyclically. The cyclic permutations are both forward ($x \to y \to z \to x$) and backward ($z \to y \to x \to z$). For each direction of the permutation all possible combinations of switches of the signs of the coordinates are included. It is an interesting question whether this observation holds also for dimensions $n > 3$. If this would be the case it would simplify the investigation of higher dimensional dynamical systems considerably.

3.4 Time-continuous version of the stability transformation

There is a second and equally interesting way to interpret the ST method. It is based on the interpretation of the ST approach as a mapping of a vector field associated with

the original dynamical system onto a transformed vector field with new desired stability properties. This interpretation allows a transparent separation of the influence of the two key ingredients of the ST method, the $\mathbf{C}_i$–matrix and the parameter λ, on the stability properties of a FP of the map. Additionally, it is best suited for the geometrical interpretation of the ST method (see section 4).

Let us discuss the underlying approach in more detail. For a given map $\mathbf{f}$, the quantity $(\mathbf{f}^{(p)}(\mathbf{r}) - \mathbf{r})$ defines a continuous flow $\dot{\mathbf{r}} = \mathbf{f}^{(p)}(\mathbf{r}) - \mathbf{r}$ in the phase space of $\mathbf{f}$. It vanishes for the FPs of $\mathbf{f}^{(p)}$. The FPs of $\mathbf{f}^{(p)}$ therefore correspond to stationary points of the flow $(\mathbf{f}^{(p)}(\mathbf{r}) - \mathbf{r})$. These stationary points are generally unstable: In their neighbourhood, the flow is deflected away. Fig. 1 shows an example of the phase portrait of a two-dimensional system around a stationary point (these considerations equally hold in higher dimensions). Fig. 1 (a) shows the phase portrait around the unstable stationary point. A stabilisation of this point can now be achieved by a transformation of the vector field. According to Fig. 1 (b), a reversal of the sign of the x–component of the vector field is sufficient to stabilise the flow: Following the flow vectors leads to the stationary point. Changing the sign of the x–component of the vector field corresponds to the multiplication of the vector field $\mathbf{f}^{(p)}(\mathbf{r}) - \mathbf{r}$ with the $\mathbf{C}_i$–matrix $\left(\begin{smallmatrix} -1 & 0 \\ 0 & 1 \end{smallmatrix}\right)$. The resulting vector field is therefore given by the dynamical system

$$\dot{\mathbf{r}} = \begin{pmatrix} -1 & 0 \\ 0 & 1 \end{pmatrix} \left(\mathbf{f}^{(p)}(\mathbf{r}) - \mathbf{r}\right)$$

This is the time-continuous form of the transformed system. In Fig. 2 a second example of a stationary point with different stability properties is shown. Obviously, application of the same transformation as in the example of Fig. 1 does not yield a stabilisation of the stationary point. For this stationary point, a different transformation has to be applied to achieve stabilisation.

Let us now step back from the above time–continuous form to the time–discrete one in Eqn. (4) by applying an Euler–discretisation (a linear approximation) of the time derivative $\dot{\mathbf{r}}$, $\dot{\mathbf{r}} \to (\mathbf{r}_{i+1} - \mathbf{r}_i)/(\Delta t)$. From this point of view the parameter λ in Eqn. (4) corresponds to the time interval Δt introduced in this discretisation. The relation of the time interval $\lambda = \Delta t$ to the instability of the FPs detected with this particular value arises naturally. Let $\dot{\mathbf{r}} = \mathbf{h}(\mathbf{r})$ be an arbitrary time-continuous system, given by a system of ordinary differential equations (in the above discussion $\mathbf{h}(\mathbf{r}) = \mathbf{f}^{(p)}(\mathbf{r}) - \mathbf{r}$). Let

$\mathbf{r}_0$ be a stationary point of the system $\mathbf{h}$ with $\dot{\mathbf{r}} = \mathbf{h}(\mathbf{r}_0) = 0$. We now apply the stability transformation, i.e. we consider the systems $\dot{\mathbf{r}} = \mathbf{g}(\mathbf{r}_0) = \mathbf{C}_i\mathbf{h}(\mathbf{r})$, with the matrix $\mathbf{C}_i$ chosen in such a way that the stationary point $\mathbf{r}_0$ becomes stable. Let $\mathbf{S}_h(\mathbf{r}_0) = (\partial_j h_i)(\mathbf{r}_0)$ be the stability matrix of $\mathbf{h}$ in $\mathbf{r}_0$ with eigenvalues μ_k. Let $\mathbf{S}_g(\mathbf{r}_0) = (\partial_j g_i)(\mathbf{r}_0)$ be the stability matrix of $\mathbf{g}$ in $\mathbf{r}_0$ with eigenvalues ν_k. Since $\mathbf{r}_0$ is a stable stationary point of $\mathbf{g}$, the real parts of all eigenvalues ν_k are negative, $\mathrm{Re}(\nu_k) < 0$. We now turn to the change of the stability properties accompanying the discretisation. A stable stationary point of a time–continuous system does not turn automatically into a stable FP of the time–discrete system: The stability of the FP is related to the size of the time interval Δt of the discretisation. We switch from the time–continuous system $\mathbf{g}$ to the time–discrete system $\tilde{\mathbf{g}}$ with help of the Euler–discretisation $\dot{\mathbf{r}} \to (\mathbf{r}_{i+1} - \mathbf{r}_i)/(\Delta t)$ according to $\mathbf{r}_{i+1} = \mathbf{r}_i + (\Delta t)\mathbf{g}(\mathbf{r}_i) \equiv \tilde{\mathbf{g}}(\mathbf{r}_i)$. The point $\mathbf{r}_0$ is now a FP of $\tilde{\mathbf{g}}$. Its stability depends on the size of the time interval Δt in the following way: The eigenvalues of the stability matrix of the discretised system $\tilde{\mathbf{g}}$ are $\pi_k = 1 + \lambda\nu_k$. Even if the real part of the eigenvalues ν_i is negative, the condition $|\pi_i| < 1$ for stability of the FP of the discretised system is not met for arbitrary values of the parameter Δt. With decreasing value of Δt we can stabilise in the discretised system FPs with increasing instabilities, i.e. increasing absolute values of the eigenvalues μ_k. In the case of an infinitesimal Δt each stable stationary point of the time–continuous system $\mathbf{g}$ corresponds to a stable FP of the map $\tilde{\mathbf{g}}$.

Let us now discuss the relation of the eigenvalues of the original stability matrix $\mathbf{S}_h(\mathbf{r}_0)$ to the critical value λ_{crit}, marking the transition from instability to stability. For a stabilisation transformation with an arbitrary matrix $\mathbf{C}_i$ an exact relation cannot be established, since the multiplication of the stability matrix $\mathbf{S}_h(\mathbf{r}_0)$ with the matrix $\mathbf{C}_i$ implies a complicated alteration of the eigenvalues. However, numerical evidence shows that generically the absolute values of the eigenvalues of $\mathbf{S}_g(\mathbf{r}_0) = \mathbf{C}_i\mathbf{S}_h(\mathbf{r}_0)$ are, independent of $\mathbf{C}_i$, of the same order of magnitude compared to the eigenvalues of $\mathbf{S}_h(\mathbf{r}_0)$. This suggests a, at least approximate, relation in the form $\lambda_{crit} \approx \Lambda^{-1}$ of λ_{crit} to the eigenvalue Λ of $\mathbf{S}_h(\mathbf{r}_0)$ with the largest absolute value. This dependence will be discussed in section 5.3 for several examples of dynamical systems.

3.5 Modified ST approaches

For a number of studies described in this article a combination of the ST method with the Newton algorithm is advantageous to enhance the speed of convergence in the linear neighbourhood of the FP. These applications show that it is most promising to apply both algorithms successively. Nevertheless, attempts have been made to combine both methods in such a way that each iteration step is a linear superposition of steps of the individual two algorithms [303–305]. For detecting the zeros of $\mathbf{F}(\mathbf{r}) = \mathbf{f}^{(p)}(\mathbf{r}) - \mathbf{r}$, in both the Newton method and the ST method an iteration $\mathbf{r}_{\mathrm{new}} = \mathbf{r}_{\mathrm{old}} + \delta\mathbf{r}$ is performed. In the ST method, $\delta\mathbf{r}$ is given by $\delta\mathbf{r} = \lambda\mathbf{C}_i\mathbf{F}(\mathbf{r})$, whereas the Newton method yields $-\mathbf{J}(\mathbf{r})\delta\mathbf{r} = \mathbf{F}(\mathbf{r})$, with $\mathbf{J}(\mathbf{r}) = \partial\mathbf{F}/\partial\mathbf{r}$ being the Jacobian matrix. The approach according to ref. [303–305] combines these two methods following the ansatz

$$[\mathbf{1}\beta\|\mathbf{F}(\mathbf{r})\| - \mathbf{C}_i\mathbf{J}(\mathbf{r})]\,\delta\mathbf{r} = \mathbf{C}_i\mathbf{F}(\mathbf{r}) \tag{9}$$

with $\beta > 0$ being an adjustable parameter. This corresponds to the ST method for a larger distance to the FP and for sufficiently large values of β, maintaining the global convergence properties. However, close to an unstable FP the Newton algorithm dominates in Eqn. (9) and guarantees fast convergence. The application of this approach to several chaotic maps and the rate of its convergence have been studied [304, 305].

A fruitful modification of the ST method as discussed in this study is its combination with the so-called "subspace projection method" [306, 307]. It allows the detection of POs of higher dimensional systems with relatively small numerical effort. The n–dimensional local phase space of the dynamical system is decomposed into two invariant subspaces such that all directions that cannot be stabilised with the trivial stability transformation $\mathbf{C} = \mathbf{1}$ and an appropriate value of the parameter λ are contained in an invariant subspace with dimension d. The basis vectors $\boldsymbol{\xi}_i$ span this d-dimensional invariant subspace and are obtained by subspace iteration [306]. In order to locate the unstable PO, the following iteration is performed:

$$\mathbf{r}_{k+1} = \mathbf{r}_k + \sum_{i=1}^{d} a_i\boldsymbol{\xi}_i + \lambda\left[\mathbf{f}^{(p)}(\mathbf{r}_k) - \mathbf{r}_k - \sum_{i=1}^{d} b_i\boldsymbol{\xi}_i\right]$$

with

$$(a_1, a_2, ..., a_d)^T = \lambda'\mathbf{C}'(b_1, b_2, ..., b_d)^T$$

and

$$b_i = (\mathbf{f}^{(p)}(\mathbf{r}_k) - \mathbf{r}_k) \cdot \boldsymbol{\xi}_i$$

In the d-dimensional subspace all possible stability transformations are performed, applying the different possible $d \times d$-matrices $\mathbf{C}'$. The number of transformations to be applied is significantly smaller compared to the required number for the complete original dynamical system.

A more theoretical approach to the ST method is the attempt to subdivide the chaotic dynamics into cyclic elements [308]. This corresponds to a decomposition of the stability matrix into the individual permutation matrices. These permutation matrices are an invariant set under application of the matrices $\mathbf{C}_i$, which suggests a relation of the two approaches on a mathematical level.

4 Geometrical Interpretation of the Stability Transformations

4.1 Classification Scheme

In this chapter our goal is to gain a deeper insight into the geometrical meaning and the interpretation of the transformations $\mathbf{s}_i$ (Eqn. (5)) which turn unstable FPs into stable ones. In order to do this, one has to go beyond the exclusive consideration of the eigenvalues at the positions of the FPs.

We shall discuss a geometrical approach [302] allowing us to classify the FPs that are stabilised by different matrices $\mathbf{C}_i$. We will hereby focus on systems with two degrees of freedom. Expectedly there should be no major obstacles with respect to the generalisation to arbitrary dimensions.

In this section, we will again utilise a double index $(k\sigma)$ for the two-dimensional matrices $\mathbf{C}_i$. Its meaning will be illustrated in the following. Details of the classification scheme and its implications can be found in ref. [302].

When dealing with the ST method a natural problem arises: Restricting ourselves to the set of orthogonal $\mathbf{C}_{k\sigma}$–matrices with exactly one non-vanishing entry ± 1 in each row and column and confining ourselves to the linearised dynamics around a FP, what can we say about the action of the matrices $\mathbf{C}_{k\sigma}$ on this simple dynamical system? The following equations describe the time–continuous version of the ST method

$$\dot{\mathbf{r}} = \mathbf{F}(\mathbf{r}) \quad , \qquad \mathbf{F}(\mathbf{r}) = \mathbf{f}^{(p)}(\mathbf{r}) - \mathbf{r} \quad , \qquad \mathbf{F}(\mathbf{r}) = (F_1(\mathbf{r}), F_2(\mathbf{r}))^T \tag{10}$$

as discussed in section 3.4. It describes a vector field $\mathbf{F}(\mathbf{r})$ around the FP $\mathbf{r}_0$ with $\mathbf{F}(\mathbf{r}_0) = \mathbf{0}$. Applying the stabilisation transformation we obtain the system

$$\dot{\mathbf{r}} = \mathbf{C}_{k\sigma} \cdot \mathbf{F}(\mathbf{r}) \tag{11}$$

Multiplication with a matrix $\mathbf{C}_{k\sigma}$ can either change the sign of the components $F_1(\mathbf{r})$ and $F_2(\mathbf{r})$, independently or it can exchange both components, altering the eigenvalues and eigenvectors of the corresponding stability matrix $(\mathbf{T}_\mathbf{F})_{ij} = \frac{\partial F_i}{\partial r_j}$ in general in a non-perturbative way. We are interested in a classification of the stability matrices, i.e. of the corresponding FPs, with respect to their stability eigenvalues and in particular with

respect to the changes they undergo in applying the transformation. To approach this problem, the following definition of an invariant set of points (see e.g. [240]) is useful: $\mathbf{C}_{k\sigma}$ acting on the manifolds Z_1, Z_2 defined as

$$Z_i = \{ \mathbf{r} \mid F_i(\mathbf{r}) = 0 \}, \quad i = 1, 2,$$

they are either mapped onto themselves if $\mathbf{C}_{k\sigma}$ does not interchange the components, or they are mapped onto each other if $\mathbf{C}_{k\sigma}$ interchanges the components. In this sense, the manifold $Z = Z_1 \cup Z_2$ is invariant with respect to the application of the set of matrices $\mathbf{C}_{k\sigma}$, i.e. $\mathbf{C}_{k\sigma}(Z) = Z$ for all $(k\sigma)$. In the linear approximation of the dynamics in the neighbourhood of $\mathbf{r}_f$ these sets clearly define straight lines and intersect in the FP: $Z_1 \cap Z_2 = \{\mathbf{r}_0\}$.

As mentioned above, we derive in the following a classification scheme for the linearised dynamics around a FP in order to understand the mechanism of the stability transformation. To this aim, we introduce two ways of classifying the stability matrices of a two–dimensional system, using certain geometrical properties of the flow around the FP. These properties reflect on the one hand different invariant sets Z and on the other hand additional geometrical properties of matrices with a common invariant set Z.

The first classification refers to matrices which have a common invariant manifold $Z = Z_1 \cup Z_2$. The sets of matrices are divided into classes labelled $\mathcal{C}(\phi_{\min}, \phi_{\max})$, where $\phi_{\min}$ and $\phi_{\max}$ are the polar angles of the manifolds Z_1 and Z_2 in the linear approximation, respectively, being sorted with increasing value. If a stability matrix $\mathbf{B}$ belongs to the class $\mathcal{C}(\phi_{\min}, \phi_{\max})$ then also the products $\{\mathbf{C}_{k\sigma} \cdot \mathbf{B}\}$ belong to this class.

For the later discussion we introduce three sets of FPs (i.e. matrices) each of which is an unification of classes $\mathcal{C}(\phi_{\min}, \phi_{\max})$:

$$\begin{aligned}
\mathcal{C}^1 &= \{\cup\, \mathcal{C}(\phi_{\min}, \phi_{\max}) |\ 0 < \phi_{\min}, \phi_{\max} < \pi/2\} \\
\mathcal{C}^2 &= \{\cup\, \mathcal{C}(\phi_{\min}, \phi_{\max}) |\ 0 < \phi_{\min} < \pi/2 < \phi_{\max} < \pi\} \\
\mathcal{C}^3 &= \{\cup\, \mathcal{C}(\phi_{\min}, \phi_{\max}) |\ \pi/2 < \phi_{\min}, \phi_{\max} < \pi\}
\end{aligned} \tag{12}$$

To derive a second classification, we assign a label $(l\tau)$ to each stability matrix $\mathbf{B}_{l\tau}$ with $\tau = \pm 1$ providing the sign of $\det(\mathbf{B}_{l\tau})$ and $l = (m + \tau - 1) \mod 4$, with $m = 0, ..., 3$ indicating the four possible values $(m\,\pi)/2$ of the polar angle of $\mathbf{F}(\phi_{\min})$. Now we define

the class $\mathcal{A}_{l\tau}$ as the set of all matrices $\{\mathbf{B}_{l\tau}\}$ with $0 \leq \phi_{\min} < \phi_{\max} \leq 2\pi$ varying within each class. For fixed $\phi_{\min}, \phi_{\max}$, multiplication by a matrix $\mathbf{C}_{k\sigma}$ transfers one complete class $\mathcal{A}_{l\tau}$ into another class $\mathcal{A}_{l'\tau'}$. The corresponding transitions $\mathcal{A}_{l\tau} \longrightarrow \mathcal{A}_{l'\tau'}$, with $l' = (k + \sigma l) \bmod 4$ and $\tau' = \sigma \cdot \tau$, are given in Table 2. The common algebra of the indices of the matrices $\mathbf{C}_{k\sigma}$ (see Eqn. (7)) and the classes $\mathcal{A}_{l\tau}$ justifies the introduction of the double index $(k\sigma)$ for the stabilising matrices.

To gain relevant information on the stability properties of FPs it suffices, as we shall see in the following, to know to which of the sets $\mathcal{C}^i$ and $\mathcal{A}_{l\tau}$ the stability matrix of the FP belongs.

4.1.1 Properties of the angular functions $\psi(\phi)$ of the flow and examples

Let us consider an arbitrary but fixed stability matrix $\mathbf{B}_{l\tau} \in \mathcal{A}_{l\tau}$. Each of the matrices $\mathbf{C}_{k\sigma} \cdot \mathbf{B}_{l\tau}$, $k = 0, ..., 3; \sigma = \pm 1$ is an element of a different class $\mathcal{A}_{l'\tau'}$. We have

$$\mathbf{B}_{l'\tau'} = \mathbf{C}_{k\sigma} \cdot \mathbf{B}_{l\tau} \quad \text{with} \quad l' = (k + \sigma l) \bmod 4 \quad \text{and} \quad \tau' = \sigma \cdot \tau \tag{13}$$

In the following we will call the set $\{\mathbf{B}_{l\tau} | l = 0, ..., 3; \tau = \pm 1\}$ the family of the matrix $\mathbf{B}_{l\tau}$. It is the central issue to analyse which elements of the family of a FP are stable.

In order to do this, we study in the following the orientational properties of the flow around a FP for a family of stability matrices with arbitrary $(\phi_{\min}, \phi_{\max})$. For the family of the matrix $\mathbf{B}_{l\tau}$ we introduce the angular functions $\psi_{l\tau}(\phi)$, representing the polar angle of the flow $\dot{\mathbf{r}} = \mathbf{B}_{l\tau} \cdot \mathbf{r}$ at a point $\mathbf{r} = (\cos\phi, \sin\phi)^T$ (see Fig. 3). $\psi_{l\tau}(\phi)$ is a continuous function of ϕ with $\psi_{l\tau}(\phi) \in [0, 2\pi]$. Due to symmetry it is sufficient to consider the range $0 < \phi < \pi$. Furthermore, $\psi_{l\tau}(\phi)$ is defined mod 2π and $\psi_{l\tau}(0) - \psi_{l\tau}(\pi) = \pi$. Two functions $\psi_{l\tau}(\phi)$ and $\psi_{l'\tau}(\phi)$ differ only by a shift $\psi_{l\tau}(\phi) - \psi_{l'\tau}(\phi) = (l - l' \bmod 4) \cdot \frac{\pi}{2}$. Furthermore we have $\psi_{l\tau}(\phi) = 2 \cdot \psi_{l\tau}(\phi_{\min}) - \psi_{l-\tau}(\phi)$.

As an illustrative example, Fig. 4a) and Fig. 5a) show the eight elements of the family of the stability matrix $\mathbf{M}_1 = \left(\begin{smallmatrix} 1 & -4 \\ -10 & 5 \end{smallmatrix}\right)$ belonging to the class $\mathcal{C}^1$. Fig. 6a) and Fig. 7a) are obtained in the same way, showing the family of $\mathbf{M}_2 = \left(\begin{smallmatrix} 1 & -4 \\ 10 & 5 \end{smallmatrix}\right)$ belonging to the class $\mathcal{C}^2$. Each sub-figure shows the linear neighbourhood of the corresponding FP. In Figs. 4b) through 7b) the corresponding angular functions $\psi_{l\tau}(\phi)$ are plotted.

The examples in Figs. 4a) through 7a) except the cases of spiral points $\mathbf{B}_{1+}$ and $\mathbf{B}_{3+}$ suggest a criterion for the stability and approximate position of the eigenvectors of the

FPs: Since the flow $\mathbf{F}(\mathbf{r})$ in $\mathbf{r} = \mathbf{r}(\phi) = (\cos\phi, \sin\phi)^T$ is a continuous vector function of the polar angle ϕ, there have to be certain values ϕ_e for which the flow $\mathbf{F}(\mathbf{r}(\phi_\mathbf{e}))$ is collinear with the position vector, i.e. $\mathbf{F}(\mathbf{r}) = \lambda \cdot \mathbf{r}$, $\lambda \in \mathbb{R}$. This implies

$$\psi_{l\tau}(\phi_e) = \begin{cases} \phi_e & : \quad \lambda > 0, \quad \text{unstable eigenvector} \\ \phi_e + \pi & : \quad \lambda < 0, \quad \text{stable eigenvector} \end{cases}$$

The angles ϕ_e are the polar angles of the eigenvectors of the corresponding stability matrix. An intersection of $\psi_{l\tau}(\phi)$ with the line $\chi_n(\phi) = \phi + n \cdot \pi$, $n = 0, 1$ indicates an unstable or stable eigenvector for the corresponding value of ϕ, respectively.

4.1.2 Stability properties of the classes

We now discuss the properties of all possible stability matrices according to their $\psi_{l\tau}(\phi)$–diagrams, which is done by simple application of continuity arguments to the functions $\psi_{l\tau}(\phi)$: In Figs. 4c) through 7c) we show those areas in the $\psi_{l\tau}(\phi)$–diagrams where a intersection of $\psi_{l\tau}(\phi)$ and $\chi_0(\phi)$ or $\chi_1(\phi)$ may occur as grey shaded boxes. However, the function $\psi_{l\tau}(\phi)$ of stability matrices related to spiral points do not intersect $\chi_0(\phi)$ or $\chi_1(\phi)$ (they do not have real eigenvectors), therefore an additional criterion is needed to analyse their stability. Numerical studies suggest that for spiral FPs the line $\chi_n(\phi)$ which is closest to $\psi_{l\tau}(\phi_t)$ in terms of a suitably defined distance (see ref. [302]) determines the stability. This can be seen as a generalisation of the criterion of the crossing with $\chi_n(\phi)$ in the case of real eigenvalues.

We begin our discussion with stability matrices $\mathbf{B} \in \{\mathcal{A}_{l-} | l = 0...3\}$ with negative determinants which are stability matrices of saddle points. The stability properties of these FPs are easy to determine from the corresponding $\psi_{l\tau}(\phi)$– diagrams in Figs. 5b) and 7b). Since the $\psi_{l\tau}(\phi)$–curves are monotonous and continuous, they intersect the lines $\chi_0(\phi)$, $\chi_1(\phi)$ exactly once. The sectors where the corresponding eigenvectors are localised are shaded grey in the corresponding phase diagrams Figs. 5c), 7c).

FPs with positive determinant $\mathbf{B}$ belonging to the classes $\{\mathcal{A}_{l+} | l = 0...3\}$ are a bit more difficult to judge. They include sinks and sources as well as spiral points. We first address the sinks and sources. The corresponding curves $\psi_{l\tau}(\phi)$ intersect either of the lines $\chi_0(\phi)$ (sink) or $\chi_1(\phi)$ (source) twice. It is important to note that there cannot be more than two crossings, which can also be seen formally [302].

We now distinguish the properties of the stability matrices with positive determinant with respect to their assignment to the classes $\mathcal{C}^1$, $\mathcal{C}^2$, and $\mathcal{C}^3$:

As can be read off directly from the Figs. 4b) and c), matrices in $\mathcal{C}^1 \cap \mathcal{A}_{0+}$ and $\mathcal{C}^1 \cap \mathcal{A}_{2+}$ are always sinks and sources, respectively. Matrices of the class $\mathcal{C}^1 \cap \mathcal{A}_{1+}$ and $\mathcal{C}^1 \cap \mathcal{A}_{3+}$ can be either sinks and sources or spiral points. For real eigenvalues, matrices of $\mathcal{C}^1 \cap \mathcal{A}_{1+}$ are sinks whereas matrices in $\mathcal{C}^1 \cap \mathcal{A}_{3+}$ are sources. In the case of spiral points, we can at least say that either $\mathbf{B}_{1+}$ is a stable and $\mathbf{B}_{3+}$ is an unstable spiral point or vice versa. This analysis applies to the class $\mathcal{C}^3$ in an analogous way. The classes $\mathcal{C}^2 \cap \mathcal{A}_{k+}$ may have the same configuration as the classes $\mathcal{C}^1 \cap \mathcal{A}_{k+}$ and $\mathcal{C}^3 \cap \mathcal{A}_{k+}$, but may additionally be composed of four spiral points (two stable and two unstable).

We thus have shown that for a given class $\mathcal{A}_{l\tau}$ two complete classes $\mathcal{A}_{l'\tau'}$ and $\mathcal{A}_{l'',\tau''}$ are related to stable FPs, i.e. the family of an arbitrary stability matrix $\mathbf{B}_{l\tau}$ contains two stable matrices $\mathbf{B}_{l'\tau'}$ and $\mathbf{B}_{l''\tau''}$. The transformations of $\mathcal{A}_{l\tau}$ into $\mathbf{B}_{l'\tau'}$ and $\mathbf{B}_{l''\tau''}$ is achieved by two matrices $\mathbf{C}_{k'\sigma'}$ and $\mathbf{C}_{k''\sigma''}$ (to be read off the transition table 2) which transfer the original stability matrix $\mathbf{B}_{l\tau}$ in a class $\mathcal{A}_{l\tau}$ into the desired stable matrices in $\mathbf{B}_{l'\tau'} \in \mathcal{A}_{l'\tau'}$ and $\mathbf{B}_{l''\tau''} \in \mathcal{A}_{l''\tau''}$. This corresponds to a transformation of the original unstable FPs into the desired stable ones in the transformed dynamical systems $\mathbf{s}_{k'\sigma'}$ and $\mathbf{s}_{k''\sigma''}$.

4.2 Minimal sets

Now we turn to the minimal sets $\mathcal{S}$ of matrices $\mathbf{C}_{k\sigma}$ necessary for the stabilisation of all FPs of a two-dimensional chaotic dynamical system. Let us first consider the classes $\mathcal{A}_{l\tau} \cap \mathcal{C}^i$, $i = 1, 2, 3$ with elements corresponding to stable FPs. We introduce the notation $(l\tau, l'\tau')$ abbreviating the two stable classes $\mathcal{A}_{l\tau}$ and $\mathcal{A}_{l'\tau'}$ for any $\mathcal{C}^i$.

$$\begin{aligned} \mathcal{C}^1 \text{ and } \mathcal{C}^3 &: \quad (1+, 2+) \quad \text{or} \quad (2+, 3+) \\ \mathcal{C}^2 &: \quad (1+, 2+) \quad \text{or} \quad (2+, 3+) \quad \text{or} \quad (3+, 0+) \end{aligned} \tag{14}$$

When looking for the minimal set of matrices $\mathbf{C}_{k\sigma}$ necessary for complete stabilisation one has to take into account that only saddle points and sinks can occur in the system $\dot{\mathbf{r}} = \mathbf{F}(\mathbf{r})$ of Eqn. (10).

Let us discuss the set $\mathcal{S}_{saddle}$ of matrices $\mathbf{C}_{k\sigma}$ which stabilise saddle points first. Since

the determinant of the stability matrix is negative for a saddle point (and positive for any stable sink or spiral point), the corresponding stabilising matrix $\mathbf{C}_{k\sigma}$ has the form $\mathbf{C}_{k-}$. It is our aim to stabilise all saddle points of the classes $\mathcal{C}^1$, $\mathcal{C}^2$, and $\mathcal{C}^3$ with matrices $\mathbf{C}_{k\sigma}$ in $\mathcal{S}_{saddle}$. Therefore, we have to determine $\mathcal{S}_{saddle}$ in such a way that any class $\mathcal{A}_{l-}$ of original matrices is transferred into at least one element in each of the pairs $(1+, 2+)$ or $(2+, 3+)$ or $(3+, 0+)$ (see Eqn. (14)). According to the transition table 2 there are two possibilities: $\mathcal{S}_{saddle} = \{\mathbf{C}_{0-}, \mathbf{C}_{2-}\}$ or $\{\mathbf{C}_{1-}, \mathbf{C}_{3-}\}$. $\mathcal{S}_{saddle}$ has to be combined with sets $\mathcal{S}_{sink}$ that stabilise the sinks to yield a possible minimal set $\mathcal{S} = \mathcal{S}_{saddle} \cup \mathcal{S}_{sink}$. Since sinks are already stable, the identity transformation $\mathcal{S}_{sink} = \{\mathbf{C}_{0+}\}$ is sufficient. Indeed, it is easy to see that no other matrix $\mathbf{C}_{k\sigma}$ is able to achieve the same [302]. We end up with two minimal sets:

$$\mathcal{S}_1 = \{\mathbf{C}_{0+}, \mathbf{C}_{0-}, \mathbf{C}_{2-}\} \quad \text{and} \quad \mathcal{S}_2 = \{\mathbf{C}_{0+}, \mathbf{C}_{1-}, \mathbf{C}_{3-}\}$$

There are other sets which also do the job, but they contain at least four matrices and are therefore not minimal.

5 Implementing the ST method and application to maps

This section discusses the application of the ST method to the detection of unstable POs in time discrete dynamical systems (maps). We discuss several improvements of the numerical implementation originally explained in refs. [300, 301, 309] in order to enhance the efficiency. We proceed with a twofold goal: Firstly, we are interested in getting complete sets of unstable POs with increasing length, discussing also the resulting distribution of their Lyapunov exponents. A second focus will be the discussion of the ability of the ST method to locate the least unstable POs of a map up to a given period p [309].

5.1 Detection of fixed points

For an efficient algorithmic implementation of the ST method for time-discrete maps, we focus on two main issues:

1) Detection of complete sets of unstable POs of a given length p.

2) Separation of closely neighboured POs of the same length p.

Since most of the maps studied here are two-dimensional, we describe the application of the ST method to two-dimensional systems. However, the procedure works equally well for higher dimensions. The necessary adjustments for adaption to systems of higher dimensionality concern solely the $\mathbf{C}_i$-matrices and their minimal set.

5.1.1 Detection of complete sets of periodic orbits

The basins of attraction for the POs in the stability transformed maps are of fractal and fibre-like structure and form a densely interwoven network. The transversal extension of these fibres shrinks along with their longitudinal stretching. The corresponding fractal-like structure can be observed on length scales covering several orders of magnitude. These features make a complete detection of all FPs more difficult. However, a clever choice of the set of initial points, i.e. of the covering of the phase space of the dynamical system, can significantly reduce the probability of missing individual POs. Additionally

convergence tests (see below) allow to gain further confidence in the completeness of the results.

To detect complete sets of POs of length p we proceed as follows: We introduce a set of grids G_i, $i = 1, 2, ...$ of initial points, which are cumulative in the following way: Initial points in G_i fill gaps larger than a given size in the union $G_1 \cup G_2 \cup ... \cup G_{i-1}$ of the proceeding grids in the sequence. The points of G_i are taken from a chaotic trajectory on the attractor of the system. For the two-dimensional Ikeda map (see section 5.2) a sequence of six grids G_1,...,G_6 is created, G_1 containing 4500 points, G_i, $i = 2, ..., 6$ containing 1500 points each. The points of each grid G_i are then propagated with the transformed maps, employing the minimal sets studied in section 4.2, for example $\mathbf{s}_{0+}$, $\mathbf{s}_{0-}$, and $\mathbf{s}_{2-}$, i.e. the matrices $\mathbf{C}_{0+}$, $\mathbf{C}_{0-}$ and $\mathbf{C}_{2-}$. The propagation of a transformed trajectory is stopped in a point $\mathbf{r}$ as soon as the step size $|\mathbf{f}^{(p)}(\mathbf{r}) - \mathbf{r}| < \epsilon$ is reached, ϵ being the desired accuracy of the position of the FP. The accuracy ϵ is primarily determined by the necessity to distinguish different closely neighbouring POs. To make this distinction for the Ikeda map, an accuracy of $\epsilon < 10^{-10}$ was sufficient to find all POs of length $p = 14$ and $p = 15$. Propagation of the points of the grid G_i with $\mathbf{s}_{0+}$, $\mathbf{s}_{0-}$ and $\mathbf{s}_{2-}$ results in the sets $N_{i,0+}$, $N_{i,0-}$ and $N_{i,2-}$, $i = 1, ..., 6$, of points that are, within a finite number of digits, FPs of the transformed, p-times iterated map $\mathbf{f}^{(p)}$. The set $N_i = N_{i,0+} \cup N_{i,0-} \cup N_{i,2-}$ contains the FPs of the map found by propagating the points of the grid G_i. In order to test the completeness of the set of FPs already found, we consider the number $n_{i,k\sigma}$ of FPs appearing in a given $N_{i,k\sigma}$ (and therefore also in N_i), with $(k\sigma) = (0+), (0-), (2-)$, but not in any other N_j, $j < i$. In case no additional FP is found when propagating another grid, i.e. $n_{i-1,k\sigma} = n_{i,k\sigma} = 0$, the set of FPs of the transformed systems $\mathbf{s}_{k\sigma}$ is considered to be complete and a propagation of a further grid G_i is not necessary. Of course this is an empirical procedure which does not provide a rigorous proof of completeness.

5.1.2 Separation of periodic orbits

A second detail of the numerical implementation is the procedure to separate closely neighboured POs. To this aim, we define a distance d_{xy} between two POs of length p,

$\mathbf{x}_i = (x_{1i}, x_{2i})$, $\mathbf{y}_i = (y_{1i}, y_{2i})$, $i = 1, \ldots, p$:

$$d_{xy} = \min_{\substack{k=0,\ldots \\ \ldots,p-1}} \sum_{\substack{1 \le i \le p \\ j=1,2}} \left(x_{ji} - y_{j(i+k \bmod p)}\right)^2 \tag{15}$$

We now consider the generic case of a set of FPs belonging to different POs of the same length p. These FPs are found by propagating the transformed systems $\mathbf{s}_{0+}$, $\mathbf{s}_{0-}$ and $\mathbf{s}_{2-}$, as described in the preceding section. All possible combinations of two FPs determined numerically up to the given accuracy are formed and the individual distances d_{xy} of each pair are calculated. The distribution of the values of d_{xy} (which can be visualised well in a log plot, see Fig. 8) forms three subsets, which are separated by distances of several orders of magnitude. The subset with the largest value of d_{xy} contains pairs generated from distinct POs. The second and third subset (with decreasing values of d_{xy}) are composed by pairs of points belonging to the same orbit. Due to the finite accuracy of any converged numerical trajectory, the two points in the pair do not have the same position.

It is possible to judge from the distribution of d_{xy} whether the propagation has still to be continued in order to separate identical and different POs: In case the d_{xy}-diagram (e.g. Fig. 8) shows not a sufficiently distinct separation between the first and second subgroup (i.e. if the corresponding values of d_{xy} differ only by one order of magnitude or even less), the acquired accuracy does not allow a reliable separation of POs and the propagation of the corresponding transformed systems has to be continued.

The large separation of the two subsets with small values for d_{xy} is particularly interesting. A possible explanation for the large gap is the following: A trajectory of the transformed map approaches the FP on a curve which, close to the FP, agrees to a large extent with the least stable manifold of the FP. Two trajectories $\{\mathbf{y}_i\}$ and $\{\mathbf{z}_i\}$ converging to the same FP $\mathbf{r}_0$ evolve on a line that contains the FP. However, they can approach the FP in two ways: The two trajectories can either be on the same side or on opposite sides of the FP. The same configuration holds for all points of an orbit $\mathbf{f}^{(r)}(\mathbf{r}_0)$, $r = 1, ..., p-1$. In case of an approach from opposite sides to the FP, the contributions to d_{xy} are much larger compared to the case of an one-sided approach. This implies a relatively large distance d_{xy} in the second subset compared to the third subset (see Fig. 8).

In addition, the distribution of distances d_{xy} can be employed to get an estimate for

the absolute accuracy of the numerically obtained coordinates of the POs: The maximal distance between two coordinates assigned to the same PO within the limits of accuracy is given by the value of the top edge of the second subset in the distribution of the distances d_{xy}. Their (mean) distance is therefore a good guess for the distance of each trajectory to the FP itself.

5.2 Example: Complete sets of periodic orbits and their Lyapunov exponents

The ST method has been applied with considerable success to a number of time discrete dynamical systems (maps). To provide a first example, we discuss the detection of complete sets of POs of the Ikeda map $\mathbf{r}_{i+1} = \mathbf{f}(\mathbf{r}_i)$, $\mathbf{r}_i = (x_i, y_i)$ [310, 311],

$$\begin{aligned} x_{i+1} &= \alpha + \beta(x_i \cos w_i - y_i \sin w_i) \\ y_{i+1} &= \beta(x_i \sin w_i + y_i \cos w_i) \end{aligned} \tag{16}$$

with $w_i = \gamma - \frac{\delta}{1+x_i^2+y_i^2}$. The attractor we are referring to appears for the parameter values $\alpha = 1.0$, $\beta = 0.9$, $\gamma = 0.4$ and $\delta = 6.0$. Applying the ST method, complete sets of POs of length $p = 1, 2, ..., 15$ have been detected (see Tab. 3) [300, 301].

An indication of the completeness of the set of POs is the convergence of the topological entropy $h = \lim_{p \longrightarrow \infty} h_p$ with $h_p = \ln n(p)/p$ and $n(p)$ being the number of the FPs of all orbits of length p. For the Ikeda map, the topological entropy h seem to converge to a fairly constant value.

A few remarks concerning the application of the ST method to the Ikeda map are in order: Since each point of a PO of the system $\mathbf{f}^{(p)}(\mathbf{r}) - \mathbf{r}$ derived from the Ikeda map $\mathbf{f}(\mathbf{r})$ is stabilised by two $\mathbf{C}_{k\sigma}$-matrices, possessing a positive or a negative determinant, respectively (see section 4.1.2), we can group the FPs of a PO of length p into two sets:

$$S_+(p) \;:\; \text{Sinks, stabilised either by } \mathbf{C}_{0+},\ \mathbf{C}_{1+},\ \mathbf{C}_{2+},\ \text{or } \mathbf{C}_{3+} \tag{17}$$

$$S_-(p) \;:\; \text{Saddles, stabilised either by } \mathbf{C}_{0-},\ \mathbf{C}_{1-},\ \mathbf{C}_{2-},\ \text{or } \mathbf{C}_{3-} \tag{18}$$

Surprisingly the sets $S_+(p)$ and $S_-(p)$ contain the same number of points $|S_+(p)| = |S_-(p)|$ for any period $p = 1...15$. The corresponding numbers are $|S_\pm(p)| = 1,\ 2,\ 4,\ 8,\ 11,\ 26,$

36, 64, 121, 242, 419, 692, 1262, 2256, 4259 for $p = 1 - 15$. This remarkable symmetry suggests a close relation between the POs of the map: Each PO with a stability matrix having a positive determinant is strongly correlated to exactly one other orbit whose stability matrix has negative determinant. This observation agrees with another interesting pairing feature we made when analysing the distribution of Lyapunov exponents of POs of the Ikeda map [312]: There exist pairs of orbits, one belonging to S_+, the other one to S_-, with nearly the same Lyapunov exponent. This indicates a fundamental symmetry of the Ikeda map (not necessarily of geometrical origin). This phenomenon may have an explanation within the index theory [313]. However, the corresponding theorems concerning the existence, number and properties of FPs are rather exclusive and cannot be applied directly to the Ikeda map.

We now turn to the discussion of the distribution of Lyapunov exponents $\Lambda = \log(|\rho|)/p$ of the unstable POs. Here, ρ is the largest eigenvalue of the matrix $\mathbf{M} = \mathbf{M}_p \cdot \ldots \cdot \mathbf{M}_2 \cdot \mathbf{M}_1$, with $\mathbf{M}_i$ being the stability matrix in the i-th point of the PO. The normalised distribution $D(\Lambda)$ of the Lyapunov exponents Λ of all POs is shown in Fig. 9 both for the Ikeda map Eqn. (16) for periods $p = 12, \ldots, 15$ and for the Hénon map [27] given by

$$\begin{aligned} x_{i+1} &= 1.4 - x_i^2 + 0.3 y_i \\ y_{i+1} &= x_i \end{aligned}$$

for periods $p = 24, \ldots, 27$. The Lyapunov distributions of both maps become narrower with increasing length p. The maximum of the distribution is at $\Lambda_{\max} = 0.5$ for the Hénon map and at $\Lambda_{\max} = 0.68$ for the Ikeda map. Around the maximum, the distribution is generally Gaussian [3, 314]. However, globally the distributions deviate from this behaviour.

- Both distributions are not symmetric: The branches $\Lambda < \Lambda_{\max}$ of the distributions are significantly more spread compared to the branches $\Lambda > \Lambda_{\max}$
- The width of the distributions is significant. However, there exist also isolated peaks. For the Hénon distribution, the most pronounced peaks are at $\Lambda = 0.551$ and $\Lambda = 0.435$. The length of the orbits considered for the Ikeda map, $p = 15$, seems however to be too small to provide similar arguments.

For further analysis we refer the reader to ref. [312].

5.3 "Stability Ordering" of periodic orbits

The ST method is based on the systematic transformation of the stability properties of a dynamical system. Thus it is not surprising that the parameter λ of the algorithm is of central importance for the stability of the correspondingly stabilised POs. The following considerations concern two-dimensional maps, but there is numerical evidence of their validity also for higher-dimensional systems. Let us denote by $\Lambda_{orb}^{(j)}$ the Lyapunov exponent of an unstable PO, the index j labelling the orbit. Let us define a critical value $\lambda_{k\sigma,i}$ of the parameter of a point $\mathbf{r}_i$ of a periodic orbit stabilised by a matrix $\mathbf{C}_{k\sigma}$ as the largest value of λ, such that all eigenvalues of the transformed stability matrix $\mathbf{T}_{s_{k\sigma}}(\mathbf{r}_i)$ in the point $\mathbf{r}_i$ possess an absolute value less than one.

The critical value $\lambda_{k,i}$ marks the borderline between stability and instability. It is related to the Lyapunov exponent $\Lambda_{orb}^{(j)}$ of an unstable PO j: A decrease of the parameter λ, starting from the critical value, implies the stabilisation of an increasing number of unstable POs, including orbits that are more and more unstable. This relation is strictly monotonous in the case of the ST transformation using the identity matrix $\mathbf{C}_{0+}$ and has an at least monotonous tendency for the other transformations [309]. For the latter case, numerical studies suggest that a slightly different definition of a critical value of λ results in a better overall monotonous tendency: We now consider all points $\mathbf{r}_i^{(j)}$, $i = 1...p$ of an orbit j of given length p, which are in general stabilised by different $\mathbf{C}_{k\sigma}$–matrices implying different critical values $\lambda_{k\sigma,i}^{(j)}$. We apply *all* eight $\mathbf{C}_{k\sigma}$–matrices for the stabilisation. As explained in section 4.1.2, each point $\mathbf{r}_i^{(j)}$ of the orbit is stabilised by two matrices, $\mathbf{C}_{k\sigma}$ and $\mathbf{C}_{k'\sigma'}$, with in general different values $\lambda_{k\sigma,i}^{(j)}$. Each orbit therefore corresponds to a set of $\mathbf{C}_{k\sigma}$–matrices stabilising the p different points of the orbit, resulting in $2p$ values $\lambda_{k\sigma,i}^{(j)}$. Let us denote the largest critical parameter of this set by $\lambda_{\max}^{(j)}$. Numerical investigations indicate that the distribution of the Lyapunov exponents $\Lambda_{orb}^{(j)}$ of the POs are ordered relatively strictly with respect to the respective $\lambda_{\max}^{(j)}$. Fig. 10 shows the corresponding distributions for the Ikeda map on a logarithmic scale and for different lengths $p = 10, ..., 15$ of the POs. The distributions of the stability coefficients $\Lambda_{orb}^{(j)}$ of the stabilised orbits of a given length p show a clear tendency of a monotonic ordering: The smaller $\lambda_{\max}^{(j)}$ is, the more unstable the POs can be while still being detectable. The areas shaded grey in each of the sub-figures indicate the regions in which the eigenvalues $\Lambda_{orb}^{(j)}(\lambda_{\max}^{(j)})$

of period $p = 15$ are located. With increasing p the ordering of the POs with respect to their stability as a function of the parameter λ becomes increasingly stricter.

This observation, verified empirically also for other nonlinear dynamical systems, *allows to detect a given number of the least unstable periodic orbits of a map in a systematic way:* In order to detect the N least unstable POs of a given map, essentially a series of ST transformations as outlined in section 5.1.1 is performed. However, the value of $\lambda = \lambda_0$ is chosen relatively large and is then reduced step by step in a sequence of successive propagations of the same set of initial points. All $\mathbf{C}_{k\sigma}$–matrices are applied to obtain $\lambda_{\max}^{(j)}$. For the numerical implementation of this algorithm a sequence of grids $G_1, G_2, G_3, \ldots$ of initial points is introduced in such a way that an increasingly denser covering of the chaotic attractor is achieved according to section 5.1.1. The size of these grids has to be large enough to yield at least N unstable POs when propagated with all eight systems $\mathbf{s}_{k\sigma}$ (Eqn. (5)) and a value of $\lambda \approx \lambda_0/2$. For our studies of the Hénon map and Ikeda map 10 grids $G_1, \ldots, G_{10}$ with 20 initial points each proved to be sufficient. The algorithm can then be summarised into the following steps (beginning with $i = 1$, $\lambda_0 = 0.8$ is a good starting value):

1. Start with initial value $\lambda := \lambda_0$ and a grid G_i of initial points. Propagate G_i 8 times, using each time a differently transformed system according to Eqn. (5) with fixed value of λ and employing a different matrix $\mathbf{C}_{k\sigma}, k = 0, ..., 3$, $\sigma = \pm$ each time.

2. In case step 1. did not yield the desired number N of POs, replace $\lambda \longrightarrow r \cdot \lambda$, ($r < 1$, $r \approx 0.8$ seems to be a good choice) and repeat step 1. Otherwise continue with step 3.

3. Replace $G_i \longrightarrow G_{i+1}$, $\lambda_0 \longrightarrow r \cdot \lambda_0$ and start step 1 anew.

The algorithm is considered to be converged, if the number N of the least unstable POs found in the cumulative grid $H_i = G_1 \cup G_2 \cup ... \cup G_i$ is the same as in the cumulative grid $H_{i+1} = G_1 \cup G_2 \cup ... \cup G_{i+1}$.

Fig. 11 shows the Lyapunov exponents of the $N = 10$ least unstable POs of the Ikeda map and the Hénon map for the length $p = 1, ..., 36$. The distribution of these Lyapunov exponents agrees with the corresponding lower part of the distribution of the Lyapunov exponents in Fig. 9.

In Fig. 11, two features are remarkable:

- The Lyapunov exponents of the least unstable POs of both maps are of the same order of magnitude. This property does not depend on the actual value of p. An increase in p results for both maps in a reduction of the Lyapunov exponents of the ten least unstable POs. This goes hand in hand with a spreading of the distribution of the Lyapunov exponents of all unstable POs with increasing p. The mean of the total distribution, i.e. of all POs of a given length p, is the mean Lyapunov exponent $\bar{\Lambda}$ of the map, which is approximately independent of p. The inset in Fig. 11 shows the distribution of the least unstable POs on a log-log scale. Here, the lower edge of the distribution behaves almost linear. This implies that the width $W(p)$ of the distribution in Fig. 9 scales approximately like an algebraic function of the period p, i.e. $W(p) \propto p^{\eta}$, $\eta > 0$.

- For particular lengths p, both maps have certain POs with exceptionally small Lyapunov exponents. Examples are the Hénon map for $p = 13, 16, 18$ and $p = 26, 28, 30$ and the Ikeda map for $p = 19, 21$ and $p = 24, 27, 30$.

5.4 Application to time series

The global convergence pattern of the ST method allows to use it in order to *locate periodic orbits in even remarkably small sets of data, which may additionally be contaminated by noise.* This situation is often met when analysing short time series data of a dynamical system (Generally, longer time series and noiseless experimental data are technically more difficult to obtain). For a profound review concerning time series analysis, see ref. [315].

We focus on detecting FPs in a finite, n-dimensional time series $\{\mathbf{r}_i, i = 1, ..., n\}$ (the construction of a multidimensional time series from a one-dimensional signal is addressed elsewhere [316–318]). We proceed in three steps [300]:

First the so-called Voronoi diagram as the union of Voronoi zones is constructed, based on the set of data. The Voronoi zones cover the phase space in the following way: Each Voronoi zone contains exactly one point $\mathbf{r}_j$ of the time series. A point in phase space belongs to the Voronoi zone of the point of the time series closest to it. This way, the zones represent a tiling of the phase space. In order to obtain a dynamical system, each

zone is assigned the transfer vector $\mathbf{r}_{j+1} - \mathbf{r}_j$ of its corresponding data point $\mathbf{r}_j$. This yields a discontinuous, piecewise constant vector field $\mathbf{F}_V(\mathbf{r})$ that is in some respect a coarse grained version of the dynamical law underlying the time series. To detect POs in this system, we proceed by transforming $\mathbf{F}_V(\mathbf{r})$ according to Eqn. (5), considering it as an explicitly given map. The stabilised system is propagated, starting from a point randomly chosen in the phase space. The iteration according to Eqn. (5) yields a trajectory that converges in direction to a FP of the corresponding system. However, due to the special form of the vector field it does not converge in the FP, but lingers in its neighbourhood, trapped by a few Voronoi zones. For obvious reasons, it is clear that the trajectory can generally converge only in intersection points of the border lines of at least three different Voronoi zones. To find out this possible convergence point closest to the FP, a "freezing" of the dynamics is performed: While still propagating the system, the amplitude $|\mathbf{F}_V(\mathbf{r})|$ of the vector field is scaled to smaller and smaller values each m iterations ($m \approx 100$). This scaling smoothes the fluctuating dynamics while keeping the FPs in their place. The result is an adiabatic convergence of the trajectory to a common point of at least three Voronoi zones. Its coordinates are a good approximation for the position of the FP.

In the following example this algorithm is applied to a time series of just 100 points of the Ikeda map Eqn. (16). Fig. 12 shows the trajectory of the corresponding stability transformed system. The scaling procedure of the vector field and the resulting convergence of the trajectory is clearly visible in the zoomed section displayed in the panel to the right. The algorithm returned the coordinates $(0.536, 0.225)$ as the approximate position of the FP of the map, which is quite close to the actual values of $\mathbf{r}_0 = (0.53275, 0.24690)$. To detect the period-two FP, a vector field is constructed using a time series of 200 points. The obtained values $(0.52184, -0.55542)$ and $(0.57946, 0.51272)$ are to be compared with the accurate coordinates of $(0.50984, -0.60837)$ and $(0.62160, 0.60593)$, respectively.

Additionally, the influence of noise on the performance of the algorithm is studied. A noisy data set $\tilde{\mathbf{r}}_i = \mathbf{r}_i + \epsilon\, \boldsymbol{\xi}_i$ is used with $\mathbf{r}_i$ being the data set without noise. The parameter ϵ is varied from 0.1 to 0.3 ratios of root means square amplitudes of the attractor. For the variable $\boldsymbol{\xi}_i$ two kinds of noise are chosen: uniform noise in $(-1, +1)$ and Gaussian distributed noise with zero mean and a variance of 0.2. To improve statistics and to avoid singular configurations the algorithm was applied to 100 initial points chosen randomly

on the attractor. For the case of $\epsilon = 0.1$ and 0.3 rms a relative accuracy of the position of the FP of 4.5% and 16.1% is found for uniform noise and 4.0% and 6.3%, respectively, for Gaussian noise.

For further aspects of the application of the ST method to time series we refer the reader to ref. [300].

6 Periodic orbits in time-continuous systems

The ST method has been developed with the focus to detect unstable POs of time-discrete chaotic systems, i.e. maps. However, time-continuous systems represent an important class of dynamical systems and it is therefore desirable to modify the ST-approach such that it is applicable to this wide class. If the lengths of the unstable POs in time-continuous systems would be known exactly, one would simply apply a similar approach as in the case of time-discrete maps in order to detect them. Unfortunately, nothing is known about the periods of unstable POs in time-continuous chaotic systems in general.

Our strategy is therefore to reduce the time-continuous dynamics to a time-discrete map, whose FPs correspond to the continuous closed orbits of the system [319].

Let the time-continuous system be given by a system of ODEs,

$$\dot{\mathbf{r}} = \mathbf{F}(\mathbf{r}) \tag{19}$$

We consider the Poincaré map $\mathbf{f_F}(\mathbf{r})$ of the vector field $\mathbf{F}(\mathbf{r})$. To this aim, we introduce a hyper-plane as a Poincaré surface of section (PSS) in phase space and consider successive intersections of the continuous trajectory in the same direction as the Poincaré map. POs of the time-continuous system correspond to FPs of the Poincaré map, i.e. to FPs of the iterated Poincaré map.

When applying the ST method to the Poincaré-map using the different matrices $\mathbf{C}_i$ the convergence of a trajectory is fast for large distances to the FP. The step-size of the algorithm is proportional to $|\mathbf{f_F}(\mathbf{r}) - \mathbf{r}|$ and therefore decreases rapidly in the linear neighbourhood of the FP. This is not a major problem if generic maps are studied for which the calculation of the next iteration step is fast. For time-continuous systems, however, the situation is different. To determine the new intersection point with the PSS, the trajectories have to be integrated numerically for a time of the order of the expected period. In case of demanding high precision and/or if a relatively small parameter λ has to be applied for stabilising a highly unstable orbit, up to 10^6 iteration steps might be necessary for a successful convergence.

This problem can be solved to a good deal by a combination of the ST method and a slightly modified Newton algorithm. It significantly enhances the speed of convergence in the linear neighbourhood of the FP. The Newton method has the advantage of a super-

exponential convergence close to the FP, but its basins of attractions are rather small and covers little more than the linear neighbourhood. An suggestive procedure, which turned out to be very efficient in the systems we investigated so far, is to first propagate the stability transformed system until the trajectory reaches the linear neighbourhood of the FP. This point of time can be determined from the convergence pattern of the trajectory (in particular from the systematic decrease of the step size in a longer sequence of iterations). The Newton-procedure is then propagated until the desired accuracy is reached.

We now turn to some peculiarities of the implementation of the Newton algorithm which are particular for its application to Poincaré–maps (for details see ref. [43]). A linearisation of the dynamics $\dot{\mathbf{r}} = \mathbf{f_F}(\mathbf{r})$ in a point $\mathbf{r}$ yields a neighbouring point $\mathbf{r}'$

$$\mathbf{f_F}(\mathbf{r}') \approx \mathbf{f_F}(\mathbf{r}) + \mathbf{J}(\mathbf{r}' - \mathbf{r}) \tag{20}$$

with the stability matrix $\mathbf{J}$. To locate the FP $\mathbf{r}_o = \mathbf{f_F}(\mathbf{r}_o)$, we consider Eqn. (20) as an equality and set $\mathbf{f_F}(\mathbf{r}') = \mathbf{r}'$. We solve the equation

$$(\mathbf{1} - \mathbf{J})(\mathbf{r}' - \mathbf{r}) = -(\mathbf{r} - \mathbf{f_F}(\mathbf{r})) \tag{21}$$

for $\mathbf{r}'$. However, $\mathbf{r}'$ is generally not in the PSS, although $\mathbf{r}$ and $\mathbf{f_F}(\mathbf{r})$ are. In addition, an unit eigenvector of the matrix $\mathbf{J}$ in the direction of the flow impedes the inversion of the matrix $\mathbf{1} - \mathbf{J}$ in Eqn. (21). The first problem can be solved by adding a constraint equation requiring that $\mathbf{r}'$ to be in the PSS. For a hyper-plane as PSS with normal vector $\mathbf{a}$ this equation reads $\mathbf{a} \cdot (\mathbf{r}' - \mathbf{r}) = 0$. The second problem is dealt with by adding a small vector $\mathbf{F}(\mathbf{r})\delta T$ in direction of the flow $\mathbf{F}(\mathbf{r})$ to the vector in Eqn. (21), resulting in a shift of the corresponding eigenvalues away from one. The Newton algorithm Eqn. (21) now reads:

$$\begin{pmatrix} \mathbf{1} - \mathbf{J} & \mathbf{f_F}(\mathbf{r}) \\ \mathbf{a} & 0 \end{pmatrix} \begin{pmatrix} \mathbf{r}' - \mathbf{r} \\ \delta T \end{pmatrix} = \begin{pmatrix} -(\mathbf{r} - \mathbf{f_F}(\mathbf{r}) \\ 0 \end{pmatrix} \tag{22}$$

Inverting the matrix on the left hand side of Eqn. (22) yields the new position $\mathbf{r}'$ which results from the old position $\mathbf{r}$ after an iteration step of the algorithm. For additional comments and details of this method see ref. [43].

We will illustrate the applications of the ST approach to time-continuous dynamical systems in the following sections for three rather different examples: The dissipative

Lorenz system, the classical Hydrogen atom in a magnetic field and the classical Helium atom in a time-dependent electric field.

6.1 The Lorenz-system

6.1.1 Properties of the system

The so-called Lorenz system has its origin in a three-dimensional model of atmospheric convection. The equations of motion are given by a system of ordinary differential equations as follows:

$$\begin{aligned} \dot{x} &= \sigma y - \sigma x \\ \dot{y} &= -xz + \rho x - y \\ \dot{z} &= xy - \beta z \end{aligned}$$

The coordinates x, y, and z are related to the velocity of the circulating gas, its temperature gradient and nonlinear deviations from the mean temperature profile [271]. σ is called Prandtl number and it is assumed that $\rho, \sigma > 1$. For a physical interpretation of the parameters, see also ref. [320]. We will consider the parameter values $\sigma = 16.0$, $\beta = 4.0$, $\varrho = 45.92$. The chaotic attractor is well studied for these values (see e.g. ref. [33] and references therein), whereas Lorenz in his original article [29] used different values. The system is dissipative, as one can see when calculating the exponential volume contraction: $\nabla \cdot \mathbf{F} = -(1 + \sigma + \beta) < 0$ for the parameter values chosen [271]. Although the phase space of the Lorenz system is three-dimensional, the chaotic attractor is approximately two-dimensional: The dynamics is almost completely reduced to a rotation in two flat discs around two FPs. These FPs are the centre of the circular motion and are located at $(\pm\sqrt{\beta(\varrho-1)}, \pm\sqrt{\beta(\varrho-1)}, \varrho-1)$. A third stationary point is at $(0,0,0)$. These stationary points of the model system are important for hydrodynamic models, for example in geophysical studies [271]. However, considerable information about the properties of the system can be gained when studying the structure of the POs. Many features of the Lorenz system and especially its POs and their bifurcations are discussed at length in ref. [33].

6.1.2 Implementing the ST approach

Several methods have been applied to detect the unstable POs of the Lorenz system (see ref. [271] and references therein). Going beyond the general theory of the ST method to time-continuous systems we will in the following demonstrate how it can be extended to locate unstable POs in the time-continuous Lorenz system.

We define a PSS by $\{(x, y, z|z = \varrho - 1\}$. This choice is advantageous, since the corresponding surface contains both FPs $(\pm\sqrt{\beta(\varrho-1)}, \pm\sqrt{\beta(\varrho-1)}, \varrho-1)$. Since every unstable PO of the system oscillates about one or both of these FPs, there have to be intersection points on the PSS and as a result FPs of the Poincaré map. These FPs can be detected with the ST method for maps as described in sections 3 and 5.1.

When propagating a set of initial conditions with the different stability transformed systems it often happens that trajectories converge in one of the stationary points. This implies an undesirable slowing down of the numerical investigation. The convergence in the stationary points can be prevented by stopping the propagation of the corresponding trajectory close to these stationary points. By doing this, it is possible that POs close to the stationary points are not found. However, a specific unstable PO has in general several intersections with the PSS, some of which are at larger distance to the stationary points and therefore detectable with the ST method. Let us discuss the choice of the distribution of the initial points. As mentioned above, the chaotic attractor embedding the unstable POs is nearly two dimensional. This results in an almost one-dimensional intersection of the attractor with the PSS. It is therefore not advisable to chose an uniform distribution in the hyper-plane for the set of initial points. Instead, initial points are better sampled from the set of intersection points of a chaotic trajectory with the PSS. It proved to be more efficient not to sample successive iterations of the chaotic trajectory, but to allow for a relatively large transient in time between consecutive initial points. This is due to the intermittent behaviour of the chaotic trajectories in the vicinity of POs.

The parameter λ is closely related to the stability of the unstable POs that can be detected (see section 5.3). It is therefore necessary to adjust its value each time the required number of intersections of the POs with the PSS is changed.

The Poincaré maps discussed in this section are in some respect artificial. Contrary to the generic case of time–discrete maps like the Hénon map and Ikeda map in section

5.2, a topological entropy, which would give an approximate guess on the number of FPs of a given period p, can not be easily defined. Moreover, the number of FPs of period p of the Poincaré map is very sensitive to the position of the PSS in phase space. However, this can be regarded as an advantage: When discussing the Hydrogen atom in a magnetic field in section 6.2, we will see that the freedom in constructing the Poincaré map can be used to selectively detect POs with given symmetry properties.

As discussed above, the numerical efficiency can be significantly improved by combining the ST method with the Newton method. When doing this, it is important at which point of the convergence procedure the turnover between the algorithms takes place. The following strategy turned out to be most efficient: The trajectory is propagated with the stability transformed system, starting from the initial point, until a given step-size $|\mathbf{f}^{(p)}(\mathbf{r}) - \mathbf{r}| < \epsilon_{ST}$ is reached. For the Lorenz system, $\epsilon_{ST} \approx 0.1$ proved to be a suitable value. Now a certain number (typically ≈ 4) iteration steps of the stability transformed system are done in order to see whether the step-size continues to decrease. This step is necessary due to the above–mentioned intermittent dynamics of the transformed system: Trajectories often remain close to unstable (for the actual value of λ) POs, before they a rejected by their repulsive dynamics. This often happens when the parameter λ is still too large to stabilise this particular PO. In this case, the trajectory is still too far away from the PO for the Newton algorithm to converge. Therefore, the propagation of the stability transformed system is continued if the step-size does not decrease successively. A decreasing step-size, however, can be a signature of a stable PO approached by the trajectory. At this point the start of the iteration of the Newton algorithm is useful. It should converge within a relatively small number of iterations (≤ 10) not too far from its starting point. However, it might happen that the convergence pattern is different, e.g. that much more iteration steps are necessary or that the converging trajectory covers a larger distance in phase space. In this case the FPs the Newton trajectory and the stability transformed trajectory converge to are different. If it is desired that the FPs detected have the properties given implicitly by the specific stability transformation (see section 4), the FP found has to be discarded. In this case, the propagation of the stability transformed trajectory is continued. In general and provided λ is sufficiently small, generally ≤ 50 iteration steps of the stability transformed system and ≤ 10 steps

of the Newton algorithm are needed to determine the position of a PO with an accuracy of $|\mathbf{f}(\mathbf{r}) - \mathbf{r}| \leq 10^{-14}$.

6.1.3 Results

In Table 4 the numerical results for the Lorenz system are shown. It is remarkable that all POs are found with just one stability transformed system: $\mathbf{s}_4$ with the matrix $\mathbf{C}_4$. Also shown is the number of primitive POs and their mean period as function of the number of intersections with the PSS. The number of primitive POs agrees with the numbers given in ref. [271]. The mean length of the orbits increases approximately linearly with the number of intersections. This peculiarity is a consequence of the rotating dynamics of the Lorenz system. The trajectories, and with them the POs rotate about the stationary points $(\pm\sqrt{\beta(\varrho-1)}, \pm\sqrt{\beta(\varrho-1)}, \varrho-1)$ with nearly constant frequency. Fig. 13 shows the approximately linear dependency and small variability of the length of the POs with respect to the number of intersections. The last two columns of the diagram show the parametrical properties of the ST approach: The size of λ and the number of initial points necessary to locate the given number of POs. However, one has to keep in mind that not all initial points converge. Therefore, for the actual application, these numbers have to be slightly larger than those given in Table 4.

With the ST method, detection of POs with a remarkable large number of intersection points is possible. Fig. 14 shows an example of a PO with 30 intersection points. The topology of this orbit is representative for most of the other closed orbits: It is dominated by a rotation in two planes with a varying number of transition between them. In Fig. 15 the intersection points in the PSS of all POs up to length $p = 14$ are displayed. Here, too, the nearly two-dimensional structure of the chaotic attractor is obvious. It is possible that the small dimensionality of the attractor is related to the fact that only one stability transformed system is enough to detect the complete set of POs.

6.2 The Hydrogen atom in a homogeneous magnetic field

The set of POs in a chaotic physical system such as the Hydrogen atom in a homogeneous magnetic field form a skeleton of the underlying dynamics. The POs are an important tool when applying semiclassical methods to calculate classical and quantum mechanical

properties of the system [62, 321–323]: Examples for this quantities are the spectrum and the fluctuations of the level density of the corresponding quantum system and even individual quantum mechanical wave functions ("scarring"). The dynamical system of a Hydrogen atom in a homogeneous magnetic field is known in literature as the diamagnetic Kepler problem. Several methods have been developed to locate POs in this system. For example, POs with certain symmetry properties can be detected by propagation of three specific lines in phase space [323]. Some of these methods are based on a symbolic code assigned to the individual PO, and nearly all are especially designed for the diamagnetic Kepler problem. In contrast to the other algorithms mentioned, the ST method requires no pre-knowledge of special properties of the system. Implementing the algorithm requires only a numerical routine to integrate the equations of motion, a clever position of the PSS and a chaotic trajectory to sample the initial points.

6.2.1 Equations of motion

The Hamiltonian for the hydrogen atom in a homogeneous magnetic field directed along the z-axis reads under the assumption of an infinite nuclear mass [62]:

$$H = \frac{p^2}{2} - \frac{1}{|\mathbf{r}|} + \frac{1}{2}\gamma l_z + \frac{1}{8}\gamma^2(x^2 + y^2)$$

It depends on the coordinates $\mathbf{r}$ and $\mathbf{p}$ and on the magnetic field γ. This additional parametric dependence can be removed by scaling the coordinates (e.g. ref. [62])

$$\tilde{\mathbf{r}} = \gamma^{2/3}\mathbf{r} \quad \text{and} \quad \tilde{\mathbf{p}} = \gamma^{-1/3}\mathbf{p}$$

Now the dynamics (i.e. the Hamiltonian equations of motion) depends only on the scaled energy ϵ,

$$\epsilon = \gamma^{-2/3}E$$

and not on E and γ separately.

The singularity at $\tilde{\mathbf{r}} = 0$ is a drawback of the corresponding Hamiltonian. It can be removed e.g. by the introduction of semi–parabolic coordinates and a coordinate dependent scaling of the time [62]:

$$\nu^2 = |\tilde{\mathbf{r}}| - \tilde{z} \quad , \quad \mu^2 = |\tilde{\mathbf{r}}| + \tilde{z}$$

The momenta

$$p_\nu = \frac{d\nu}{d\tau} \quad , \qquad p_\mu = \frac{d\mu}{d\tau}$$

are defined with respect to the scaled time τ given by

$$dt = 2|\tilde{\mathbf{r}}|d\tau = (\nu^2 + \mu^2)d\tau \tag{23}$$

The equations of motion in the transformed system at a fixed value of the scaled energy are equivalent to the equations of motion generated by the Hamiltonian

$$h(\mu, \nu, p_\mu, p_\nu) = \frac{p_\nu^2}{2} + \frac{l_z^2}{2\nu^2} + \frac{p_\mu^2}{2} + \frac{l_z^2}{2\mu^2} - \epsilon(\nu^2 + \mu^2) + \frac{1}{8}\nu^2\mu^2(\nu^2 + \mu^2) \equiv 2 \tag{24}$$

at the fixed pseudo-energy 2. For negative scaled energies $\epsilon < 0$ the Hamiltonian (24) represents a sextic oscillator: Two harmonic oscillators with frequency $\omega = \sqrt{-2\epsilon}$, coupled by the term $\nu^2\mu^2(\nu^2 + \mu^2)$ due to the diamagnetic interaction. The trajectories generated by the Hamiltonian H and h are not related by a canonical transformation, although there is a bijective correspondence between them.

In the following we confine ourselves to vanishing angular momentum $l_z = 0$. The Hydrogen atom in a magnetic field is an example of a system with mixed phase space, and the appearance of the PSS depends significantly on the value of the scaled energy ϵ (see e.g. ref. [62]). For the value $\epsilon = -0.8$ the system is close to integrable. The integrable volume of phase space decreases as ϵ approaches zero, whereas the ergodic trajectories fill an increasingly larger fraction. In our investigations of the system we first considered a value of the scaled energy of $\epsilon = -0.1$. This value of the scaled energy corresponds to an almost completely ergodic phase space. We emphasise however that the ST method works also in case a considerable fraction of the phase space is regular, as we will see when investigating the system with a scaled energy of $\epsilon = -0.4$.

The equations of motion in the semi-parabolic coordinates (μ, ν, p_μ, p_ν) are derived in a straightforward way from the Hamiltonian (24):

$$
\begin{aligned}
\dot{\mu} &= \frac{\partial h}{\partial p_\mu} = p_\mu \\
\dot{\nu} &= \frac{\partial h}{\partial p_\nu} = p_\nu \\
\dot{p_\mu} &= -\frac{\partial h}{\partial \mu} = \epsilon\mu - \frac{1}{4}\mu\nu^4 - \frac{1}{2}\mu^3\nu^2 \\
\dot{p_\nu} &= -\frac{\partial h}{\partial \nu} = \epsilon\nu - \frac{1}{4}\nu\mu^4 - \frac{1}{2}\nu^3\mu^2
\end{aligned}
\tag{25}
$$

All four coordinates are simultaneously integrated using a Taylor–integration algorithm [324]. The dynamics on the energy shell is only three-dimensional.

6.2.2 Numerical Implementation

The Taylor integrator [324] is an extremely powerful tool. Although the chaotic trajectories have a quite complicated topology and form interwoven tangles (see Fig. 17), the integrating routine performs very large time steps. When the Taylor integrator is used for the calculation of successive intersections of a trajectory with the Poincaré surface, one has to take care that the step size of the integration routine does not exceed the length of the expected unstable PO.

When discussing the Lorenz system, we already mentioned that the ST method as extended for time-continuous systems has three key components: A good positioning of the PSS, the tuning of the value of the parameter λ and the proper grid of initial points. We now discuss the meaning and proper choice of these three components for the hydrogen atom:

The PSS is defined as the manifold obeying:

$$\{\nu, p_\nu, \mu = 0\}$$

Due to the exchange symmetry $\mu \leftrightarrow \nu$ of the Hamiltonian Eqn. (24) and the equations of motion (25) this choice of the PSS gives the same numerical values of the spatial position of the unstable POs as the choice $\{\mu, p_\mu, \nu = 0\}$ would yield.

The position of a point in the PSS is therefore given by the pair of coordinates (ν, p_ν). It is determined using a bisection method with an accuracy of $|\mu| < 10^{-15}$. The intersection

of the three-dimensional energy surface with the PSS defines a two-dimensional area in this surface in which the dynamics of the system takes place. Eqn. (24) shows that the area in the PSS allowed to the dynamics is given by ($p_\mu^2 \geq 0$)

$$p_\nu^2 - 2\epsilon\nu^2 \leq 4$$

i.e. in coordinates ($\sqrt{-2\epsilon}\nu, p_\nu$) this area is given by a circle of radius 2. The Hamiltonian Eqn. (24) with $l_z = 0$ and $\mu = 0$ defines the initial value $p_\mu = 2\sqrt{2 - \epsilon\nu^2 - \frac{1}{2}p_\nu^2}$ corresponding to an initial point (ν, p_ν) in the surface of section. It is sufficient to consider just one sign (+ in this case) for the square root on the right hand side. Choosing the other sign (−) simply yields POs that are related by reflection at the PSS to orbits that are found by choosing the positive sign of the square root (inverting the sign of both μ and p_μ does not alter the equations of motions (25)). The Cartesian time between successive sections of a trajectory with the PSS is given by Eqn. (23)

$$t(\tau) = 2\int_0^\tau (\nu^2(\tilde{\tau}) + \mu^2(\tilde{\tau}))\, d\tilde{\tau}$$

It equals the period of the orbit in case the trajectory starts at a FP of the Poincaré map.

The role of the number of intersections of an orbit is slightly modified in comparison with the cases discussed so far: The unstable POs in this system are less regular than those of the Lorenz system. There may be long unstable POs with only a few intersections of the PSS as well as relatively short ones which intersect the Poincaré surface quite often. For the distribution of the length of the unstable POs see Fig. 16. One example of such an orbit is displayed in Fig. 17. Similar long orbits can be located with a small value of λ, a small number of intersection points (i.e. short period p) and a relatively large number of initial points. The biggest bulk of the orbits found applying these conditions, however, are shorter and possess a simpler appearance. The appearance of very long as well as very short POs applying the same parameters within the ST approach suggests a scaling property of this system: In the neighbourhood of each PO with given number of intersections, there seem to be an infinite number of POs with the same number of intersections, but with arbitrary long period. The larger the grid of initial points is and the smaller the parameter λ is, the more POs are expected to be found in a given area of phase space. To investigate this particular issue, we used rather large grids of initial

points to find POs with up to four intersections. As a result we found rather large sets of POs with extensively varying length, as visible in Fig. 16. There is no doubt, that a similar procedure, i.e. propagating the ST method with large grids and a relatively small λ, would display such a "scaling" for POs with a larger number of intersections, as well.

From the above, it is evident that using the ST method, one can – at least in an approximate way – selectively stabilise unstable POs with certain topological features. Looking for POs starting with a large grid of initial points and a comparatively small value for the λ parameter one can detect long POs which linger for a long time at a certain distance above and below the PSS (Fig. 18 a)). The numerical effort of this procedure is bearable, since for each step of the ST algorithm the Poincaré map has to be iterated just a few times. On the other side, looking for FPs of the higher iterated Poincaré map, one might get, even for a relatively large λ, POs that have a crown–like appearance like in Fig. 18 b). *The position of the PSS and the demanded number of intersections can therefore be used as a tool to determine, at least in a rough way, the topology of the POs to be found.*

Determining the set of initial points is relatively straightforward for this system. The dynamics is supposed to be nearly ergodic and conserves phase space volume. Therefore an uniform distribution of initial points on the surface of section is a good choice. The Hamiltonian equations (24) are symmetric with respect to the reflections $\nu \to -\nu$ and $p_\nu \to -p_\nu$. Therefore, each unstable PO with a given length appears four times in phase space, and the intersections with the PSS are located at coordinates related by the above symmetry operations. To avoid the convergence into POs that are trivially related by symmetry, the initial points were distributed in a quarter segment of a circle with the coordinates $(\sqrt{-2\epsilon}\nu, p_\nu)$ and the radius 2.

6.2.3 Ergodic phase space

Table 5 displays the result of the numerical investigations. Differently to the Lorenz system the minimal number of intersections is 1, corresponding to POs of the type as in Fig. 18 a). As already discussed above, the number of prime orbits with a given number of intersections as shown in Table 5 is not unique. Therefore the numbers of POs with a given number of intersections and their mean length of period do not vary in a regular way

as for the Lorenz system, Table 4. The rightmost column in Table 5 shows the minimal number N_i of initial points that had to converge in order to find the listed number of POs. We used a set of 4000 initial points to detect POs with up to 4 intersections. Since this number turned out to be larger than the necessary saturation N_i, we reduced it to 1000 initial points for POs with more than four intersections. However, again one has to keep in mind that not all initial points finally converge in a PO. They might diverge or might not reach the desired accuracy within an appropriate time. Differently to the case of the Lorenz system, propagation of *each* of the ST–transformed systems in the complete minimal set $\{\mathbf{s}_1, \mathbf{s}_3, \mathbf{s}_4\}$ yielded distinct orbits. The set of initial points has to be propagated three times, with a different ST–transformed system each time. Fig. 19 shows the intersection points of the POs given in Table 5 of the system with the Poincaré surface. To generate this figure the intersection points have been mirror–imaged by the $\sqrt{-2\epsilon}\nu$– and p_ν–axes, according to the above-discussed symmetries. The dynamics is supposed to be ergodic and conserves phase-space volume, i.e. a chaotic trajectory fills the intersection of the energy surface and the PSS with uniform density. Nevertheless, the intersections of the POs are arranged in a way that suggests some reminiscent structure of phase space. Especially for larger absolute values of $\sqrt{-2\epsilon}\nu$ a shell-like structure emerges. Given a value of $|\sqrt{-2\epsilon}\nu|$, certain values of $|p_\nu|$ seem to be favoured by POs. With $|\sqrt{-2\epsilon}\nu|$ approaching its maximal value of 2, these favoured values continuously decrease to zero. It is supposed that, taking POs with a higher number of intersections into account, the accessible phase space will be filled up and the Poincaré section will be uniformly covered with intersections of POs.

6.2.4 Mixed phase space

The almost completely chaotic phase space of the Hydrogen atom for the scaled energy $\epsilon = -0.1$ undergoes a transition to an almost completely regular phase space for the scaled energy $\epsilon = -0.8$. For scaled energies between these two extreme values phase space is mixed with a ratio of regular structures between 0 and 1. Still unstable POs are located in the chaotic regions of the phase space. However, with decreasing ϵ more and more chains of alternating elliptic and hyperbolic FPs emerge. These chains are visible as an island structure in phase space. For lowering ϵ they form invariant tori (see e.g. ref. [3]).

These tori cover the whole phase space in the purely regular system. The order of the appearance of these tori (or their destruction, when starting with a completely regular system) is described by the KAM-theorem [325–327]. We are interested in the question whether the ST method is suited to detect POs even in a dynamical system with such a mixed phase space. To this aim, we propagate a grid of 1000 uniformly distributed initial points for a value of the scaled energy of $\epsilon = -0.4$ with all eight stability transformed systems. We chose a value of $\lambda = 0.005$. As mentioned above, in the fully chaotic, ergodic system, all detected POs were located by applying $\mathbf{s}_1$, $\mathbf{s}_3$ and $\mathbf{s}_4$. In contrast, now the propagation of *all* eight stability transformed systems yielded unstable POs. Fig. 20 shows the PSS with the unstable POs of lengths $p = 1...6$ found for this value of λ and the described set of initial points. The arrangement of the elliptic FPs surrounding the destroyed invariant tori is clearly visible. Nearly all FPs found are related to these elliptic FPs, whereas in the purely chaotic regime of the phase space only a few POs have been detected. However, with a smaller value of λ, certainly more closed orbits can be located in these regions, too.

6.3 Classical collinear Helium with and without laser field

First investigations of the classical Helium atom have been performed in connection with the old quantum theory [328–331]. Attempts were made to transfer the early method of quantisation of the hydrogen atom and to pay special attention to the POs of the classical system. However, the success of quantum mechanics in the following decades made these studies seem unnecessary. In addition, the non-integrability of the classical dynamics of the helium atom did not allow for an easy quantisation [332]. Modern semiclassical methods developed in the last twenty years [63, 333–336] brought the classical (highly excited) helium atom again into the focus of interest [337–345]. The semiclassical properties of the helium atom have consequently been studied extensively [322, 346]. We apply the ST method to detect POs of the classical helium atom in the collinear configuration. With this geometry, the nucleus and the two electrons are arranged on a line. The electrons cannot penetrate the nucleus. Therefore, two topologically different configurations are possible: With the Zee-configuration, both electrons are on the same side of the nucleus. If the nucleus is in between the two electrons, the configuration is called eZe. The clas-

sical and quantum dynamics of the driven Zee-configuration (the so-called 'frozen-planet configuration") has already been analysed in great detail [347–352]. In the following, we will investigate the eZe-configuration with and without an oscillating electric field with respect to periodic structures in phase space.

6.3.1 The equations of motion of the classical helium atom

The non-relativistic Hamiltonian of the helium atom for fixed infinitely heavy nucleus is given by (in atomic units)

$$H(\mathbf{r}_1, \mathbf{r}_2, \mathbf{p}_1, \mathbf{p}_2, t) = \frac{\mathbf{p}_1^2}{2} + \frac{\mathbf{p}_2^2}{2} - \frac{Z}{|\mathbf{r}_1|} - \frac{Z}{|\mathbf{r}_2|} + \frac{1}{|\mathbf{r}_1 - \mathbf{r}_2|} + (\mathbf{r}_1 + \mathbf{r}_2)\mathbf{F}(t) \tag{26}$$

The spatial coordinates with respect to the nucleus and the momenta of the two electrons are $\mathbf{r}_1$, $\mathbf{r}_2$ and $\mathbf{p}_1$, $\mathbf{p}_2$, respectively. The external field with amplitude $|\mathbf{F}|$ and frequency ω is given as

$$\mathbf{F}(t) = |\mathbf{F}| \cos(\omega t)\, \mathbf{e}_z$$

The phase space of this system is twelve-dimensional.

The Hamiltonian Eqn. (26) possesses a remarkable scaling property [353, 354]: The corresponding equations of motion are invariant under the following scaling operations with a positive parameter $\lambda > 0$

$$\begin{aligned}
\mathbf{r}_i &\longmapsto \lambda \mathbf{r}_i \qquad (i = 1, 2) \\
\mathbf{p}_i &\longmapsto \lambda^{-1/2} \mathbf{p}_i \qquad (i = 1, 2) \\
t &\longmapsto \lambda^{3/2} t \\
\mathbf{F} &\longmapsto \lambda^{-2} \mathbf{F} \\
\omega &\longmapsto \lambda^{-3/2} \omega \\
H &\longmapsto \lambda^{-1} H
\end{aligned} \tag{27}$$

It is therefore advisable to fix the value of λ when investigating the dynamics. This can be done by assigning an initial value of either a time dependent variable (e.g. the energy) or by fixing the value of a time independent parameter (e.g. the frequency ω).

The equations of motion belonging to Eqn. (26) are not suited for a numerical integration: In a two-body collision, which is very frequent in the linear configuration, one

of the electrons approaches the nucleus, which results in an increase of its momentum proportional to $|\mathbf{r}_i|$ and finally to divergence. This problem can be fixed with help of the so-called Kustaanheimo-Stiefel transformation [355, 356]. This transformation maps the three-dimensional, canonically conjugated vectors $\mathbf{r}$ and $\mathbf{p}$ onto the four-dimensional and equally canonically conjugated vectors P and Q, respectively.

$$\begin{pmatrix} \mathbf{r} = (r_x, r_y, r_z)^T \\ \mathbf{p} = (p_x, p_y, p_z)^T \end{pmatrix} \longmapsto \begin{pmatrix} \mathbf{Q} = (Q_a, Q_b, Q_c, Q_d)^T \\ \mathbf{P} = (P_a, P_b, P_c, P_d)^T \end{pmatrix} \tag{28}$$

For details of this quite subtle transformation we refer the reader to refs. [355, 356]. Additionally, we introduce a new time τ and a new Hamiltonian function $\mathcal{H}$ according to

$$\begin{aligned} \mathrm{d}t &= R_1 R_2 \mathrm{d}\tau \\ \mathcal{H} &= R_1 R_2 (H - E) \end{aligned}$$

with H being the Hamiltonian function in the new coordinates $\mathbf{Q}$ and $\mathbf{P}$, E being its value at a specific point of time t and $R_i = \mathbf{Q}_i^2$, $i = 1, 2$. $\mathcal{H}$ vanishes for any time τ and therefore describes an autonomous system – contrary to the system given in Eqn. (26).

It is an interesting fact that now E and τ are additional, canonically conjugated variables of the system. Their time evolution is given by

$$\frac{\mathrm{d}t}{\mathrm{d}\tau} = -\frac{\partial \mathcal{H}}{\partial E} \quad , \qquad \frac{\mathrm{d}E}{\mathrm{d}\tau} = \frac{\partial \mathcal{H}}{\partial t}$$

Starting from the original Hamiltonian H (26), we end up with the new Hamiltonian

$$\begin{aligned} \mathcal{H} &= \mathcal{H}(\mathbf{Q}_1, \mathbf{Q}_2, \mathbf{P}_1, \mathbf{P}_2, E, t) \\ &= \frac{1}{8} R_2 \mathbf{P}_1^2 + \frac{1}{8} R_1 \mathbf{P}_2^2 - (R_1 + R_2) Z + \frac{R_1 R_2}{|\mathbf{f}(\mathbf{Q}_1) - \mathbf{f}(\mathbf{Q}_2)|} \\ &\quad + R_1 R_2 (\mathbf{f}(\mathbf{Q}_1) + \mathbf{f}(\mathbf{Q}_2)) \cdot \mathbf{F}(t) - R_1 R_2 E \end{aligned}$$

and the new equations of motion

$$
\begin{aligned}
\frac{\mathrm{d}t}{\mathrm{d}\tau} &= R_1 R_2 \\
\frac{\mathrm{d}E}{\mathrm{d}\tau} &= R_1 R_2 (\mathbf{f}(\mathbf{Q}_1) + \mathbf{f}(\mathbf{Q}_2)) \cdot \frac{\mathrm{d}\mathbf{F}}{\mathrm{d}t}(t) \\
\frac{\mathrm{d}\mathbf{Q}_1}{\mathrm{d}\tau} &= \frac{1}{4} R_2 \mathbf{P}_1 \\
\frac{\mathrm{d}\mathbf{Q}_2}{\mathrm{d}\tau} &= \frac{1}{4} R_1 \mathbf{P}_2 \\
\frac{\mathrm{d}\mathbf{P}_1}{\mathrm{d}\tau} &= R_1 R_2 \sum_{j=x,y,z} \left(\frac{f_j(\mathbf{Q}_1) - f_j(\mathbf{Q}_2)}{R_{12}^3} - F_j(t) \right) \frac{\partial f_j}{\partial \mathbf{Q}_1} \\
&\quad + 2\mathbf{Q}_1 \left(-\frac{1}{8}\mathbf{P}_2^2 + Z - \frac{R_2}{R_{12}} - R_2 (\mathbf{f}(\mathbf{Q}_1) + \mathbf{f}(\mathbf{Q}_2)) \cdot \mathbf{F}(t) + R_2 E \right) \\
\frac{\mathrm{d}\mathbf{P}_2}{\mathrm{d}\tau} &= R_1 R_2 \sum_{j=x,y,z} \left(\frac{f_j(\mathbf{Q}_2) - f_j(\mathbf{Q}_1)}{R_{12}^3} - F_j(t) \right) \frac{\partial f_j}{\partial \mathbf{Q}_2} \\
&\quad + 2\mathbf{Q}_2 \left(-\frac{1}{8}\mathbf{P}_1^2 + Z - \frac{R_1}{R_{12}} - R_1 (\mathbf{f}(\mathbf{Q}_1) + \mathbf{f}(\mathbf{Q}_2)) \cdot \mathbf{F}(t) + R_1 E \right)
\end{aligned}
\tag{29}
$$

with $\mathbf{f}(\mathbf{Q}) = (f_x(\mathbf{Q}), f_y(\mathbf{Q}), f_z(\mathbf{Q}))^T$, the components given by

$$
\begin{aligned}
f_x(\mathbf{Q}) &= Q_a^2 - Q_b^2 - Q_c^2 + Q_d^2 \\
f_y(\mathbf{Q}) &= 2(Q_a Q_b - Q_c Q_d) \\
f_z(\mathbf{Q}) &= 2(Q_a Q_c + Q_b Q_d)
\end{aligned}
$$

and $R_{12} = |\mathbf{f}(\mathbf{Q}_1) - \mathbf{f}(\mathbf{Q}_2)|$. The equations of motion (29) are regular in $|\mathbf{r}_1| = 0$ and $|\mathbf{r}_2| = 0$ (see e.g. ref. [347]). Therefore two-body collisions of an electron and the nucleus do not cause any problems for the numerical integration. Instabilities arise only for the collision of both electrons ($|\mathbf{r}_1| = |\mathbf{r}_2| = 0$). Due to conservation of energy, these collisions can take place only at the nucleus. Three-body collisions of this kind can principally not be regularised [357]. However, they are of minor importance for the numerical calculations. In the following, we focus on the POs of the helium atom in collinear (one-dimensional) eZe-configuration.

6.3.2 Coding and generic periodic orbits without external field

The number of POs of a chaotic system generally increases exponentially with the length of the orbits. This is why a complete detection of all POs up to a given length, necessary for the semiclassical quantisation of a system, is difficult. A helpful signature for the completeness of a set of POs is the symbolic code, that provides a one-to-one relation between the POs and binary strings of finite length. The electrons of the collinear helium atom collide with the nucleus in a certain sequence. For each individual PO, the sequence of these collisions is unique. Therefore the symbol sequence like $''...i_{-2}, i_{-1}, i_0, i_1, i_2, ...''$ can be used to label a particular PO. Using the symbol 1 and 2 for collisions of the first and second electron, respectively, a sequence with periodic pattern like $''...112112112...''$ is assigned to a PO. Some POs show a reversal of the roles of the two electrons after half of the period: The trajectory of the second electron in the second half of the period is the mirror image of the trajectory of the first electron in the first period and vice versa. This is a redundancy of the symbolic coding as described above. In these cases, the qualitatively unique symbol sequence is only half of the period. In a reduced symbolic coding, the binary collision of a electron is labelled with $''+''$ or $''-''$, when the preceding collision concerned the same or the other electron, respectively. The symbol sequence $''...122122...''$ in the $''12''$-code therefore corresponds to the sequence $''...-+--+...''$ in the $''+-''$-code. The length of a symbol sequence in the $''+-''$-code equals the length of the sequence in the $''12''$-code described previously, as long as no reversal of roles takes place, in which case the length is halved. The reduction of the code corresponds to a de-symmetrisation of the motion, which is described in a fundamental region of the symmetry-reduced configuration space. The lengths of the sequences of POs, which are not symmetric with respect to an exchange of the two electrons, are not altered. In Table 6 all POs up to the length $p = 7$ of the collinear helium atom and their symbolic sequences in the $''12''$- and the $''+-''$-code are listed. They are unique except for cyclic permutations. The number of primitive POs in systems with a symbolic code of this kind increases like $2^N/N$ with the length N of the sequence. The orbit with the symbolic code $''+''$ is in some respects exceptional: It describes a trajectory with one electron at infinite distance to the nucleus while the other one oscillates with a high frequency close to the nucleus. Strictly speaking, this is not a bound periodic configuration of the system. In

the fifth column of Table 6 the Lyapunov exponent of the various periodic orbits is given. The stability of a PO is strongly determined by whether or not the two electrons and the nucleus come close to a three-body-collision ($r_1 = r_2 = 0$) within one period. In this context the POs with just one letter $''-''$ in the string of the symbolic code are remarkable. Fig. (21) shows some examples of these orbits, e.g the orbit with the code $''+++-''$. This is a PO which is symmetric with respect to the reversal of the roles of the two electrons as described above. Obviously, this reversal of roles requires a large momentum transfer at the symmetry point in time. To this aim, both electrons have to be close to each other, i.e. they approach a three-body-collision. The more $''+''$-letter precede a $''-''$-letter in the symbolic code, the closer the trajectory comes to a three-body-collision. The Lyapunov exponent increases in a corresponding way. Another extreme species of PO is given by a symbolic code of the type $''+(-)^N''$, N being an integer number. Within this configuration, both electrons oscillate with nearly the same frequencies. The phase difference increases until one electron touches the nucleus two times within one period of the other electron, which results in the appearance of a $''+''$-letter in the symbolic code. Another type of PO has a symbolic code of the form $''(+)^N--''$. As can be seen in the example with $N = 24$ in Fig. (21), one electron oscillates close to the nucleus, whereas the second one stays for a long time far away from it. This class of POs belong to the least unstable and therefore possesses the smallest Lyapunov-exponent compared to orbits with the same length of the symbolic code.

6.3.3 Detection of periodic orbits

In the following section we describe the approach for localising POs of the collinear helium atom by applying the ST method. Similar to the time-continuous dynamical systems of the Lorenz system and the hydrogen atom in the homogeneous magnetic field, we are now searching for POs as FPs of a suitably defined Poincaré-map. Appropriately placed initial points are then propagated with the ST-transformed Poincaré-map. As they are of central importance, we again emphasise the basic four characteristics of the ST-method that determine the results of the numerical calculations:

- the position of the *Poincaré surface of section*
- the set of *initial points*

- the size of the *parameter* λ
- the *matrices* used in the ST method

As PSS a stroboscopic map with equidistant time intervals ω^{-1} is introduced. The reason for this is the periodic time dependence of the equations of motion of the system with an external field, since the Hamiltonian of the collinear helium atom in an oscillating field is explicitly time dependent (see section 6.3.1). A PSS defined as a hyper-manifold in the four-dimensional phase space as it is done for the other systems studied in this context is not advisable: It is true that every PO intersects the surface defined in this way in a controlled way. However, to fully specify a PO one has to know not only the position in phase space, but also the frequency and the phase of the driving electric field. This can be avoided by introducing the time i.e. the phase $\omega t \bmod 2\pi$ of the field as an additional dimension, as explained in section 6.3.1. The Hamiltonian is time independent in this extended phase space. The PSS is defined as a cut in the time as an auxiliary dimension of the phase space. The scaling properties Eqn. (27) allow to chose the frequency as $\omega = 1$. This determines the value of the scaling parameter λ in Eqn. (27). This too is very useful when analysing data from different numerical calculations: Topologically identical orbits are now mapped onto each other by a simple shift in time. An additional scaling with λ according to Eqn. (27), which implies a change of the length of the orbit, is impossible. This definition of the PSS rather demands the PO or a multiple of it to fit into the time interval $(\Delta t)_{\text{Poincaré}} = \omega^{-1}$ between successive Poincaré sections. A different choice of ω would result in POs topologically equivalent to those for $\omega = 1$, but with spatial and momentum coordinates scaled according to Eqn. (27). This definition of the Poincaré section implies a four-dimensional Poincaré map.

The distribution of initial points for the propagation of the transformed systems is uniform in the four-dimensional phase space. The energetically allowed subspace is determined by the energy in the individual initial points (r_1, r_2, p_1, p_2). It is useful to allow only initial points with an energy E_0 already in the range of the energy of the expected POs. It proved to be favourable to demand the condition $-5 < E_0 < 0$ (in atomic units). Trajectories starting from initial points with energies significantly outside this interval generally diverge quickly. In some numerical investigations the asymmetric-stretch-orbit was looked for. To this aim a specific distribution of initial points is chosen, which already

has the desired antisymmetry: $(r_1 = r_2; p_1 = -p_2)$. In this case a distribution of the initial points in a two dimensional subspace of the four-dimensional phase space is sufficient. However, it turns out that the trajectories of the ST-transformed systems converge after a, in general relatively long, transient time in POs far from the initial point. Therefore a specific location of the initial points in phase space seems generally not necessary.

The value of the parameter λ of the transformation Eqn. (5) determines the properties of the POs that can be found with it. A value of $\lambda = 10^{-2}$ allows the detection of a number of qualitatively different orbits, but for localisation of the particularly unstable orbits with a symbolic code like $''++-''$ and $''+++-''$, a value of $\lambda < 10^{-4}$ is necessary. The time for convergence, however, scales approximately with the inverse step size of the algorithm, λ. The fraction of POs that can be detected is therefore mostly determined by the computational resources available.

The POs are FPs of the discrete four-dimensional Poincaré map. Therefore the four-dimensional $\mathbf{C}_i$-matrices have to be used with the numerical implementation. For this dimension and in contrast to $N = 2$ and $N = 3$ dimensions no minimal set has yet been determined. This is why all $2^4\ 4! = 384$ transformed systems have to be propagated. Generally, in each of the transformed systems several POs are found. With these data, a set of 14 $\mathbf{C}_i$-matrices could be selected empirically that enabled the stabilisation of all

POs:

$$\begin{pmatrix} \cdot & + & \cdot & \cdot \\ + & \cdot & \cdot & \cdot \\ \cdot & \cdot & + & \cdot \\ \cdot & \cdot & \cdot & + \end{pmatrix}, \begin{pmatrix} \cdot & \cdot & \cdot & + \\ \cdot & + & \cdot & \cdot \\ \cdot & \cdot & + & \cdot \\ + & \cdot & \cdot & \cdot \end{pmatrix}, \begin{pmatrix} + & \cdot & \cdot & \cdot \\ \cdot & \cdot & + & \cdot \\ \cdot & - & \cdot & \cdot \\ \cdot & \cdot & \cdot & + \end{pmatrix}, \begin{pmatrix} \cdot & - & \cdot & \cdot \\ \cdot & \cdot & + & \cdot \\ \cdot & \cdot & \cdot & - \\ - & \cdot & \cdot & \cdot \end{pmatrix},$$

$$\begin{pmatrix} + & \cdot & \cdot & \cdot \\ \cdot & \cdot & + & \cdot \\ \cdot & + & \cdot & \cdot \\ \cdot & \cdot & \cdot & + \end{pmatrix}, \begin{pmatrix} \cdot & - & \cdot & \cdot \\ \cdot & \cdot & + & \cdot \\ + & \cdot & \cdot & \cdot \\ \cdot & \cdot & \cdot & + \end{pmatrix}, \begin{pmatrix} + & \cdot & \cdot & \cdot \\ \cdot & - & \cdot & \cdot \\ \cdot & \cdot & - & \cdot \\ \cdot & \cdot & \cdot & + \end{pmatrix}, \begin{pmatrix} + & \cdot & \cdot & \cdot \\ \cdot & \cdot & + & \cdot \\ \cdot & \cdot & \cdot & - \\ \cdot & - & \cdot & \cdot \end{pmatrix},$$

$$\begin{pmatrix} \cdot & + & \cdot & \cdot \\ \cdot & \cdot & + & \cdot \\ - & \cdot & \cdot & \cdot \\ \cdot & \cdot & \cdot & + \end{pmatrix}, \begin{pmatrix} \cdot & + & \cdot & \cdot \\ \cdot & \cdot & + & \cdot \\ + & \cdot & \cdot & \cdot \\ \cdot & \cdot & \cdot & + \end{pmatrix}, \begin{pmatrix} - & \cdot & \cdot & \cdot \\ \cdot & - & \cdot & \cdot \\ \cdot & \cdot & \cdot & - \\ \cdot & \cdot & + & \cdot \end{pmatrix},$$

with $''\cdot'' \equiv 0$, $''+'' \equiv +1$, and $''-'' \equiv -1$. This selection is, however, not generally applicable and specific to the system considered.

In order to enhance the speed of convergence, the combination of the ST approach with the Newton methods is favourable. The subtle issue with the combination of these two algorithms is the point of switching from one to the other. For the system of the collinear helium atom, the switching takes place when reaching a given step size of the ST algorithm. Reaching a value of 10^{-2} of the step size seemed to be a good criterion. It is necessary to control not only the complete convergence of the Newton method, but also whether or not it converges close to the switching point. Typically, a few hundred iterations of the ST algorithm, followed by ten to hundred steps of the Newton algorithm are sufficient to determine the position of a generic PO with an accuracy of 10^{-10} . Combining the ST method with the Newton method, the numerical effort for the detection of a periodic orbit can be reduced by approximately a factor of ten.

In order to apply the Newton method, the monodromy matrix close to a FP $\mathbf{r}_0$ is determined approximately: A set of points shifted away from the trajectory $\mathbf{r}$ by small vectors $\boldsymbol{\epsilon}_i$, $i = 1, ..., 4$ in the different directions of phase space coordinates are

mapped by the Poincaré map $\mathbf{f}(\mathbf{r})$. The individual columns $\mathbf{m}_i$ of the monodromy matrix $\mathbf{M} = (\mathbf{m}_1, \mathbf{m}_2, \mathbf{m}_3, \mathbf{m}_4)$ are then given by $\mathbf{m}_i = (\mathbf{f}(\mathbf{r} + \boldsymbol{\epsilon}_i) - \mathbf{f}(\mathbf{r}))/|\boldsymbol{\epsilon}_i|$. The choice of a stroboscopic Poincaré map has the advantage that the two eigenvectors with eigenvalue one, generic for time-continuous Hamiltonian systems (see section 6), present no obstacles in the numerical performance of the Newton algorithm. The explicit definition of the PSS as a time slice impedes a deviation of the trajectory from the PSS. However, if it is important not to leave the energy shell when propagating the Newton algorithm, some adjustments have to be done in order to ensure the conservation of energy in each iteration of the algorithm as an additional condition (see ref. [43]). But as explained above, the algorithm of the ST method already allows free diffusion in the phase space without being restricted to an energy shell. This diffusion is even desirable, since it allows the access to a large class of periodic orbits for a given set of initial points. This is why we do not implement an additional condition for the conservation of the energy when using the Newton algorithm.

6.3.4 Periodic orbits with and without external field

For investigation of the system of the collinear helium without an external electric field the field amplitude in Eqn. (26) is set $|\mathbf{F}(t)| = 0$. The value of the frequency $\omega = 1$, however, is kept, since it specifies the stroboscopic PSS. With the energy-specific selection of initial points as described above and a parameter of $\lambda = 10^{-4}$, about $50 - -70\%$ of the initial points converge in each individual ST-transformed system. The 25000 detected POs reduce to 64 topologically distinct ones, their symbolic code being up to 26 letters long. The complete set of POs with length up to $p = 7$ of the symbolic $''12''$-code, as listed in Table 6, can be detected. The significant longer orbits generally have a symbolic code according to the scheme $''(+)^N - -''$. Fig. 21 shows a typical example of an orbit in this class. Unstable POs of this kind are remarkably stable.

Introducing an electric, harmonically oscillating field $|\mathbf{F}(t)| \neq 0$ quite a few properties of the POs of the collinear classical helium atom change. The Hamiltonian function is time dependent, therefore the energy is not conserved any more. Moreover the chaotic dynamics can not be described by a complete symbolic code. It is still possible to assign a code constituted from the letters of a binary alphabet to each of the POs in the same

way as it is done for the field free case. However, this code is not unique any more. In general, several POs can be assigned the same code, whereas for other symbolic strings no PO exists. The ST method is successfully applied to locate the positions of the POs in the system with nonzero field, too. The numerical implementation does not differ at all from the corresponding one for the zero field system. The only adjustments to be done concern of course the integration routine. However, when analysing the data, a different strategy has to be followed. The distinction between topologically equivalent and distinct orbits can not be done with help of the symbolic code any more, since the external driving breaks the translational invariance in time of the POs. Now the phase of the oscillations of the electrons with respect to the oscillating field can have several (generally two) distinct values. This fixes the phase of the PO relative to the PSS. As a consequence, the POs in an electric field are determined uniquely by their initial conditions, i.e. the values of spatial coordinates and momenta on the PSS. This feature proves to be very useful when considering whether two POs, given by their coordinates in the PSS, are topologically identical or not.

Now the following question is interesting: How do the POs for the zero field evolve with a slow increase of the field amplitude? Their structure can alter qualitatively at bifurcation points, e.g. at a merging point of two different orbits or when a new orbit arises. Besides this, the stability properties of orbits may change with the field strength. Figs. 22 to 25 show the evolution of several POs with increasing amplitude of the external field. The slow increase of the field amplitude is realized in 100 to 300 equidistant steps, ranging from zero to the maximal amplitude. The new position of the POs is determined after each step of the increase of the field amplitude. To do this, the same Newton routine as for the zero field case is applied. The correct phase of the field is of essential importance (although it is irrelevant for the field free case). There seems to be no rule how to choose the phase difference generally, but it is promising to fix the phase in a way that the temporal evolution of the PO corresponds to the time dependence of the electric field. In case of the existence of a symmetry point of time t_s of the PO with $(r_1(t_s+\tau), r_2(t_s+\tau)) = (r_1(t_s-\tau), r_2(t_s-\tau))$, the field has an extremal amplitude at t_s. At a point of antisymmetry t_a of the PO with $(r_1(t_a+\tau), r_2(t_a+\tau)) = (r_2(t_a-\tau), r_1(t_a-\tau))$, the field strength has a zero at t_a. With this adaption many POs can be traced starting

from the field free case. Only for the most unstable orbits with the symbolic $''+-''$-code $''(+)^N-''$ in the field free configuration a more careful procedure is necessary. These orbits are very close to a three body collision, which results in a large Lyapunov exponent. This has the consequence that the trajectory of the Newton algorithm quickly leaves the basin of attraction of the individual POs even for small field strength. In this case the damped-Newton method [272] proves to be more robust. In this method, each step of the Newton method is scaled with a factor $\rho < 1$. Now more steps are necessary for convergence, but the convergence process is more reliable. A value of $\rho \approx 0.1$ is sufficiently small for the detection of periodic orbits of this type and for tracing them for a strength of the external field up to $F \approx 10^{-2}$.

The Figs. 22 through 25 show four examples for field free POs (including the asymmetric-stretch orbit) and their continuation for non-vanishing field. In the following, we will explain the essential phenomena of the externally driven system with help of these orbits. Both trajectories, corresponding to the two possible values of the phase are displayed in Figs. 22 to 25. The right hand diagram in each of the figures demonstrates the dependence of the Lyapunov exponent on the field strength.

The PO in Fig. 22 is the asymmetric-stretch-orbit, having a point of antisymmetry at time t_a. Therefore the phase is fixed in a way that the amplitude has a zero for the time when the two electrons possess equal distance to the nucleus. For the field in the asymmetrical mode to have a zero at t_a, the phase of the field has to be $\phi = 1/4$ or $\phi = 3/4$.

With a phase of $\phi = 3/4$, the Lyapunov exponent decreases for small field amplitudes, even takes on negative values and has a minimum at approximately $F = 0.9$. *The PO is stable for this field strength.* The dynamics is dominated by regular islands around the PO. Let us discuss the dynamical features underlying this stabilisation process: Trajectories of slightly higher energy than the undisturbed asymmetric-stretch orbit have longer periods, whereas the periods of the orbits of lower energy are shorter. A disturbance of the original PO implies a disequilibrium with respect to the energies of the two electrons. Without external field, the electron with higher energy is delayed. It obtains a positive energy transfer within the following collisions, causing a further acceleration which results in subsequent ionisation of the atom. The external field has the effect to slow down the

faster, longer trajectory (of higher energy) and to accelerate the slower, shorter trajectory (of lower energy). Thus the destabilising process described above is compensated and a stabilisation of the system is achieved. Further increase of the field strength, however, destabilises the PO again. For further details of this process and its quantum mechanical implications, see ref. [358].

A choice of $\phi = 1/4$ results in an impression of the oscillating trajectories of both electrons in their outer extremal positions. The Lyapunov exponent for this mode increases monotonously. In this case, the external field has a destabilising effect: Its orientation causes longer trajectories to gain more energy and to become even longer, whereas shorter trajectories are slowed down and lose energy.

Let us discuss the other examples of POs, shown in Figs. 23 to 25. Although these orbits are qualitatively different to the asymmetric-stretch orbit since they are symmetric with respect to time inversion, essentially the same process is met. In case the external field is directed in a way that the force applied to the electron with the longest trajectory is directed inwards, the instability is reduced. Therefore the Lyapunov exponent decreases for a certain range of the field strength, but, different to the antisymmetric mode, it remains positive and the PO stays unstable.

The minimum of the Lyapunov exponent as a function of the field strength can be sharp (as in the case of the asymmetric-stretch-orbit) or broad. Obviously the position of the minimum of the Lyapunov exponent moves to higher field strengths with increasing length of the symbolic code of the orbit. This feature can be understood qualitatively considering the fact that a long symbolic code generally implies that one of the electrons oscillates relatively close to the nucleus and is tightly bound. To modify this constellation in order to influence the Lyapunov exponent significantly, a relatively strong field has to interact with the tightly bound electron. The increase of the Lyapunov exponent is nearly linear with the field strength, as can be seen for the POs with a longer symbolic code in Figs. 24 and 25.

7 Markov partitions

7.1 Partitions of phase space

A very interesting question in the context of chaotic dynamical systems is the following: How does the dynamical system map the points in the different regions of its phase space and how can the various possible trajectories be characterised? What is the long term behaviour of these trajectories and of the whole system?

These questions concern both the qualitative and overall behaviour of the system. The latter are best understood in terms of the symbolic dynamics which is characteristic for the corresponding system studied. Understanding the symbolic dynamics is in many cases the key to a theory of the specific chaotic system. But how do we derive the symbolic dynamics related to a system?

To characterise mapping properties of areas of phase space, we divide it into non-overlapping regions $\mathcal{M}_1, \mathcal{M}_2, ..., \mathcal{M}_N$ covering the complete accessible phase space. Every subdivision of this kind defines a partition. In particular, if any point in a specific region $\mathcal{M}_j$ of the partition is the image of a point of only one particular region $\mathcal{M}_i$, the partition is called Markov partition (e.g. see refs. [12, 14, 22]). In different words, the regions of a Markov partition are mapped onto other complete regions or onto unions of those. More formally, an expanding d-dimensional map

$$f \;:\; \mathcal{M} \longrightarrow \mathcal{M}$$

is said to generate a finite Markov partition when $\mathcal{M}$ can be divided into N regions $\{\mathcal{M}_1, \mathcal{M}_2, ..., \mathcal{M}_N\}$ such that in a step of the iteration the images of all points in $\mathcal{M}_i$ either fill another region $\mathcal{M}_j$ or avoid it completely:

$$\mathcal{M}_j \cap f(\mathcal{M}_i) = \emptyset \quad \text{or} \quad \mathcal{M}_j \subset f(\mathcal{M}_i) \quad \text{for all } j$$

A Markov partition is therefore a dynamically invariant partition of the phase space. This suggests its use for the qualitative description of trajectories: Each of the regions of the partition is assigned a symbol of a N-letter alphabet. Any trajectory of the system can be assigned a chain of letters of the alphabet, corresponding to the regions of the partition the trajectory passes through.

In addition, Markov partitions are related to the invariant density, an important quantity of the system [359]. In case it is ergodic, the time average of any dynamical quantity can be determined once the invariant density of the system is known (see also refs. [360–362] and refs. [363–366] for the relation of the invariant density to unstable POs). The invariant density of the system is generally given by the eigenfunction with the largest eigenvalue of the Frobenius-Perron operator that governs the time evolution of the system. In case of the existence of a Markovian partition, the operator reduces to a finite-dimensional topological transition matrix. Its dimension corresponds to the fineness of the partition. In this discretised form, the determination of the eigenfunctions is quite straightforward.

One can even try to approximate the invariant density of a given system that possesses no Markov partition. A method known as Ulam's Method provides a general procedure for this approximation and is based on the fact that the maps with a Markov partition are dense in function space. The method was first conjectured by Ulam [367] and was proven later by Li [368]. See ref. [77] for a detailed discussion of this topic.

There is yet another, also very important use of Markov partitions of one-dimensional maps in connection with systems modelling deterministic diffusion [151–153]. In these systems, diffusion is modelled by chains of chaotic maps,

$$r_{i+1} = [r_i] + f_a(r_i)$$

with $[r_i]$ being the largest integer smaller than r_i and $f_a(r_i + 1) = f_a(r_i)$ being a periodic nonlinear function with parameter a. Depending on the value of a, a point $r_i \in ([r_i], [r_i] + 1)$ is mapped back into the unit interval $([r_i], [r_i] + 1)$ or into one of the neighbouring unit intervals. This hopping between intervals models the evolution of the diffusion process. The process is described with help of a diffusion coefficient D, which is a central physical quantity of the system. There are at least three ways to determine D: The first one makes use of the Einstein formula for the diffusion coefficient [369], $D = \lim_{t\to\infty} \frac{<r^2>}{2t}$ with $r(t)$ being the trajectory of the system. Here, the spatial mean $< r^2 >$ can be evaluated with the invariant density derived from the Markov map as described above. The second way to calculate D is via determination of the second largest eigenvalue of the Frobenius-Perron operator (see e.g. refs. [370–372]). A third way is the evaluation of the so-called Green-Kubo formula for diffusion by iterated functional equations [373]. All three methods rely

on the finite dimensionality of the topological transition matrix of the Markov maps.

7.2 Markov partitions as a fixed point problem

We now make use of the ST method to calculate Markov partitions of one-dimensional parametric maps. To demonstrate the essential features of this approach, we concentrate on one-parametric maps

$$r_{n+1} = f_a(r_n)$$

with two extrema (one maximum, one minimum). The calculation of the partition can be related to the search for roots in the parameter space a of the map. The two maps we study are maps of the unit interval (real closed interval of length one) onto itself. Both maps – without the calculation of the modulo — are used to perform one-dimensional model simulations of deterministic diffusion of nonlinear systems as described above [156–158].

- The first map

$$f_a = \begin{cases} \mod\left(a\ \left(r+\frac{1}{2}\right)+\frac{1}{2}, 1\right)-\frac{1}{2}; & r \le 0 \\ -\mod\left(a\ \left(\frac{1}{2}-r\right)-\frac{1}{2}, 1\right)+\frac{1}{2}; & r > 0 \end{cases} \tag{30}$$

  maps the interval $[-\frac{1}{2}, \frac{1}{2}]$ linearly onto itself. It has the symmetry $f_a(r) = -f_a(-r)$ and is discontinuous at $r = 0$. Both extrema are located at $r = 0$ and they have the values

$$\epsilon_1 = \lim_{r\to 0-} f_a(r) = \mod\left(\left(\frac{a+1}{2}\right), 1\right) - \frac{1}{2} \quad , \qquad \epsilon_2 = \lim_{r\to 0+} f_a(r) = \frac{1}{2} - \left|\epsilon_1 + \frac{1}{2}\right|$$

- The second map is given by the sinusoidal map, which is defined as follows:

$$r_{n+1} = f_a(r_n) = \mod\left(r_n + a\cdot\sin(2\pi\, r_n), 1\right) \tag{31}$$

  The extrema of this map are at $r_1 = \frac{1}{2\pi}\arccos(\frac{-1}{2\pi a})$ and $r_2 = 1 - r_1$, respectively, with the values of the function in these points being

$$\begin{aligned} \epsilon_1 = f_a(r_1) &= \frac{1}{2\pi}\arccos\left(\frac{-1}{2\pi a}\right) + a\ \sin\left(\arccos\left(\frac{-1}{2\pi a}\right)\right) \\ &= \frac{1}{2\pi}\arccos\left(\frac{1}{2\pi a}\right) + a\sqrt{1-\left(\frac{1}{2\pi a}\right)^2} \\ \epsilon_2 = f_a(r_2) &= 1 - |1 - r_1| \end{aligned} \tag{32}$$

In addition, the two maps possess trivial FPs ϵ_3 with $f(\epsilon_3) = \epsilon_3$. The FPs of the maps are given by $\epsilon_3 = -0.5 \equiv 0.5$ for the linear map and $\epsilon_3 = 0 \equiv 1$ for the sinusoidal map.

To determine the Markov partitions of these maps we begin with a few general considerations. The end points of the regions of the Markov partition are given by the images of the end points of the intervals of monotony of the corresponding map. Obviously, there are two classes of these intervals: The intervals of the first class are limited by the end points of the unit interval, whereas the intervals of the other class are limited on one side by an endpoint of the unit interval and on the other side by an image ϵ_i of one of the extrema. The first class of intervals of monotony simply maps the complete phase space and therefore generates only the trivial Markov partition (which contains the complete phase space as its only region). The nontrivial partitions, however, are determined by the second class of intervals.

The end points of the intervals of monotony are given by the images ϵ_i of the extrema r_i of the map when propagating forward in time. To achieve a finite depth of the partition, the extrema are to be mapped onto a finite set of points within a number of iterations. Therefore the images ϵ_i of the extrema have to be mapped onto a dynamically invariant set after a finite number of points. For this kind of mapping only three ways are possible: The image ϵ_i of an extremum r_i is mapped after a finite number of steps

- onto itself
- onto the image ϵ_j of an other extremum $i \neq j$
- onto one of the trivial FPs ϵ_3 of the map.

Figs. 26, 27 and 28 illustrate these three transitions with examples from the sinusoidal map. The symmetries of the two maps considered here prevent the mixing of the above three cases. The number of iterations necessary to map ϵ_i to ϵ_j is the fineness of the partition. The search for parameter values related to given partitions is essentially a search for FPs of the function $f_a(\epsilon_i) - \epsilon_j$ depending on the parameter a, which can be performed applying the ST method. The transformed time-continuous systems have a particularly simple structure:

$$\dot{a} = C \cdot [f_a^{(p)}(\epsilon_i) - \epsilon_j]$$

The discretised version is

$$a_{n+1} = a_n + \lambda \cdot C \cdot [f_{a_n}^{(p)}(\epsilon_i) - \epsilon_j] \tag{33}$$

with the step size λ. The coefficient C can possess the values $C = \pm 1$. In contrast to the applications of the ST method discussed so far, the propagation of the transformed system takes place in parameter space whereas the step-size of the algorithm is determined in phase space of the map. Thereby one has to keep in mind that the points ϵ_i and ϵ_j also depend on the parameter a and the above Eqn. (33) is therefore a dynamical system for the parameter a. The dependence on a is implicit and highly nonlinear. Its complex behaviour gets more and more pronounced with increasing number p of iterations. The regions of the resulting Markov partition are given by the images of the extrema ϵ_1 and ϵ_2. A map with two extrema and p iterations therefore yields a partition with $2p+1$ regions. By symmetry of the underlying maps, the resulting partitions are themselves symmetric in the corresponding unit interval. *This adaption of the ST method demonstrates the ability of the algorithm to detect FPs and zeros of functions which are not given in a analytically closed form.*

7.3 Implementation of the algorithm

The distribution of the initial points for the propagation of the transformed system is of prominent importance for the effective performance of the method. An unfortunate choice of the distribution does not prevent a complete detection of all partitions, but requires a higher overall density of the initial points. However, the efficiency of the method can be increased significantly by a more sophisticated distribution of initial points. As the parameter a of the map approximately equals the derivative $\mathrm{d}f_a^{(p)}(r)/\mathrm{d}r$, the density of the partitions in the parameter space increases with a. This should correspond to an increasing density of initial points. The linear map has constant derivative, therefore the density grows proportional to a^{p+1} (p is the depth of the iteration and the fineness of the partition). The numerical calculations were performed on a grid with approximately 1000 points, weighted with the density $\rho \propto a^{p+1}$ of the expected Markov partitions. For the step size λ of the transformed systems $\lambda = 10^{-2}$ proved to be a good value.

With the sinusoidal map, the dependence of the density of partitions on a is less regular. This is related to the appearance of tangential zeros of the function $f_a(\epsilon_i) - \epsilon_j$.

Tangential zeros are always accompanied by a relatively large region containing no further zeros. Nevertheless, the density of partitions increases significantly with the parameter a for this map, too. This is why we chose the same distribution $\rho \propto a^{p+1}$ in the interval $[0, 10]$ for the initial points as for the linear map. The determination of the optimal value of the parameter λ turns out to be less straightforward compared to the linear map, too. This is due to the fact that the function $F(a) := f_a^{(p)}(\epsilon_i) - \epsilon_j$ in Eqn. (33) shows transversal zeros with $\mathrm{d}F(a)/\mathrm{d}a \neq 0$ as well as tangential zeros with $\mathrm{d}F(a)/\mathrm{d}a = 0$. The transversal zeros are a minor obstacle for detection. The value of $F(a)$, which is proportional to the step size of the algorithm according to Eqn. (33), varies linearly even in close neighbourhood of the zero: The step size is finite even close to the solution, which allows its detection with moderate numerical effort. Approaching a tangential zero of the sinusoidal map, the step size $F(a)$ reduces with a higher than linear order of the distance to the zero. This results in a slowing-down of the algorithm at a wider distance from the solution. To locate a tangential zero with an accuracy of 10^{-14}, up to 10^7 times more iterations are necessary compared to a transversal zero. On the other hand, a flat $F(a)$ in Eqn. (33) allows a much larger value of the step size λ. With $\lambda = 10$, only 10^6 steps are sufficient to locate the zero with an accuracy of 10^{-14}. Therefore the use of a small λ far from the zero and a larger value close to it is an ideal combination. To achieve this, we stopped the numerical propagation when reaching a critical value of $F(a) = f_a^{(p)}(\epsilon_i) - \epsilon_j$ and continued the trajectory with the Newton algorithm, which had a better performance in this case. This corresponds to an introduction of a variable parameter $\Lambda \to \lambda(a)$:

$$\lambda = \lambda(a) = \left[\frac{d}{d\,a} \left(f_a^{(p)}(\epsilon_i) - \epsilon_j \right) \right]^{-1}$$

with

$$\frac{d}{d\,a} \left(f_a^{(p)}(\epsilon_i) - \epsilon_j \right) = \left[\prod_{\substack{i=0 \\ r_i = f_a(r_{i-1})}}^{p-1} (1 + 2\pi a \sin(2\pi\epsilon_i)) \right] \cdot \frac{d\,\epsilon_i}{d\,a} - \frac{d\,\epsilon_j}{d\,a}$$

According to Eqn. (32) we have

$$\frac{d\epsilon_1}{da} = -\frac{d\epsilon_2}{da} = \sin\left(\arccos\left(\frac{-1}{2\pi a} \right) \right) = \sqrt{1 - \frac{1}{(2\pi a)^2}}$$

The trivial FPs are independent of a, $d\epsilon_3/da = 0$. The number of iterations necessary for the Newton-algorithm to converge with an accuracy of 10^{-14} are of the order of 10^3.

Most initial points converge with only 10^2 iterations. For the convergence of the Newton algorithm, it is not relevant whether the zero is transversal or tangential. With both maps, the completeness of the set of Markov partitions found can be numerically verified by increasing the number of initial points until saturation of the number of detected partitions is reached.

7.4 Numerical results

7.4.1 Linear map

In Fig. 29 the distribution of parameter values corresponding to a Markov partition with fineness $p = 1$ and $p = 2$ are shown. The integer values of a are related to the trivial partitions. For these values, both extrema coincide. The map is continuous for any p, and each monotonous interval maps the whole interval $[0, 1]$ completely onto itself. Therefore the interval is itself the only partition for this value of a. The number of parameter values corresponding to nontrivial partitions increase with a: The function $F(a)$, whose zeros are to be determined, grows as a^{p+1}, but is folded back into the unit interval. Therefore the density of the Markov partitions increases as a^{p+1} in parameter space.

7.4.2 Sinusoidal map

The distributions of the Markov partitions of the sinusoidal map are shown in Figs. 30, 31 and 32. Compared to the corresponding distributions of the linear map, the number of partitions of this map is significantly larger which is why the distributions are shown in the form of histograms. The high density of partitions in parameter space has probably its reason in the unimodal character of the sinusoidal map. It is in some respect a superposition of two unimodal maps. The existence of both a rising and a falling branch allows a larger variability of possible mappings of the extrema compared to a map with just one rising branch like the linear map. The fact that there are more ways to map the extrema implies a higher density of partitions in the unit interval. Additionally, the distribution obviously has windows close to integer values of the parameter. These windows are remarkably dominant for the partitions corresponding to the transition $\epsilon_1 \rightarrow \epsilon_3$. This feature is due to a bifurcation process located at the extremum of the map and can therefore also be traced back to the unimodal character of the map. The windows are

related to the appearance of stable FPs close to the extremum. For a certain parameter interval, these stable FPs attract the trajectories starting from the extremum and therefore prevent the mapping of the extremum in regions of the phase space further off. Let us discuss this mechanism in more detail: The dynamics close to the extrema for $a = 1$ is sketched in Fig. 33. As the mapping behaviour of the extremum determines the existence and properties (fineness) of the partition, the dynamics in the phase space area around the extremum is of prominent importance. For integer values of the parameter a the FP r_0 is located very close to the extremum. The position of r_0 is the solution to the equation (without loss of generality the depth of iteration is set $p = 0$)

$$f_a(r_0) = r_0$$

i.e.

$$r_0 + a \cdot \sin(2\pi r_0) = r_0 + n$$

n is an integer number and can be chosen $n = 1$ in the following. For $a = a_1 = 1$, the map $f_a(r)$ touches the line $y(r) = r$ tangentially in the point $r_0 = 1/4$. This FP is marginally stable, since $\mathrm{d}f_a(r)/\mathrm{d}r = 1$. As discussed above, the trajectories starting at the extrema determine the partition. This trajectory is displayed in Fig. 33 b) for the value $a_1 = 1$. It approaches the tangential FP r_0 without reaching it. A mapping of this extremum onto itself, onto the corresponding other extremum or one of the trivial FPs is therefore not possible. The dynamics is qualitatively similar for values of a which are slightly smaller than a_1, as shown in Fig. 33 a). For these values of the parameter, no FP close to the extremum exists, but the dynamics is still intermittent. The trajectory remains in a small area of the phase space close to the extremum for a long time before being pushed further away. A mapping of the extremum in a remote region of phase space is not possible within a few steps of iteration, therefore no partition exists for this range of parameter value, too. The window in the distribution of partitions extends therefore even to values less than an integer value. When increasing a, one finds for $a = a_0 = \sqrt{1/(4\pi)^2 + n^2} \approx 1.012586$ the only value in the window that corresponds to a Markov partition. For this value, the extremum equals the FP r_0 (see Fig. 33 c)). The partition corresponds therefore to a transition $\epsilon_1 \to \epsilon_1$ (and because of the symmetry of the map also $\epsilon_2 \to \epsilon_2$). This FP is stable and remains so for a slight enhancement of the value of a (see Fig. 33 d)). A trajectory started in the extremum now converges in the stable FP, which again impedes

the existence of a finite partition. Only for values of a that are large enough to render r_0 unstable the trajectory can leave the region close to the extremum and possibly create a Markov partition. (see Fig. 33 f)). This bifurcation appears for a parameter value of $a = a_{-1} = \sqrt{1/(\pi)^2 + n^2} = 1.049439$ (see Fig. 33 e)) with the gradient of the function in this point being $\mathrm{d}f_a(r)/\mathrm{d}r = -1$. Similar to the situation at the lower boundary of the window in the distribution, the formation of partitions is suppressed even for values of a slightly larger than a_{-1}, as the trajectory remains close to r_0 for a long time. However, for these values only partitions with a high number of regions can be expected. The window in the distribution containing just one parameter value (corresponding to the transition $\epsilon_1 \to \epsilon_1$) contains the interval $[a_1, a_{-1}]$. The length of this interval decreases for increasing parameter a, since the curvature of the map at the extrema ϵ_1 and ϵ_2 grows with a.

7.5 Transients

Markov partitions also occur when extrema are mapped onto a PO (and not a single FP) not containing the extrema themselves. Therefore additional extrema can be found by looking for parameter values a that correspond to a closed orbit with period p with one of the extrema being its nth pre-image:

$$f^{(n+p)}(\epsilon_i) = f^{(n)}(\epsilon_i) \qquad \text{and} \qquad f^{(n+p-1)}(\epsilon_i) \neq f^{(n-1)}(\epsilon_i)$$

These parameter values can be found with a similar method as the more simple partitions with the extrema being part of the PO. The ansatz for the dynamical system for a is

$$a_{n+1} = \lambda \cdot C \cdot [f_{a_n}^{(n+p)}(\epsilon_i) - f_{a_n}^{(n)}(\epsilon_i)]$$

When propagating this system we meet the problem that besides the desired orbits with a transient of length n also orbits are found with a shorter transient or even with no transient behaviour at all. This is not a fundamental problem, but the number of partitions found with this ansatz is considerably large which complicates the test of convergence of the method by means of saturation.

8 Integration of partial differential equations by applying the ST method

8.1 Types and properties of partial differential equations

In this chapter we explain how to extend the ST method in order to integrate nonlinear partial differential equations (PDEs). By nature the results of this chapter are preliminary and there are lots of possibilities to improve the approach we are going to describe. Generally, the numerical integration of PDEs is a vast field since they are central to the description of many physical systems. Examples are hydrodynamics of fluids, astrophysical models, biological processes or the evolution of electro-magnetic fields. For a numerical treatment, the fundamental mathematical distinction of PDEs into hyperbolic, parabolic and elliptic PDEs is of minor importance. Many problems described by PDEs are of mixed type, either in their generic form or in their numerical implementation. A different distinction seems to be more relevant: For the numerical stability of the algorithm it is important, whether the integration is supposed to be performed in both space and time (initial value problem) or merely with respect to the spatial coordinates (boundary value problem). In the following, we focus on the former case of time-dependent problems. With the initial distribution at an initial time t_0 given by $u(x, t_0)$, the PDE determines how $u(x, t)$ evolves in time. The numerical code is expected to describe this evolution with a certain given accuracy.

Integrating an initial value problem requires a high stability of the numerical algorithm, since only the initial distribution and possibly certain boundary values are given. There is a variety of methods to integrate PDEs. In most cases the choice of the method is determined by the nature of the problem. The integration of a smooth spatially periodic problem for example suggests the application of Fourier methods. However, these would cause serious problems when used for integration of systems with discontinuities. The most important methods of the numerical implementation are the method of finite differences, the method of finite elements, Monte Carlo methods, spectral methods and variational methods [374–377]. To employ the method of finite differences the differential equation is discretised on a time-spatial grid. The method of finite elements is mainly used to solve boundary value problems [374, 375]. It has many applications in the technical and

engineering field, since the method can easily be adapted to systems with irregular and complex geometry. As mentioned above, the spectral methods are applicable for both very irregular geometries and smooth functions. Generally, they converge faster than methods employing finite differences, but there might arise problems with the discontinuities in the system [376, 377].

8.2 Discretisation

We will apply the ST method to the integration of several types of nonlinear PDEs. To this aim, we discretise the differential equation on a grid. Let us outline this procedure in some more detail: The points on the grid have a constant separation Δx in the spatial direction and Δt in the temporal direction. The continuous distribution $u(x,t)$ corresponds to the discretised distribution u_j^n, with n being the time index and j the spatial index. In this way, we get a high-dimensional, nonlinearly coupled system of equations. The solution of this system of equations yields the "new" distribution $u(x, t+\Delta t)$. In most of the cases discussed in the following, the discretisation is done in the following way [378]:

$$u_t(x,t) \longmapsto \frac{u_j^{n+1} - u_j^n}{\Delta t} \tag{34}$$

$$u_x(x,t) \longmapsto \frac{u_{j+1}^n - u_{j-1}^n}{2\Delta x} \tag{35}$$

$$u_{xx}(x,t) \longmapsto \frac{u_{j+1}^n - 2u_j^n + u_{j-1}^n}{(\Delta x)^2} \tag{36}$$

$$u_{xxx}(x,t) \longmapsto \frac{u_{j+2}^n - 2u_{j+1}^n + 2u_{j-1}^n - u_{j-2}^n}{2(\Delta x)^3} \tag{37}$$

$$u_{xxxx}(x,t) \longmapsto \frac{u_{j+2}^n - 4u_{j+1}^n + 6u_j^n - 4u_{j-1}^n + u_{j-2}^n}{(\Delta x)^4} \tag{38}$$

This scheme of discretisation is called FTCS-scheme (forward time, centred space) [237]. It indicates, that the approximation is performed including the spatially neighbouring points only (centred space), but not the points of the grid shifted in time. The distribution at the "new" point of time u_j^{n+1} appears only in the time derivative Eqn. (34) (forward time). The equation discretised in this way can be solved explicitly for u_j^{n+1}, j given, i.e. we have an explicit scheme. In case the discretised distribution u_j^n is known for

all j and a particular n, the distribution u_j^{n+1} can be calculated directly. However, the FTCS scheme is not stable for hyperbolic dynamical systems. There are problems when integrating e.g. diffusive equations with the FTCS scheme, due to the fact that the discrete approximation is only accurate up to first order in time. The demands on an integration algorithm for systems like these are high: The dynamics is composed of fluctuations on different length scales, which are to be reproduced as precisely as possible. However, the temporal steps of the integration are generally large compared to the typical smallest time scales occurring in the system. The FTCS scheme is better suited to reproduce the small scale fluctuations, but amplifies them excessively when larger step sizes of the integration are used. Divergences of the algorithm may be the consequence. The FTCS scheme on its own is therefore less suited for the integration of nonlinear PDEs. It is desirable to combine the FTCS scheme with an algorithm that possibly reproduces the small scale fluctuations less accurate, but converges in the correct equilibrium distribution in the long time limit $\Delta t \to \infty$. This property guarantees the stability of the discretisation scheme. A possible discretisation having this feature is the so-called complete implicit scheme [237]. The discretised derivatives agree with the derivatives of the FTCS scheme Eqn. (35) through (38) except that they are evaluated at time $n+1$ instead of n. This method works, so to speak, backwards in time, the sought-after distribution u_j^{n+1} is given only implicitly by the u_j^n. However, this is a minor problem for the implementation: The system of equations to solve is given as a tridiagonal banded matrix for a linear system, in case of a nonlinear system this tridiagonal matrix is obtained after a linearisation about the known distribution u_j^n. Tridiagonal band matrices can be inverted with a relatively small amount of numerical effort.

A combination of the two discretisation schemes discussed above is ideal, as it has both the stability of the complete implicit scheme as well as the accuracy of the FTCS scheme. The resulting algorithm is second order accurate in space and time. The arithmetic mean of the FTCS scheme and the complete implicit method is such a combination and is called Crank-Nicholson scheme [237]. It is applied to all systems discussed in this section.

8.3 Implementation of the ST method

The discretisation of the PDEs is performed on a grid of N points and results in a N-dimensional coupled nonlinear system of equations. The distribution $u(\mathbf{x},t)$ at the time t now is given as a vector $\mathbf{u}^n = (u_1^n, u_2^n, u_3^n, ..., u_N^n)^T$ at the discrete point of time n. The resulting system of equations can be written in the following way:

$$\mathbf{F}(\mathbf{u}^n, \mathbf{u}^{n+1}) = 0 \quad , \quad \mathbf{F} = (F_1, F_2, ..., F_N)^T \tag{39}$$

We can thus interpret the evolution equation as a fixed point problem. The vector $\mathbf{u}^{n+1}$ is a zero of the function $\mathbf{F}$ defined on a high-dimensional phase space. This interpretation allows the application of the ST method in order to solve Eqn. (39) for the vector $\mathbf{u}^{n+1}$. To this aim, we perform iterations $\mathbf{u}_{(p)}^{n+1} \rightarrow \mathbf{u}_{(p+1)}^{n+1}$ as follows:

$$\mathbf{u}_{(p+1)}^{n+1} = \mathbf{u}_{(p)}^{n+1} + \lambda \mathbf{C}_i \mathbf{F}(\mathbf{u}_{(p)}^n, \mathbf{u}^{n+1}) \quad , \quad \mathbf{u}_{(0)}^{n+1} = \mathbf{u}^n$$

The process of iteration converges in the solution $\mathbf{u}^{n+1}$. It starts with the distribution $\mathbf{u}_{(0)}^{n+1} = \mathbf{u}^n$ at the "old" point of time n. This is reasonable, since $u(\mathbf{x},t)$ is supposed to change little within a short time step Δt (the Euler approximation Eqn. (34) is a good approximation only for small Δt). All possible $\mathbf{C}_i$-matrices with one non vanishing entry± 1 in each row and column have been tested for their possible use in the ST-transformed system with a small grid ($N = 5...9$). In all systems studied (see below), the unit matrix is the only one resulting in convergence of the algorithm, which reduces the numerical effort significantly. The overall sign of the matrix is negative in cases where the time derivative Eqn. (34) possesses a positive sign in the function $\mathbf{F}(\mathbf{u}_{(p)}^n, \mathbf{u}^{n+1})$ and vice versa. The reason for the exclusive appearance of the unit matrix might be the structure of the stability matrix $(\mathbf{S_F})_{ij} = \partial \mathbf{F}_i(\mathbf{u}^n, \mathbf{u}^{n+1}) / \partial u_j^{n+1}$ of the N-dimensional FP problems in the FP $\mathbf{u}^{n+1}$: The entries in the diagonal include the term $(\Delta t)^{-1}$ for all systems considered. These diagonal elements dominate for small time steps Δt. The other entries of the stability matrix contain terms proportional to $(\Delta x)^k$, $k = 1, ..., 4$. However, these entries are generally small compared to the diagonal entries. This is caused by the fact that for a stable propagation of the distribution, the time step Δt can be chosen very small without a possible danger of instabilities and divergencies. In contrast to this, the spatial step size Δx can not be set arbitrarily small. As the geometry of the system (i.e. the size of

the phase space) is not supposed to change, a reduction of Δx corresponds to an increase of the dimensionality of the system, which generally causes additional instabilities in the propagation. The stability matrix describes the dynamics close to the FP $\mathbf{u}^{n+1}$. In case it is diagonally dominated, the matrix has eigenvalues close to the diagonal elements. If all diagonal elements are real and have the same sign, as in all the systems discussed, these properties can be expected to be met for the individual eigenvalues, too. The $\mathbf{C}_i$ matrices that stabilise a FP with the stability matrix $\mathbf{S}$ are required to result in negative real parts of the eigenvalues of the product $\mathbf{C}_i\mathbf{S}$. For a diagonally dominating matrix, a multiplication with the negative unit matrix is therefore sufficient for stabilisation of the corresponding FP.

It is an interesting fact that an algorithm similar to the ST method has already been invented to solve elliptic boundary problems [237]: Let $\mathcal{L}$ be an elliptic differential operator, ρ a source term and u a solution of the PDE

$$\mathcal{L}u = \rho \tag{40}$$

This equation can be written as a diffusive system:

$$\frac{\partial u}{\partial t} = \mathcal{L}u - \rho \tag{41}$$

An initial distribution u, not necessarily the solution of Eqn. (40), relaxes for $t \longrightarrow \infty$ to an equilibrium distribution when propagated according to Eqn. (41). This equilibrium distribution is the solution of the original elliptical problem Eqn. (40). To perform the propagation, Eqn. (41) is discretised according to Eqns. (34) through(38), subsequently following the FTCS-scheme. As this is an explicit scheme, the discretised equations can be propagated directly. Eqn. (41) is exactly the continuous form of the ST-transformed system (see section 3.4), with the unit matrix as the $\mathbf{C}_i$-matrix. This method of solving elliptic boundary problems is known as "Jacobi's method". It was first described by Jacobi (1804-51), but is not widely used due to its slow convergence.

In the following we discuss the adaption of the ST method to the integration of nonlinear PDEs. In each of the examples to be discussed, the ST method is used to find solutions of the systems of equations obtained after discretisation according to the Crank-Nicholson scheme. Optimal values have been chosen for the size of the spatial grid, the geometry of the system (size of the phase space) and the size of the time steps Δt. To validate

the results of the calculations, each particular system Eqn. (39) is propagated using the Newton algorithm, too. This is performed by calculating the zero $\mathbf{u}^{n+1}$ of the vector valued function $\mathbf{F}(\mathbf{u}^n, \mathbf{u}^{n+1})$ in Eqn. (39) approximately by iteration of $\mathbf{u}^{n+1}_{(1)}, \mathbf{u}^{n+1}_{(2)}, \mathbf{u}^{n+1}_{(3)}, ...,$ $\lim_{p\to\infty} \mathbf{u}^{n+1}_{(p)} = \mathbf{u}^{n+1}$ and $\mathbf{u}^{n+1}_{(0)} = \mathbf{u}^n$ of the following linearised equation:

$$\mathbf{F}(\mathbf{u}^n, \mathbf{u}^{n+1}_{(p)}) + \mathbf{S_F} \cdot (\mathbf{u}^{n+1}_{(p+1)} - \mathbf{u}^{n+1}_{(p)}) = 0 \quad \text{with} \quad (\mathbf{S_F})_{ij} = \frac{\partial \mathbf{F}_i(\mathbf{u}^n, \mathbf{u}^{n+1})}{\partial u^{n+1}_j} \tag{42}$$

The stability matrix $\mathbf{S_F}$ is a tridiagonal matrix in case of fixed boundary conditions in case only three point approximations of the form (35) and (36) are in use. When five point approximations like in Eqns. (37) and (38) are employed, the corresponding stability matrices are penta-diagonal. Inversion of these band diagonal matrices is can be done with a comparatively small numerical effort. The solution of Eqn. (42) is more complicated when periodic boundary conditions are required. The cyclic coupling of the dynamics results in components of the stability matrix in the lower left and upper right corner additional to the band diagonal ones. In this case, the matrix can only be inverted using significantly slower numerical routines.

8.4 Examples

8.4.1 Burgers equation

The Burger system is an example of a diffusive system including a nonlinear term

$$u_t = 2uu_x + u_{xx} \tag{43}$$

The term $u_t = u_{xx}$ on its own describes the spreading of the initial distribution, whereas the term $u_t = 2uu_x$ leads to an increasing concentration. The interplay of these two mechanisms results in a stable dynamics which allows the existence and propagation of solitary solutions in form of shock waves. Eqn. (43) is integrated numerically to propagate a given initial distribution. To this aim, we make use of the ST method to solve the complicated high-dimensional nonlinear system of equations. Discretisation of eqn. (43) comes first: With Eqns. (34) through (38) and the Crank-Nicholson scheme we get

$$\frac{u_j^{n+1}-u_j^n}{\Delta t} = \frac{u_{j+1}^n+u_{j-1}^n+u_{j+1}^{n+1}+u_{j-1}^{n+1}}{4}\ \frac{u_{j+1}^n-u_{j-1}^n+u_{j+1}^{n+1}-u_{j-1}^{n+1}}{4\Delta x} + \frac{u_{j+1}^n-2u_j^n+u_{j-1}^n+u_{j+1}^{n+1}-2u_j^{n+1}+u_{j-1}^{n+1}}{2(\Delta x)^2} \tag{44}$$

The solitary solutions of the Burgers equation can be obtained easily with help of the Hopf-Cole transformation $u \mapsto v$, $v_x = uv$ and the ansatz $v(x,t) = v(x-ct)$ (see e.g. ref. [379]). The solution $u_s(x,t)$ is

$$u_s(x,t) = \frac{-c}{1+\exp\left[c(x-x_o-ct)\right]}$$

The solution $u_s(x,t)$ is a shock wave localised in $x = x_o$ (i.e. u_x is maximal in $x = x_o$). The quantity c represents both the amplitude and the velocity of the wave. An example of a time evolution is shown in Fig. 34. The superposition of shock waves with different amplitude and velocity is particularly interesting: Fig. 35 shows two wave fronts, moving into the same direction with different velocities. At collision the faster wave absorbs the slower one. The propagation continues with the sum of the individual velocities. This shows that the solitary solutions are not real solitons which would penetrate each other without any distortion. A collision of two solitary solutions of the Burgers equations, which move in opposite directions, results in a shock wave moving with the difference of the individual velocities. Fig. 36 shows the time evolution of two shock waves with exactly opposite velocities: After the collision, the distribution is merely a stationary wave front.

Eqn. (44) is solved with the ST method on a grid with $N = 100$ (Fig. 34) and $N = 170$ (Figs. 35 and 36) points, respectively. The size of the time steps is $\Delta t = 0.2$.

8.4.2 The Fitzhugh-Nagumo equation

The Fitzhugh-Nagumo system has been developed as a simple model featuring the propagation of excitation pulses in nerve cells [380]. It is given by

$$u_t = \frac{1}{2}u_{xx} + (a-u)(u^2-1) \quad , \quad -1 < a < 0 \tag{45}$$

Discretisation on a grid with help of Eqns. (34) through (38), using the ST method, yields:

$$\begin{aligned}\frac{u_j^{n+1}-u_j^n}{\Delta t} &= \frac{1}{2}\frac{u_{j+1}^n-2u_j^n+u_{j-1}^n+u_{j+1}^{n+1}-2u_j^{n+1}+u_{j-1}^{n+1}}{2(\Delta x)^2} + \ldots \\ \ldots &+ \left(a-\frac{u_{j+1}^n+u_{j-1}^n+u_{j+1}^{n+1}+u_{j-1}^{n+1}}{4}\right)\left(\left(\frac{u_{j+1}^n+u_{j-1}^n+u_{j+1}^{n+1}+u_{j-1}^{n+1}}{4}\right)^2-1\right)\end{aligned}$$

The Fitzhugh-Nagumo system has the following solitary solution [379]:

$$u = \tanh(x-at) \tag{46}$$

Fig. 37 shows the time evolution of a distribution Eqn. (46) with $a = -0.5$. We used a spatial grid with $N = 100$ points and a time step $\Delta t = 0.2$.

8.4.3 Real Ginzburg-Landau equation

As the next example we chose the real Ginzburg-Landau system. It is a special case of the complex Ginzburg-Landau system, which describes the evolution of a complex field in time. This system has a long history in the physics of dynamical systems: It is a good approximation to the amplitude dynamics of spatio-temporal hydrodynamic systems close to instabilities, leading to a turbulent dynamics. It also acts as a model system in the theory of phase transitions and of superconductivity and has many other applications [381–383]. In contrast to the complex Ginzburg-Landau equation, the real one (all coefficients are real), given by

$$u_t = u_{xx} + u - u^3,$$

shows a comparatively simple behaviour. To our knowledge no nontrivial solitary solutions exist when also the distribution $u(x,t)$ is real. Discretisation following the Crank-Nicholson scheme yields

$$\begin{aligned}\frac{u_j^{n+1}-u_j^n}{\Delta t} &= \frac{u_{j+1}^n-2u_j^n+u_{j-1}^n+u_{j+1}^{n+1}-2u_j^{n+1}+u_{j-1}^{n+1}}{2(\Delta x)^2} + \ldots \\ \ldots &+ \frac{u_{j+1}^n+u_{j-1}^n+u_{j+1}^{n+1}+u_{j-1}^{n+1}}{4} - \left(\frac{u_{j+1}^n+u_{j-1}^n+u_{j+1}^{n+1}+u_{j-1}^{n+1}}{4}\right)^3\end{aligned}$$

In Fig. 38 the time development of a stationary distribution is displayed. It shows a relaxation to the constant and stationary distribution $u(x,t) = 1$. For this propagation, a spatial grid of $N = 100$ points and time steps $\Delta t = 0.1$ have been utilised.

8.4.4 Korteweg-de-Vries equation

The Korteweg-de-Vries equation is one of the most basic equations with solutions in form of solitons [384]. For the physics and mathematics of solitons in nonlinear PDEs we refer the reader to ref. [379].

The solitons of the Korteweg-de-Vries equation

$$u_t = 6uu_x - u_{xxx} \tag{47}$$

are bell-shaped, localised solutions

$$u(x,t) = -\frac{q^2}{2}\frac{1}{\cosh^2[q(x-vt)]} \tag{48}$$

with $v = q^2$, which move in one direction without changing their shape. It is a remarkable feature and a generic property of nonlinear systems, that generally the velocity increases with its amplitude. The solution (48) of the Korteweg-de-Vries equation (47) is negative. However, by scaling $u \longmapsto -u/6$ an alternative version of the Korteweg-de-Vries equation can be obtained

$$u_t + uu_x + u_{xxx} = 0 \tag{49}$$

which has positive solutions

$$u(x,t) = 3q^2\frac{1}{\cosh^2[q(x-vt)]} \tag{50}$$

The numerical integration is performed using the discretised form of Eqn. (47), following Eqns. (34) through (38)

$$\frac{u_j^{n+1} - u_j^n}{\Delta t} = 6u_j^n\frac{u_{j+1}^n - u_{j-1}^n + u_{j+1}^{n+1} - u_{j-1}^{n+1}}{4\Delta x} - \frac{u_{j-2}^n + 2u_{j-1}^n - 2u_{j+1}^n + u_{j+2}^n}{4(\Delta x)^3} \tag{51}$$

Fig. 39 shows the time propagation of the distribution (48) with $q = 0.4$. For the discretisation, we used a spatial grid with $N = 120$ points and time steps $\Delta t = 0.1$. For this propagation, fixed boundary conditions have been chosen, but periodic boundary conditions are as well straightforward to implement.

8.4.5 Kuramoto-Sivashinsky equation

The Kuramoto-Sivashinsky equation [385–387] is one of the most fundamental and best studied field equations describing spatio-temporal chaotic dynamics. Therefore it is often

considered as a model system for the investigation of spatio-temporal chaos and turbulent systems. In many physical systems the Kuramoto-Sivashinsky equation appears as an amplitude equation. Its qualitative behaviour is relatively simple: A characteristic feature of the spatio-temporal chaotic dynamics describing turbulent dynamics is the simultaneous existence of at least two length scales [388]. The small scale time evolution is governed by the deterministic dynamics. In contrary, the dynamics seems to be stochastic on larger length scales. The field equations couple these two species of dynamical behaviour. The quantitative interplay between these two scales is essential for the appearance of turbulence and spatio-temporal chaos and is subject of many studies and investigations (see for example ref. [162]).

The Kuramoto-Sivashinsky equation reads

$$u_t = (u^2)_x - u_{xx} - \nu u_{xxxx} \tag{52}$$

Its small scale cells have an extension of the order of $l_0 = 2\sqrt{2}\pi$ and are limited by linear instability. Nonlinear coupling of different cells results in the appearance of global patterns on a much larger length (and time) scale than l_0. The Kuramoto-Sivashinsky equation describes a large number of physical processes, e.g. the dynamics of a flame front of a burning flame. The "flame front" $u(x,t)$ has a compact support and a periodic phase space coordinate $x \in [0, 2\pi]$. The parameter ν of the system is a fourth order viscosity parameter. The term νu_{xxxx} has a damping effect on the dynamics by suppressing oscillations of shorter wavelength and relatively large amplitude. With decreasing viscosity, the stability of the flame front is reduced and turbulence is more pronounced. To propagate the Kuramoto-Sivashinsky system in time, the Eqn. (52) is discretised according to the Crank-Nicholson scheme

$$\begin{aligned}
\frac{u_j^{n+1} - u_j^n}{\Delta t} &= \left(\frac{u_{j+1}^n - u_{j-1}^n}{2\Delta x} u_j^n + \frac{u_{j+1}^{n+1} - u_{j-1}^{n+1}}{2\Delta x} u_j^{n+1} \right) \\
&\quad -\frac{1}{2} \left(\frac{u_{j+1}^n - 2u_j^n + u_{j-1}^n}{(\Delta x)^2} + \frac{u_{j+1}^{n+1} - 2u_j^{n+1} + u_{j-1}^{n+1}}{(\Delta x)^2} \right) \\
&\quad -\frac{\nu}{2} \left(\frac{(u_{j+2}^n + u_{j-2}^n) - 4(u_{j+1}^n + u_{j-1}^n) + 6u_j^n}{(\Delta x)^4} \right. \quad + \ \ldots \\
&\qquad \ldots \ + \left. \frac{(u_{j+2}^{n+1} + u_{j-2}^{n+1}) - 4(u_{j+1}^{n+1} + u_{j-1}^{n+1}) + 6u_j^{n+1}}{(\Delta x)^4} \right)
\end{aligned}$$

Figs. 40 and 41 show the results of the integration with the ST method. The discretisation is performed on a spatial grid with $N = 170$ points and time steps $\Delta t = 0.1$. In Figs. 40 and 41 periodic boundary conditions are implemented, but integration with fixed boundary conditions (distribution has zero value at the boundaries) is also possible. In Fig. 40 the viscosity parameter is chosen to be $\nu = 1.5$, in Fig. 41 it is $\nu = 6.0$. Obviously, for a larger value of ν less fluctuations on a smaller time and length scale appear.

9 Summary and outlook

9.1 Summary

This review discusses in detail the tool of stability transformations, its applications and extensions to new problems. The focus is essentially threefold: First to understand the theoretical foundations of the ST method, second, to provide algorithms and numerical implementations for discrete and time-continuous systems and third to extend the ST approach in order to solve problems such as the finding of Markov partitions and the propagation of nonlinear partial differential equations.

The ST method was originally developed in order to detect unstable periodic orbits in chaotic dynamical systems. These orbits form the skeleton of the dynamics of nonlinear dynamical systems and are a key ingredient for the understanding of various features related to chaotic dynamics.

It is the basic principle of the ST method to change the stability properties of the unstable periodic orbits – while keeping their positions – by application of an appropriate transformation of the dynamical system. The orbits stabilised in such a way can be detected straightforwardly by propagation of the corresponding system.

The major advantage of the ST approach as compared with other methods is the outstanding global convergence property. The basins of attraction exceed by far the linear neighbourhood of the periodic orbits and are topologically simply connected areas in phase space. At a large distance from the periodic orbit, the rate of convergence is high. Another beneficial feature of the ST method is its ability to selectively stabilise periodic orbits: A parameter λ of the approach is almost strictly related to the stability properties of the orbits. The smaller the value of λ is, the larger the instability eigenvalue of the orbits to be detected can be. This allows to rapidly detect the least unstable periodic orbits of a chaotic system, which can then be used in particular versions of so-called stability ordered cycle expansions.

For these advantages, one has to pay a price: A series of stability transformations has to be applied in order to principally (provided λ is small enough) detect a complete set of orbits of a given length. However, this complete set of $2^n n!$ stability transformations (applied to a n-dimensional dynamical system) contains a certain redundancy. To lighten

the computational burden, a minimal set of transformations necessary for the detection of the complete set of periodic orbits is desirable. For $n = 2$ and in addition to analytical studies, a geometrical ansatz was developed which allowed a classification of all possible types of periodic orbits in a two-dimensional system, making use of geometrical and topological arguments only. Moreover, this classification is in a certain sense compatible with the process of the stabilisation transformation: Application of the transformation to a dynamical system corresponds to a well-defined transition of the individual fixed points from one class to a second one. This way, two minimal sets of three transformations each are determined for two-dimensional system.

The algorithm of the stability transformation has originally been developed for detection of periodic orbits in time–discrete maps. Especially when combined with the Newton algorithm in order to enhance the speed of convergence close to the fixed point the ST approach proved to be very efficient to locate even very long periodic orbits. The fast, super-exponential convergence of the Newton algorithm in the linear neighbourhood of a close orbit guarantees an accurate localisation of the orbit with moderate numerical effort.

Periodic orbits form the skeleton of the dynamics also of time-continuous dynamical systems, given by a set of nonlinear differential equations. The ST approach is applicable also to this broad and outstandingly important class of systems. For this task, the stability transformations of the discrete, properly defined Poincaré map of the system are performed. This approach is universal and is easily adapted to a large class of time-continuous systems, possessing an either fully chaotic or mixed phase space. Systems studied include the well known Lorenz system, the classical Hydrogen atom in a homogeneous magnetic field and the classical model of a Helium atom with and without an external laser field. The Poincaré surface of section can be a stroboscopic map or defined in terms of phase space intersections. Compared to maps, the time-continuous systems are more diverse with respect to the implementation of the algorithm of the ST method as well as to the properties of the periodic orbits localised. The position of the Poincaré surface of section can be utilised as an effective tool to specify the approximate geometry of the periodic orbits to be located. A clever choice of the set of initial points, of the parameter λ and the required number of intersection points are additional ways to steer

the outcome of the ST method.

The detection of periodic orbits with the ST method is essentially the search for zeros of a nonlinear equation given implicitly by the corresponding dynamical system. Many numerical problems can be traced back to the solution of nonlinear, highly fluctuating systems of equations. Therefore it is suggestive to apply the algorithm to more general classes of problems beyond dynamical systems. Two examples are discussed: The determination of Markov-partitions of parameter-depending maps and the propagation of partial nonlinear differential equations.

A Markov partition is a partitioning of the phase space which is dynamically invariant and is of relevance e.g. for models of deterministic diffusion. The property of a Markov partition can be traced back to a mapping of the extrema of the corresponding dynamical system onto a dynamically invariant set of points, e.g. a periodic orbit. This characteristic feature can be cast into a fixed point problem of an appropriately defined artificial dynamical system, accessible for the ST approach.

Another class of problems to be handled by the ST method is the integration of a large class of partial nonlinear differential equations. The evolution equations, when discretised in space and time, represent real, nonlinear functions in a high-dimensional space. The zeros of these functions correspond to the system propagated forward one step in time and can be obtained straightforwardly with the ST method.

9.2 Outlook

The method of stability transformation demonstrates its powerful ability to detect fixed points and periodic orbits of a large class of dynamical systems. However, although the algorithm proved its worth in many applications, the understanding of its theoretical foundations in more than two dimensions is still a challenge, caused by the mathematical complexity of the underlying problem. An enhanced understanding of the basis of the method would surely improve its practical applications. Especially when studying higher-dimensional systems the number of transformed systems to be propagated affects the numerical efficiency. Therefore it is advisable, in particular with respect to the implementation of the algorithm, to determine a minimal set of transformations for each dimension sufficient to stabilise any fixed point of the dynamical system. The geometrical

approach we presented for two dimensions could be a good starting point. It is suggestive to look for an analogy of the dynamically invariant manifolds, which allows for a similar classification as in two dimensions. Points on the surface of a $(N-1)$ sphere in a N-dimensional space might serve as this analogy. On the one hand, these points are mapped in a well-defined way by the matrices of the stability transformation, on the other hand they confine the section of phase space possibly containing the eigenvectors of the corresponding stability matrix.

A rewarding field for further application of the ST method are studies of further physical and mathematical dynamical systems. Especially for four- through six-dimensional systems the propagation of the complete set of stability transformations is numerically still practicable. In these systems, other well-known methods such as the Newton-Algorithm are less efficient due to the small extensions of the basins of attraction around the fixed points to be detected. For studies of systems with more than six dimensions the determination of the minimal set of stability transformations becomes necessary. The application of the ST method to quantum mechanical systems in the semiclassical regime is another rewarding field of future research, since one of the most prominent difficulties in these systems is the systematic detection of periodic orbits in the phase space.

The detection of spatial and temporal patterns in the time evolution of nonlinear partial differential equations describing a turbulent system is another possible extension of the ST method. In order to achieve this, the algorithm would have to be applied to a Poincaré map, which is suitably defined either as a function of spatial coordinates or as a stroboscopic map. Our applications of the ST approach to solve nonlinear partial differential equations have demonstrated that even very high-dimensional ($N > 100$) nonlinear equations can be solved.

9.3 Acknowledgements

The authors are highly indebted to Peter Schlagheck (University of Regensburg) for his considerable and productive assistance concerning the finding of the unstable periodic orbits of the helium atom in the laser field. We thank Predag Cvitanović (Georgia Tech) for fruitful discussions regarding the field of periodic orbit theory. Rainer Klages (MPI für Physik komplexer Systeme) provided valuable advise particularly concerning Markov

partitions. The collaboration with Lazarus Kapsias (University of Athens) is accepted with thanks. D.P. thanks the Max Planck Institut für Physik komplexer Systeme for kind hospitality. P.S. acknowledges the kind hospitality of the Section of Solid State Theory of the Department of Physics of the University of Regensburg. The Deutsche Forschungsgemeinschaft and the IKYDA-program are gratefully acknowledged for financial support.

References

[1] S. H. Strogatz. *Nonlinear Dynamics and Chaos.* Addison-Wesley, New York, 1994.

[2] K. T. Alligood, T. D. Sauer, and J. A. Yorke. *Chaos, and Introduction to Dynamical Systems.* Springer, New York, 1996.

[3] E. Ott. *Chaos in Dynamical Systems.* Cambridge University Press, Cambridge, MA, 1993.

[4] S. Smale and M. W. Hirsch. *Differential Equations, Dynamical Systems, and Linear Algebra.* Academic Press, San Diego 1974.

[5] H. G. Schuster. *Deterministic Chaos.* VHC Verlagsgesellschaft, Weinheim, 1989.

[6] M. C. Gutzwiller. *Chaos in Classical and Quantum Mechanics.* Springer, New York, 1990.

[7] V. Reitmann. *Reguläre und chaotische Dynamik.* Teubner, Stuttgart, 1996.

[8] T. Buzug. *Analyse chaotischer Systeme.* BI Wissenschaftsverlag, Mannheim, 1994.

[9] A. Lasota and M. C. Mackey. *Chaos, Fractals and Noise* vol. 97 of *Applied Mathematical Sciences.* Springer, New York, 1994.

[10] G. Nicolis. *Introduction to Nonlinear Science.* Cambridge University Press, Cambridge, 1995.

[11] L. Perko. *Differential Equations and Dynamical Systems* vol. 7 of *Texts in Applied Mathematics.* Springer, New York, 1996.

[12] R. L. Devaney. *An Introduction to Chaotic Dynamical Systems.* Addison-Wesley Publishing Company, New York, 1989.

[13] A. J. Lichtenberg and M. A. Lieberman. *Regular and Stochastic Motion* vol. 38 of *Applied Mathematical Sciences.* Springer, New York 1983.

[14] J. Guckenheimer and P. Holmes. *Nonlinear Oscillations, Dynamical Systems, and Bifurcations of Vector Fields* vol. 42 of *Applied Mathematical Sciences.* Springer, New York, 1983.

[15] G. L. Baker and J. P. Gollub. *Chaotic Dynamics.* Cambridge University Press, Cambridge, 1996.

[16] C. Robinson. *Dynamical Systems.* CRC Press, Inc., Boca Raton, Florida, 1995.

[17] * M. Brack and R. K. Bhaduri. *Semiclassical Physics.* Frontiers in Physics. Addison Wesley, New York, 1997.

[18] M. Tabor. *Chaos and Integrability in Nonlinear Dynamics.* John Wiley & Sons, Inc., New York, 1989.

[19] P. Plaschko and K. Brod. *Nichtlineare Dynamik, Bifurkation und Chaotische Systeme.* Vieweg & Sohn, Braunschweig/Wiesbaden, 1995.

[20] A. H. Nayfeh and B. Balachandran. *Applied Nonlinear Dynamics.* John Wiley & Sons, Inc., New York, 1995.

[21] A. M. O. de Almeida. *Hamiltonian Systems: Chaos and Quantization.* Cambridge University Press, Cambridge, 1988.

[22] A. Katok and B. Hasselblatt. *Modern Theory of Dynamical Systems.* Cambridge University Press, Cambridge, MA, 1995.

[23] Y. S. Sinai. *Topics in Ergodic Theory.* Princeton University Press, Princeton, NJ, 1994.

[24] S. Smale. Differentiable dynamical systems. *Bull. Am. Math. Soc.* **73** (1967) 747.

[25] R. Bowen. *Equilibrium states and the ergodic theory of Anosov diffeomorphisms.* Springer Lecture Notes in Math. 470. Springer, Heidelberg, 1975.

[26] Y. S. Sinai. Gibbs measures in ergodic theory. *Russ. Math. Surveys* **166** (1972) 21.

[27] M. Hénon. A two-dimensional mapping with a strange attractor. *Comm. Math. Phys.* **50** (1976) 69.

[28] H. Poincaré. *Les méthodes nouvelles da la méchanique céleste.* Guthier-Villars, Paris, 1892.

[29] E. N. Lorenz. *J. Atmos. Sci.* **20** (1963) 130.

[30] P. Cvitanović, Ed. *Universality in Chaos* 2nd ed. Adam Hilger, Bristol, 1989.

[31] B.-L. Hao. *Chaos.* World Scientific, Singapore, 1984.

[32] C. Mira, Ed. *Chaotic Dynamics - From one dimensional endomorphism to two dimensional diffeomorphism.* World Scientific, Singapore, 1987.

[33] C. Sparrow. *The Lorenz Equations: Bifurcations, Chaos and Strange Attractors.* Springer, New York, 1982.

[34] P. Collet and J. P. Eckmann. *Iterated Maps on the Interval as Dynamical Systems.* Birkhäuser, Cambridge, MA, 1980.

[35] J. Milnor and W. Thurston. On iterated maps of the interval. In *Dynamical Systems, U. of Maryland 1986-87*, A. Dold and B. Eckmann, Eds. vol. 1342 of *Lecture Notes in Mathematics.* Springer, Berlin, 1988 p. 465.

[36] A. Wolf, J. B. Swift, et al. Determining Lyapunov Exponents from a Time series. *Physica D* **16** (1985) 285.

[37] J. P. Eckmann, S. O. Kamphorst, et al. Lyapunov exponents from time series. *Phys. Rev. A* **34** (1986) 4971.

[38] V. I. Arnold. Instability of dynamical systems with several degrees of freedom. *Sov. Math. Docl.* **5** (1964) 581.

[39] J. Barrow-Green. *Poincaré and the Three Body Problem.* American Math. Soc., Providence R.L., 1997.

[40] F. Diracu and P. Holmes. *Celestial Encounters, The Origin of Chaos and Stability.* Princeton Univ. Press, Princeton NJ, 1996.

[41] * R. Artuso, E. Aurell, and P. Cvitanović. Recycling of strange sets: I. Cycle expansions. *Nonlinearity* **3** (1990) 325.

[42] * R. Artuso, E. Aurell, and P. Cvitanović. Recycling of strange sets: II. Applications. *Nonlinearity* **3** (1990) 361.

[43] * P. Cvitanović, R. Artuso, R. Mainieri, G. Tanner, and G. Vattay, Eds. *Classical and Quantum Chaos.* Niels Bohr Institute, Copenhagen, 2001. www.nbi.dk/ChaosBook/.

[44] P. Gaspard. *Chaos, Scattering and Statistical Mechanics.* Cambridge University Press, Cambridge, 1997.

[45] D. Wintgen. Quantisiertes Chaos. *Phys. Blätter* **49** (1990) 641.

[46] M. V. Berry. Quantum chaology, not quantum chaos. *Physica Scripta* **40** (1989) 335.

[47] R. Blümel and W. Reinhard. *Chaos in Atomic Physics.* Cambridge Monographs on atomic, Molecular and Chemical Physics. Cambridge University Press, Cambridge, 1997.

[48] F. J. Dyson. Statistical theory of the energy levels of complex systems I. *J. Math. Phys.* **3** (1962) 140.

[49] F. J. Dyson. Statistical theory of the energy levels of complex systems II. *J. Math. Phys.* **3** (1962) 157.

[50] F. Dyson. Statistical theory of the energy levels of complex systems III. *J. Math. Phys.* **3** (1962) 166.

[51] P. Pechukas. Distribution of energy eigenvalues in the irregular spectrum. *Phys. Rev. Lett.* **51** (1983) 943.

[52] T. Yukawa. New approach to the statistical properties of energy levels. *Phys. Rev. Lett.* **54** (1985) 1883.

[53] M. L. Mehta. *Random Matrices.* Academic Press, Boston, 1991.

[54] F. Haake. *Quantum Signatures of Chaos.* Springer, New York, 1991.

[55] A. Bohr and B. R. Mottelson. *Nuclear Structure.* W.A. Benjamin, New York, 1969.

[56] N. Rosenzweig and C. E. Porter. Repulsion of energy levels. *Phys. Rev.* **120** (1960) 1698.

[57] H. J. Stöckmann and J. Stein. "Quantum" chaos in billiards studied by microwave absorption. *Phys. Rev. Lett.* **64** (1990) 2215.

[58] R. L. Weaver. Spectral statistics in elastodynamics. *J. Acoust. Soc. Am.* **85** (1989) 1005.

[59] O. Bohigas, O. Legrand, C. Schmit, and D. Sornette. Comment on spectral statistics in elastodynamics. *J. Acoust. Soc. Am.* **89** (1991) 1456.

[60] R. Blümel and W. P. Reinhard. Where is the chaos in two-electron atoms? In *Quantum-Nonintegrability*, D. Feng and J.-M.Yuan, Eds. Cambridge University Press, Cambridge, 1997.

[61] G. Casati, B. V. Chirikov, I. Guarneri, and D. L. Shepelyansky. Relevance of classical chaos in quantum mechanics: The hydrogen atom in a monochromatic field. *Phys. Rep.* **52** (1987) 263.

[62] * H. Friedrich and D. Wintgen. The hydrogen atom in a uniform magnetic field-an example of chaos. *Phys. Rep.* **183** (1989) 37.

[63] M. C. Gutzwiller. Periodic orbits and classical quantization conditions. *J. Mat. Phys.* **12** (1971) 343.

[64] A. Selberg. Harmonic analysis and discontinous groups in weakly symmetric Riemannian spaces with applications to Dirichlet series. *J. Ind. Math. Soc.* **20** (1956) 47.

[65] H. P. McKean. Selberg's trace formula as applied to a compact Riemann surface. *Comm. Pure Appl. Math.* **25** (1972) 225.

[66] L. E. Reichl. *The Transition to Chaos in Conservative Classical Systems: Quantum Manifestations.* Springer, New York, 1992.

[67] W. H. Miller. Semiclassical quantisation of nonseparable systems: A new look at periodic orbit theory. *J. Chem. Phys.* **63** (1987) 996.

[68] M. V. Berry. Semiclassical mechanics of regular and irregular motion. In *Chaotic Behaviour in Deterministic Systems* (Amsterdam,, 1983) G. Iooss, R. Helleman, and R. Stora, Eds. North Holland Publ. Co,.

[69] P. Cvitanović, C. P. Dettmann, R. Mainieri, and G. Vattay. Trace formulae for stochastic evolution operators: Weak noise perturbation theory. *Journal of Statistical Physics* **93** (1998) 981.

[70] P. Cvitanović, C. P. Dettmann, R. Mainieri, and G. Vattay. Trace formulae for stochastic evolution operators: Smooth conjugation method. *Nonlinearity* **12** (1999) 939.

[71] I. Kornfeld, S. Fomin, and Y. Sinai, Eds. *Ergodic Theory.* Springer, New York, 1982.

[72] I. Kornfeld, S. Fomin, and Y. Sinai. An introduction to ergodic theory. In *Springer Graduate Texts in Math.* vol. 79. Springer, New York, 1982.

[73] M. Denker, C. Grillenberger, and K. Sigmund. *Ergodic theory on compact spaces* vol. 470 of *Springer Lecture Notes in Math.* Springer, New York, 1975.

[74] K. Peterson, Ed. *Ergodic Theory.* Cambridge Univ. Press, Cambridge, 1983.

[75] P. Walters, Ed. *An introduction to ergodic theory.* Springer, New York, 1998.

[76] D. Ruelle. *Comm. Math. Phys.* **9** (1968) 267.

[77] G. Froyland. Extracting dynamical behaviour via markov models. In *Nonlinear Dynamics and Statistics: Proceedings 1998* (2000) A. Mees, Ed. Birkhauser,.

[78] P. Cvitanović and B. Eckhardt. Periodic orbit expansions for classical smooth flows. *Journal of Physics A* **24** (1991) L237.

[79] V. Baladi and D. Ruelle. *Ergodic Theory Dynamical Systems* **14** (1994) 621.

[80] M. Pollicott. A note on the Artuso-Aurell-Cvitanović approach to the Feigenbaum tangent operator. *J. Stat. Phys.* **62** (1991) 257.

[81] V. Baladi. A brief introduction to dynamical zeta functions. In *DMV-Seminar 27, Classical Nonintegrability, Quantum Chaos* (1997) A. Knauf and Y. Sinai, Eds. Birkhauser,.

[82] M. Pollicott. Periodic orbits and zeta functions. In *AMS Summer Institute on Smooth ergodic theory and applications* (1999) A. Knauf and Y. Sinai, Eds. DMV-Seminar 27, Classical Nonintegrability, Quantum Chaos Proc. Symposia Pure Applied Math., AMS.

[83] D. Ruelle. *Statistical Mechanics, Thermodynamic formalism.* Addison-Wesley, Reading, MA, 1978.

[84] D. Ruelle. Functional determinants related to dynamical systems and the thermodynamic formalism. IHES/P/95/30 Bures sur Yvette, F March 1995. Preprint,.

[85] W. Parry and M. Pollicott. *Zeta Functions and the periodic Structure of Hyperbolic Dynamics, Astérisque 187-188.* Société Mathématique de France, Paris, 1990.

[86] V. Baladi. Dynamical zeta functions. In *Real and Complex Dynamical Systems*, B. Branner and P. Hjorth, Eds. Kluwer, Dordrecht, 1995.

[87] V. Baladi. *Positive Transfer Operators and Decay of Correlations.* World Scientific, Singapore, 2000.

[88] R. Dorfman. *From Molecular Chaos to Dynamical Chaos.* Cambridge University Press, Cambridge, 1998.

[89] D. J. Driebe. *Fully Chaotic Map and Broken Time Symmetry.* Kluwer, Dordrecht, 1999.

[90] J. Bricmont. Science of Chaos or Chaos in Science? *Physicalia Magazine* **17** (1995) 159.

[91] V. I. Arnold. *Mathematical Methods in Classical Mechanics.* Springer, Berlin, 1978.

[92] A. M. O. de Almeida. *Hamiltonian Systems: Chaos and Quantization.* Cambridge University Press, Cambridge, 1988.

[93] S. J. Schiff et al. Controlling chaos in the brain. *Nature* **370** (1994) 615.

[94] A. Salomaa, Ed. *Formal Languages.* Academic Press, San Diego, 1973.

[95] J. E. Hopcroft and J. D. Ullman, Eds. *Introduction to Automata Theory, Languages and Computation.* Addison-Wesley, Reading, Ma, 1979.

[96] D. M. Cvektović, M. Doob, and H. Sachs, Eds. *Spectra of Graphs.* Academic Press, New York, 1980.

[97] A. Weil. Numbers of solutions of equations in finite fields. *Bull. Am. Math. Soc.* **55** (1949) 497.

[98] S. Smale. *Ann. Math.* **74** (1961) 199.

[99] J. Guckenheimer. *Invent. Math.* **39** (1977) 165.

[100] A. Manning. *Bull. London Math. Soc.* **3** (1971) 215.

[101] M. Artin and B. Mazur. *Ann. Math.* **81** (1965) 82.

[102] A. Voros. Spectral zeta functions. In *Zeta Functions in Geometry (Proceedings, Tokyo 1990)* (2000) N. Kurokawa and T. Sunada, Eds. vol. 21 of *Advanced Studies in Pure Mathematics* Math. Soc. Japan, Birkhauser,.

[103] N. E. Hurt. Zeta functions and periodic orbit theory: A review. *Results in Mathematics* **23** (1993) 55.

[104] D. Fried. Lefschetz formula for flows. *Contemp. Math.* **23** (1993) 55. The Lefschetz centennial conference.

[105] F. Hofbauer and G. Keller. Ergodic properties of invariant measures for piecewise monotonic transformations. *Math. Z.* **180** (1982) 119.

[106] F. Hofbauer and G. Keller. Zeta-functions and transfer operators for piecewise linear transformations. *J. reine angew. Math.* **352** (1984) 100.

[107] G. Keller. On the rate of convergence to equilibrium in one-dimensional systems. *Comm. Math. Phys.* **96** (1984) 181.

[108] V. Baladi and G. Keller. Zeta functions and transfer operators for piecewise monotone transformations. *Comm. Math. Phys.* **127** (1990) 459.

[109] M. V. Berry. Riemann's zeta function: A model for quantum chaos? In *Quantum Chaos and Statistical Nuclear Physics*, T. Seligman and H. Nishioka, Eds. Springer, Berlin, 1986.

[110] J. Keating. The Riemann zeta function and quantum chaology. In *Quantum Chaos*, G. Casati, I. Guarneri, and U. Smilansky, Eds. North-Holland, Amsterdam, 1993.

[111] E. B. Bogomolny and P. Leboeuf. Statistical properties of the zeros of zeta functions - beyond the Riemann case. *Nonlinearity* **7** (1994) 1155.

[112] A. N. Kolmogorov and S. V. Fomin, Eds. *Elements of the theory of functions and functional analysis.* Dover, 1989.

[113] R. G. Douglas, Ed. *Banach algebra techniques in operator theory.* Springer, New York, 1998.

[114] A. Grothendieck. La Théorie de Fredholm. *Bull. Soc. Math. France* **84** (1956) 319.

[115] D. Ruelle. *Inv. Math.* **34** (1976) 231.

[116] J. Plemelj. Zur Theorie der Fredholmschen Funktionalgleichung. *Monat. Math. Phys.* **15** (1909) 93.

[117] F. Smithies. The Fredholm theory of integral equations. *Duke Math.* **8** (1941) 107.

[118] D. Fried. *Ann. Scient. Éc. Norm. Sup.* **19** (1986) 49.

[119] H. H. Rugh. The correlation spectrum for hyperbolic analytic maps. *Nonlinearity* **5** (1992) 1237.

[120] W. Brenig. *Statistische Theorie der Wärme.* Springer, Berlin, 1975.

[121] D. Wintgen. Semiclassical path-integral quantization of nonintegrable Hamiltonian systems. *Phys. Rev. Lett.* **63** (1988) 1803.

[122] G. S. Ezra, K. Richter, G. Tanner, and D. Wintgen. Semiclassical cycle expansion for the helium atom. *J. Phys. B* **24** (1991) L413.

[123] D. Wintgen, K. Richter, and G. Tanner. The semi-classical helium atom. In *Quantum Chaos*, G. Casati, I. Guarneri, and U. Smilansky, Eds. North Holland, Amsterdam, 1993.

[124] W. R. S. Garton and F. S. Tomkins. Diamagnetic Zeeman effect and magnetic configuration mixing in long spectral series of BaI. *Astrophysical J.* **158** (1969) 839.

[125] A. Holle, J. Main, G. Wiebusch, H. Rottke, and K. H. Welge. Quasi-landau spectrum of the chaotic diamagnetic hydrogen atom. In *Atoms in Strong Fields* (New York, 1990) C. A. Nicolaides, C. W. Clark, and M. Nayfeh, Eds. Plenum Press,.

[126] B. Hüpper, J. Main, and G. Wunner. Photoabsorption of nonhydrogenic Rydberg atoms in a magnetic field: Effects of core-scattered classical orbits. *Phys. Rev. Lett.* **74** (1995) 744.

[127] H. Friedrich and B. Eckhardt. *Classical, Semiclassical and Quantum Dynamics in Atoms*. Lecture Notes in Physics. Springer, Berlin, 1997.

[128] P. F. O'Mahoney. Quasi-Landau modulations in nonhydrogenic systems in a magnetic field. *Phys. Rev. Lett.* **63** (1989) 2653.

[129] P. A. Dando, T. S. Monteiro, D. Delande, and K. T. Taylor. Beyond periodic orbits: An example in nonhydrogenic atoms. *Phys. Rev. Lett.* **74** (1995) 1099.

[130] J. Main. Semiclassical approaches to atoms in external fields. In *Classical, Semiclassical and Quantum Dynamics in Atoms*, H. Friedrich and B. Eckhardt, Eds. vol. 485 of *Lecture Notes in Physics,*. Springer, Berlin, Heidelberg 1997.

[131] J. von Milczewski and T. Uzer. Canonical perturbation treatment of a Rydberg electron in combined electric and magnetic fields. *Phys. Rev. A* **56** (1997) 220.

[132] J. Main, M. Schwacke, and G. Wunner. Hydrogen atom in combined electric and magnetic fields with arbitrary mutual orientations. *Phys. Rev. A* **57** (1998) 1149.

[133] P. Cvitanović. Invariant measurement of strange sets in terms of cycles. *Phys. Rev. Lett.* **61** (1988) 2729.

[134] S. Grossmann and S. Thomae. Invariant distributions and stationary correlation functions of one-dimensional discrete processes. *Z. Naturforsch. A* **32** (1977) 1353.

[135] B. Eckhardt and G. Russberg. Resummation of classical and semiclassical periodic-orbit formulas. *Phys. Rev. E* **47** (1993) 1578.

[136] F. Christiansen, G. Paladin, and H. H. Rugh. Determination of correlation spectra in chaotic systems. *Phys. Rev. Lett.* **65** (1990) 2087.

[137] C. Grebogi, E. Ott, and J. A. Yorke. Unstable periodic orbits and the dimensions of multifractal chaotic attractors. *Phys. Rev. A* **37** (1988) 1711.

[138] D. Auerbach, P. Cvitanović, J. P. Eckmann, G. H. Gunaratne, and I. Procaccia. Exploring chaotic motion through periodic orbits. *Phys. Rev. Lett.* **58** (1987) 2387.

[139] E. Ott, T. Sauer, and J. A. Yorke. Lyapunov partition functions for the dimensions of chaotic sets. *Phys. Rev. A* **39** (1989) 4212.

[140] D. P. Lathrop and E. J. Kostelich. Characterization of an experimental strange attractor by periodic orbits. *Phys. Rev. A* **40** (1989) 4028.

[141] P. Cvitanović and B. Eckhardt. Periodic-orbit quantization of chaotic system. *Phys. Rev. Lett.* **63** (1989) 823.

[142] D. Ruelle. Statistical mechanics of a one-dimensional lattice gas. *Commun. Math. Phys.* **29** (1968) 267.

[143] H. H. Rugh. *Time evolution and corrections in chaotic dynamical systems.* PhD thesis Niels Bohr Institute 1992.

[144] B. Eckhardt. Fractal properties of scattering singularities. *J. Phys. A* **20** (1987) 5971.

[145] P. Gaspard and S. A. Rice. Scattering from a classically chaotic repellor. *J. Chem. Phys.* **90** (1989) 2225.

[146] P. Gaspard and S. A. Rice. Semiclassical quantization of the scattering from a classically chaotic repellor. *J. Chem. Phys.* **90** (1989) 2245.

[147] P. Gaspard and D. Alonso Ramirez. Ruelle classical resonances and dynamical chaos: The three- and four-disk scatterers. *Physical Review E* **45** (1992) 8383.

[148] R. Artuso. Diffusive dynamics and periodic orbits of dynamical systems. *Phys. Lett. A* **160** (1991) 528.

[149] W. N. Vance. Unstable periodic orbits and transport properties of nonequilibrium steady states. *Phys. Rev. Lett.* **96** (1992) 1356.

[150] P. Cvitanović, J. P. Eckman, and P. Gaspard. Transport properties of the lorentz gas in terms of periodic orbits. *Chaos, Solitons and Fractals* **6** (1995) 113.

[151] * R. Klages. *Deterministic diffusion in one-dimensional chaotic dynamical systems.* Wissenschaft & Technik Verlag, Berlin, 1996.

[152] R. Klages and J. R. Dorfman. Simple maps with fractal diffusion coefficients. *Phys. Rev. Lett.* **74** (1995) 387.

[153] R. Klages and J. R. Dorfman. Simple deterministic dynamical systems with fractal diffusion coefficients. *Phys. Rev. E* **59** (1999) 5361.

[154] T. Geisel and J. Nierwetberg. Onset of diffusion and universal scaling in chaotic systems. *Phys. Rev. Lett.* **48** (1982) 7.

[155] R. Artuso, G. Casati, and R. Lombardi. Periodic orbit theory of anomalous diffusion. *Phys. Rev. Lett.* **71** (1993) 62.

[156] M. Schell, S. Fraser, and R. Kapral. Diffusive dynamics in systems with translational symmetry: A one-dimensional-map model. *Phys. Rev. A* **26** (1982) 504.

[157] S. Grossmann and H. Fujisaka. Diffusion in discrete nonlinear dynamical systems. *Phys. Rev. A* **26** (1982) 1779.

[158] H. Fujisaka and S. Grossmann. Chaos-induced diffusion in nonlinear discrete dynamics. *Cond. Matt.* **48** (1982) 261.

[159] M. Mareschal and B. Holian, Eds. *Microscopic simulations of Complex Hydrodynamic Phenomena* (New York, 1992) Plenum,.

[160] P. Manneville and Y. Pomeau. Intermittency and the Lorenz model. *Phys. Lett. A* **75** (1979) 1.

[161] P. Manneville and Y. Pomeau. Intermittent transition to turbulence in dissipative dynamical systems. *Comm. Math. Phys.* **74** (1980) 189.

[162] F. Christiansen, P. Cvitanović, and V. Putkaradze. Spatiotemporal chaos in terms of unstable recurrent patterns. *Nonlinearity* **10** (1997) 55.

[163] Y. Kuramoto and T. Tsuzuki. Persistent propagation of concentration waves in dissipative media far from thermal equilibrium. *Prog. Theor. Phys.* **55** (1976) 365.

[164] G. I. Sivashinsky. Nonlinear analysis of hydrodynamical instability in laminar flames - I. Derivation of basic equations. *Acta Astr.* **4** (1977) 1177.

[165] C. Foias, B. Nikolaenko, G. R. Sell, and R. Témann. Kuramoto-Sivashinsky equation. *J. Math. Pures et Appl.* **67** (1988) 197.

[166] I. G. Kevrekidis, B. Nicolaenko, and J. C. Scovel. Back in the saddle again: A computer assisted study of the Kuramoto-Sivashinsky equation. *SIAM J. Applied Math.* **50** (1990) 760.

[167] I. Schwartz and I. Triandaf. Tracking unstable orbits in experiments. *Phys. Rev. A* **46** (1992) 7439.

[168] H. D. I. Abarbanel, R. Brown, J. J. Sidorowich, and L. S. Tsimring. The analysis of observed chaotic data in physical systems. *Rev. Mod. Phys.* **65** (1993) 1331.

[169] R. Badii, E. Brun, M. Finardi, L. Flepp, R. Holzner, J. Parisi, C. Reyl, and J. Simonet. Progress in the analysis of experimental chaos through periodic orbits. *Rev. Mod. Phys.* **66** (1994) 1389.

[170] P. So, E. Ott, S. J. Schiff, D. T. Kaplan, T. Sauer, and C. Grebogi. Detecting unstable periodic orbits in chaotic experimental data. *Phys. Rev. Lett.* **76** (1996) 4705.

[171] P. So, E. Ott, T. Sauer, B. J. Gluckman, C. Grebogi, and S. J. Schiff. Extracting unstable periodic orbits from chaotic time series data. *Phys. Rev. E* **55** (1997) 5398.

[172] P. Grassberger, H. Kantz, and U. Moenig. On the symbolic dynamics of the Hénon map. *J. Phys. A* **22** (1989) 5217.

[173] O. Biham and M. Kvale. Unstable periodic orbits in the stadium billiard. *Phys. Rev. A* **46** (1992) 6334.

[174] C. P. Dettmann and G. P. Morriss. Stability ordering of cycle expansions. *Phys. Rev. Lett.* **78** (1997) 4201.

[175] C. P. Dettmann and P. Cvitanović. Cycle expansions for intermittent diffusion. *Phys. Rev. E* **56** (1997) 6687.

[176] P. Dahlqvist and G. Russberg. Periodic orbit quantisation of bound chaotic systems. *Journal of Physics A* **24** (1991) 4763.

[177] D. Pierson and F. Moss. Detecting periodic unstable points in noisy chaotic and limit cycle attractors with applications to biology. *Phys. Rev. Lett.* **75** (1995) 2124.

[178] T. Kaplan. Applying blind chaos control to find periodic orbits. unpublished, 1999.

[179] Y. C. Hsiao and P. C. Tung. Controlling chaos for nonautonomous systems by detecting unstable periodic orbits. *Chaos, Solitons and Fractals* **13** (2002) 1043.

[180] Y. L. Bolotin, V. Y. Gonchar, A. A. Krokhin, A. Tur, and V. V. Yanovsky. Control of unstable high-period orbits in complex systems. *Phys. Rev. Lett.* **82** (1999) 2504.

[181] Y. C. Lai, M. Ding, and C. Grebogi. Controlling Hamiltonian chaos. *Phys. Rev. E* **47** (1993) 86.

[182] Y. C. Lai, T. Tél, and C. Grebogi. Stabilizing chaotic-scattering trajectories using control. *Phys. Rev. E* **48** (1993) 709.

[183] S. Boccaletti, C. Grebogi, Y. C. Lai, H. Mancini, and D. Maza. The control of chaos: Theory and applications. *Physics Reports* **329** (2000) 103.

[184] * E. Ott, C. Grebogi, and J. A. Yorke. Controlling chaos. *Phys. Rev. Lett.* **64** (1990) 1196.

[185] L. J. Dubé and P. Després. The control of dynamical systems: Recovering order from chaos. In *AIP Conference Proceedings* (2000) vol. 500 p. 551. Physics of Electronic and Atomic Collisions. XXI International Conference, Sendai, Japan, 22-27 July 1999.

[186] B. Doyon and L. J. Dubé. Targeting unknown and unstable periodic orbits. *Phys. Rev. E* **65** (2002) 037202/1–4.

[187] A. Hübler and E. Lüscher. Resonant Stimulation and Control of Nonlinear Oscillators. *Naturwissenschaften* **76** (1989) 67.

[188] Y. Braiman and I. Goldhirsch. Taming chaotic dynamics with weak periodic perturbations. *Phys. Rev. Lett.* **66** (1991) 2545.

[189] R. Lima and M. Pettini. Suppression of chaos by resonant parametric perturbations. *Phys. Rev. E* **41** (1990) 726.

[190] R. Chacon and J. Diaz Bejarano. Routes to suppressing chaos by weak periodic perturbations. *Phys. Rev. Lett.* **71** (1993) 3103.

[191] Y. Kivshar, F. Rodelsperger, and H. Benner. Suppression of chaos by nonresonant parametric perturbations. *Phys. Rev. E* **49** (1994) 319.

[192] W. L. Ditto, S. N. Rauseo, and M. L. Spano. Experimental control of chaos. *Phys. Rev. Lett.* **65** (1990) 3211.

[193] G. Nitsche and U. Dressler. Controlling chaos using time delay coordinates. *Phys. Rev. Lett.* **68** (1992) 1.

[194] R. W. Rollins, P. Parmananda, and P. Sherard. Controlling chaos in highly dissipative systems: A simple recursive algorithm. *Phys. Rev. E* **47** (1993) R780.

[195] D. Auerbach, C. Grebogi, E. Ott, and J. A. Yorke. Controlling chaos in high dimensional systems. *Phys. Rev. Lett.* **69** (1992) 3479.

[196] T. Tel. Controlling transient chaos. *Journal of Physics A* **24** (1991) L1359.

[197] T. Shinbrot, E. Ott, C. Grebogi, and J. A. Yorke. Using chaos to direct trajectories to targets. *Phys. Rev. Lett.* **65** (1990) 3215.

[198] * K. Pyragas. Continuous control of chaos by self-controlling feedback. *Phys. Lett. A* **170** (1992) 421.

[199] K. Pyragas. Stabilization of unstable periodic and aperiodic orbits of chaotic systems by self-controlling feedback. *Zeitschrift für Naturforschung A* **48** (1993) 629.

[200] K. Pyragas. Predictable chaos in slightly perturbed unpredictable chaotic systems. *Phys. Lett. A* **181** (1993) 203.

[201] A. Kittel, K. Pyragas, and R. Richter. Prerecorded history of a system as an experimental tool to control chaos. *Phys. Rev. E* **50** (1994) 262.

[202] D. J. Gauthier, D. W. Sukow, H. M. Concannon, and J. E. S. Socolar. Stabilizing unstable periodic orbits in a fast diode resonator using continuous time-delay autosynchronization. *Phys. Rev. E* **50** (1994) 2343.

[203] J. E. S. Socolar, D. W. Sukow, and D. J. Gauthier. Stabilizing unstable periodic orbits in fast dynamical systems. *Phys. Rev. E* **50** (1994) 3245.

[204] E. Ott, C. Grebogi, and J. A. Yorke. Controlling chaotic dynamical systems. In *CHAOS: Soviet-American Perspectives on Nonlinear Science*, D. Campbell, Ed. American Institute of Physics, New-York, 1990 p. 153.

[205] T. Shinbrot, C. Grebogi, E. Ott, and J. A. Yorke. Using small perturbations to control chaos. *Nature* **363** (1993) 411.

[206] E. J. Kostelich, C. Grebogi, E. Ott, and J. A. Yorke. Higher dimensional targeting. *Phys. Rev. E* **47** (1993) 305.

[207] E. R. Hunt. Stabilizing high-period orbits in a chaotic system: The diode resonator. *Phys. Rev. Lett.* **67** (1991) 1953.

[208] Y. Liu and J. Ohtsubo. Experimental control of chaos in a laser-diode interferometer with delayed feedback. *Optics Letters* **19** (1994) 448.

[209] G. A. Johnson and E. R. Hunt. Controlling chaos in a simple autonomous system: Chua's circuit. *International Journal of Bifurcation and Chaos* **3** (1993) 789.

[210] B. Peng, V. Petrov, and K. Showalter. Controlling chemical chaos. *J. Chem. Phys.* **95** (1992) 4957.

[211] V. Petrov, B. Peng, and K. Showalter. A map-based algorithm for controlling low-dimensional chaos. *J. Chem. Phys.* **96** (1992) 7506.

[212] V. Petrov, V. Gaspar, J. Masere, and K. Showalter. Controlling chaos in the Belousov-Zhabotinsky reaction. *Nature* **361** (1993) 240.

[213] R. Roy, T. W. Murphy, T. D. Maier, Z. Gills, and E. R. Hunt. Dynamical control of a chaotic laser: Experimental stabilisation of a globally coupled system. *Phys. Rev. Lett.* **68** (1992) 1259.

[214] C. Reyl, L. Flepp, R. Badii, and E. Brun. Control of NMR-laser chaos in high-dimensional embedding space. *Phys. Rev. E* **47** (1993) 267.

[215] S. Bielawski, M. B. M, D. Derozier, and P. Glorieux. Stabilization and characterization of unstable steady states in a laser. *Phys. Rev. A* **47** (1993) 3276.

[216] J. Singer, Y.-Z. Wang, and H. H. Bau. Controlling a chaotic system. *Phys. Rev. Lett.* **66** (1991) 1123.

[217] A. Azevedo and S. M. Rezende. Controlling chaos in spin-wave instabilities. *Phys. Rev. Lett.* (1991) 1342.

[218] A. Garfinkel, M. L. Spano, W. L. Ditto, and J. N. Weiss. Controlling cardiac chaos. *Science* **257** (1992) 1230.

[219] T. Shinbrot. Chaos: Unpredictable yet controllable? *Nonlinear Science Today* **3** (1993) 1.

[220] W. L. Ditto and L. M. Pecora. Mastering chaos. *Scientific American (International Edition)* **269** (1993) 62.

[221] G. Chen and X. Dong. *International Journal of Bifurcation and Chaos* **3** (1993) 1363.

[222] K. Pyragas and A. Tamasevicius. Experimental control of chaos by delayed self-controlling feedback. *Phys. Lett. A* **180** (1993) 99.

[223] K. Pyragas. Control of chaos via extended delay feedback. *Phys. Lett. A* **206** (1995) 323.

[224] A. Kittel, J. Parisi, and K. Pyragas. Delayed feedback control of chaos by self-adapted delay time. *Phys. Lett. A* **198** (1995) 433.

[225] A. Kittel, J. Parisi, K. Pyragas, and R. Richter. Delayed feedback control of chaos in an electronic double-scroll oscillator. *Zeitschrift für Naturforschung A* **49** (1994) 843.

[226] A. Kittel, M. Popp, J. Parisi, and K. Pyragas. *Control of chaos by self-adapted delayed feedback.* Nonlinear physics of complex systems. Current status and future trends. Springer, Berlin, Germany, 1996.

[227] M. de Sousa Vieira and A. J. Lichtenberg. Controlling chaos using nonlinear feedback with delay. *Phys. Rev. E* **54** (1996) 1200.

[228] K. Pyragas, F. Lange, T. Letz, J. Parisi, and A. Kittel. Stabilization of an unstable steady state in intracavity frequency-doubled lasers. *Phys. Rev. E* **61** (2000) 3721.

[229] S. Bielawski, D. Derozier, and P. Glorieux. Controlling unstable periodic orbits by a delayed continuous feedback. *Phys. Rev. E* **49** (1994) R971.

[230] W. Just, J. Möckel, D. Reckwerth, E. Reibold, and H. Benner. Delayed feedback control of periodic orbits in autonomous systems. *Phys. Rev. Lett.* **81** (1998) 62.

[231] W. Just, E. Reibold, H. Benner, K. Kacperski, P. Fronczak, and J. Holyst. Limits of time-delayed feedback control. *Phys. Lett. A* **254** (1999) 158.

[232] W. Just, E. Reibold, K. Kacperski, K. Kacperski, P. Fronczak, J. Holyst, and H. Benner. Influence of stable Floquet exponents on time-delayed feedback control. *Phys. Rev. E* **61** (2000) 5045.

[233] W. Just, T. Bernard, M. Ostheimer, E. Reibold, and H. Benner. Mechanism of time-delayed feedback control. *Phys. Rev. Lett.* **78** (1997) 203.

[234] X. Yu and Y. Xia. Detecting unstable periodic orbits in Chen's chaotic attractor. *International Journal of Bifurcation and Chaos* **10** (2000) 1987.

[235] H. G. Schuster and M. B. Stemmler. Control of chaos by oscillating feedback. *Phys. Rev. E* **56** (1997) 6410.

[236] X. Yu. Controlling Lorenz chaos. *International Journal of Bifurcation and Chaos* **27** (1999) 355.

[237] * W. H. Press, S. A. Teukolsky, W. T. Vetterling, and B. P. Flannery. *Numerical recipes in FORTRAN: The Art of Scientific Computing.* Cambridge University Press, Cambridge, MA, 1992.

[238] C. J. F. Ridders. A new algorithm for computing a single root of a real continuous function. *IEEE Transactions on Circuits & Systems* **CAS-26** (1979) 979.

[239] R. P. Brent. *Algorithms for Minimization without Derivatives.* Prentice–Hall, Englewood Cliffs, NJ, 1973 ch. 3, 4.

[240] L. Drossos, O. Ragos, M. N. Vrahatis, and T. Bountis. Method for computing long periodic orbits of dynamical systems. *Phys. Rev. E* **53** (1996) 1206.

[241] * M. N. Vrahatis. An efficient method for locating and computing periodic orbits of nonlinear mappings. *J. Comput. Phys.* **119** (1995) 105.

[242] M. N. Vrahatis, A. E. Perdiou, V. S. Kalantonis, E. A. Perdios, et al. Application of the characteristic bisection method for locating and computing periodic orbits in molecular systems. *Computer Physics Communications* **138** (2001) 53.

[243] D. J. Kavvadias and M. N. Vrahatis. Locating and computing all the simple roots and extrema of a function. *SIAM Journal on Scientific Computing* **17** (1996) 1232.

[244] M. N. Vrahatis, T. Bountis, and H. Kollmann. Periodic orbits and invariant surfaces of 4D nonlinear mappings. *International Journal of Bifurcation and Chaos* **6** (1996) 1425.

[245] A. E. Perdiou, V. S. Kalantonis, E. A. Perdios, and M. N. Vrahatis. Application of efficient composite methods for computing with certainty periodic orbits in molecular systems. *Computer Physics Communications* **148** (2002) 227.

[246] V. S. Kalantonis, E. A. Perdios, A. E. Perdiou, and M. N. Vrahatis. Computing with certainty individual members of families of periodic orbits of a given period. *Celestial Mechanics & Dynamical Astronomy* **80** (2001) 81.

[247] M. N. Vrahatis, A. E. Perdiou, V. S. Kalantonis, E. A. Perdios, K. Papadakis, R. Prosmiti, and S. C. Farantos. Application of the characteristic bisection method for locating and computing periodic orbits in molecular systems. *Computer Physics Communications* **138** (2001) 53.

[248] C. Polymilis, G. Servizi, C. Skokos, G. Turchetti, and M. N. Vrahatis. Locating periodic orbits by Topological Degree theory. *arXiv:nlin.CD/0211044 v1, 25 Nov. 2002* (2002).

[249] F. S. Acton. *Numerical Methods That Work* 2nd ed. Mathematical Assiciation of America, Washington, 1990. Chapter 5.

[250] J. Ortega and W. Rheinboldt. *Iterative Solution of Nonlinear Equations in Several Variables.* Academic Press, New York, 1970.

[251] H. Qiu. *A Robust Examination of the Newton-Raphson Method with strong Global Convergence Properties.* PhD thesis University of Central Florida 1993.

[252] I. Newton. Methodus fluxionum et serierum infinitarum (between 1664 and 1671).

[253] I. Raphson. Analysis aequationum universalis. London, 1690.

[254] L. V. Kantorovich and G. P. Akilov. *Functional Analysis in Normed Spaces.* Pergamon Press, Elmsford, New York, 1964.

[255] S. Smale. *Newton's method estimates from data in one point.* The Merging of Disciplines: New Directions in Pure, Applied and Computational Mathematics. Springer, New York, 1986.

[256] M. S. Petkovic, D. D. Herceg, and S. M. Ilic. *Point Estimation Theory and Its Applications.* Institute of Mathematics, Novi Sad, Yugoslavia, 1997.

[257] X. Wang and D. Han. On dominating sequence method in the point estimate and Smale's theorem. *Sci. Sinica Scr. A* (1989) 905.

[258] J. H. Curry. On zero finding methods of higher order from data at one point. *J. Complexity* **5** (1989) 219.

[259] M. Kim. On approximate zeros and rootfinding algorithms for a complex polynomial. *Math. Comput.* **51** (1988) 707.

[260] A. S. Householder. *The Numerical Treatment of a Single Nonlinear Function.* McGraw-Hill, New York, 1970.

[261] B. B. Mandelbrot. *The Fractal Geometry of Nature.* W. H. Freeman, San Francisco, CA, 1983.

[262] H. Peitgen and D. Saupe. *The Science of Fractal Images.* Springer, New York, NY, 1988.

[263] R. M. Dickau. Compilation of Iterative and List Operations. *Mathematica J.* **7** (1997) 14.

[264] F. Stummel and H. Hainer, Eds. *Praktische Mathematik.* Teubner, Stuttgart, 1982.

[265] C. G. Broyden. A Class of Methods for Solving Nonlinear Simultaneous Equations. *Mathematics of Computation* (1965) 577.

[266] J. E. Dennis and R. B. Schnabel. *Numerical Methods for Unconstrained Optimization and Nonlinear Equations.* Prentice-Hall, Englewood Cliffs, New York, 1983.

[267] T. P. Minka. Beyond Newton's method. Preprint 2002.

[268] M. W. Hirsch and S. Smale. On algorithms for solving $f(x) = 0$. *Commun. Pure Appl. Math.* **32** (1979) 281.

[269] P. J. Zufiria and R. S. Guttalu. A computational method for finding all the roots of a vector function. *Applied Mathematics and Computation* **35** (1990) 13.

[270] S. G. Nash. reconditioning of truncated-Newton methods. *SIAM Journal on Scientific & Statistical Computing* **6** (1985) 599.

[271] E. Kazentsev. Unstable periodic orbits and attractor of the Lorenz model. Rapport de rechereche no. 3344. Institut National de Recherche en Informatique et en Automatique, 1998.

[272] S. M. Zoldi and H. S. Greenside. Spatially localized unstable periodic orbits of a high-dimensional chaotic system. *Phys. Rev. E* **57** (1998) R2511.

[273] B. Mestel and I. Percival. Newton method for highly unstable orbits. *Physica D* **24** (1987) 172.

[274] Q. Chen, J. D. Meiss, and I. C. Percival. Orbit extension method for finding unstable orbits. *Physica D* **29** (1987) 143.

[275] K. T. R. Davies, T. E. Huston, and M. Baranger. Calculations of periodic trajectories for the Hénon-Heiles Hamilton an using the monodromy method. *Chaos* **2** (1992) 215.

[276] M. Baranger and K. T. R. Davies. Periodic trajectories for a two-dimensional nonintegrable Hamiltonian. *Annals of Physics* **177** (1987) 330.

[277] M. Baranger, K. T. R. Davies, and J. H. Mahoney. The calculation of periodic trajectories. *Annals of Physics* **186** (1988) 95.

[278] M. Baranger, M. R. Haggerty, and B. Lauritzen. Periodic orbits of nonscaling Hamiltonian systems from quantum mechanics. *Chaos* **5** (1995) 261.

[279] K. T. R. Davies. A new method for calculating classical periodic trajectories in two dimensions. *Mathematical Models & Methods in Applied Sciences* **4** (1994) 251.

[280] N. S. Simonovic. Calculations of periodic orbits: The monodromy method and application to regularized systems. *Chaos* **9** (1999) 854.

[281] D. Pingel, P. Schmelcher, and F. K. Diakonos. Analytical solutions to one-dimensional dissipative and discrete chaotic dynamics. *Phys. Rev. E* **58** (1998) 369.

[282] * O. Biham and W. Wenzel. Characterization of unstable periodic orbits in chaotic attractors and repellors. *Phys. Rev. Lett.* **63** (1989) 819.

[283] * O. Biham and W. Wenzel. Unstable periodic orbits and the symbolic dynamics of the complex Hénon map. *Phys. Rev. E* **42** (1990) 4639.

[284] M. J. Davies, R. S. MacKay, and A. Sannami. Homoclinic bifurcations for the Hénon map. *Physica D* **52** (1991) 171.

[285] W. Wenzel, O. Biham, and C. Jayaprakash. Periodic orbits in the dissipative standard map. *Phys. Rev. E* **43** (1991) 6550.

[286] B. Dey. Unstable periodic orbits and characterization of the spatial chaos in a nonlinear monatomic chain at the T=0 first-order phase-transition point. *Phys. Rev. B* **52** (1995) 220.

[287] G. D'Alessandro, P. Grassberger, S. Isola, and A. Politi. On the topology of the Hénon map. *Journal of Physics A* **23** (1990) 5285.

[288] A. Politi and A. Torcini. Towards a statistical mechanics of spatiotemporal chaos. *Phys. Rev. Lett.* **69** (1992) 3421.

[289] B. R. Hunt and E. Ott. Optimal periodic orbits of chaotic systems occur at low period. *Phys. Rev. E* **54** (1996) 328.

[290] R. T. Skodje and M. J. Davis. Statistical rate theory for transient chemical species: Classical lifetimes from periodic orbits. *Chemical Physics Letters* **175** (1990) 92.

[291] K. T. Hansen. Remarks on the symbolic dynamics for the Hénon map. *Phys. Lett. A* **165** (1992) 100.

[292] H. P. Fang. Dynamics of strongly dissipative systems. *Phys. Rev. E* **49** (1994) 5025.

[293] H. Kaplan. Type-I intermittency for the Hénon-map family. *Phys. Rev. E* **48** (1993) 1655.

[294] Y. Nagai and Y.-C. Lai. Characterization of blowout bifurcation by unstable periodic orbits. *Phys. Rev. E* **55** (1997) R1251.

[295] D. Sterling, H. R. Dullin, and J. D. Meiss. Homoclinic bifurcations for the Hénon map. *Physica D* **134** (1999) 153.

[296] D. Sterling and J. D. Meiss. Computing periodic orbits using the anti-integrable limit. *Phys. Lett. A* **241** (1998) 46.

[297] K. T. Hansen. *Symbolic Dynamics in Chaotic Systems.* PhD thesis Univ. of Oslo 1994.

[298] K. T. Hansen. Alternative method to find orbits in chaotic systems. *Phys. Rev. E* **52** (1995) 2388.

[299] Z. B. Wu and J. Y. Zeng. A method to find unstable periodic orbits for the diamagnetic kepler problem 2000.

[300] *** P. Schmelcher and F. K. Diakonos. Detecting unstable periodic orbits of chaotic dynamical systems. *Phys. Rev. Lett.* **78** (1997) 4733.

[301] *** P. Schmelcher and F. K. Diakonos. General approach to the localization of unstable periodic orbits in chaotic dynamical systems. *Phys. Rev. E* **57** (1998) 2739.

[302] *** D. Pingel, P. Schmelcher, F. K. Diakonos, and O. Biham. Theory and applications of the systematic detection of unstable periodic orbits in dynamical systems. *Phys. Rev. E* **62** (2000) 2119.

[303] *** R. L. Davidchack and Y. C. Lai. Efficient algorithm for detecting unstable periodic orbits in chaotic systems. *Phys. Rev. E* **60** (1999) 6172.

[304] *** R. L. Davidchack, Y. C. Lai, A. Klebanoff, and E. M. Bollt. Towards complete detection of unstable periodic orbits in chaotic systems. *Phys. Lett. A* **287** (2001) 99.

[305] ** A. Klebanoff and E. M. Bollt. Convergence analysis of Davidchack and Lai's algorithm for finding periodic orbits. *Chaos, Solitons and Fractals* **12** (2001) 1305.

[306] * H. Ito and A. Kumamoto. Locating fold bifurcation points using subspace shooting. *IEICE Trans. Fundamentals E* **81** (1998) 1791.

[307] * H. Ito, M. Murakita, I. Wakabayashi, and A. Kumamoto. Detecting unstable periodic orbits in chaotic systems using subspace fixed-point iteration. *Proc. Progress in Nonlinear Science, Russia* **to be published** (2001).

[308] * R. Thomas. Deterministic chaos seen in terms of feedback circuits: Analysis, synthesis, "labyrinth chaos". *International Journal of Bifurcation and Chaos* **9** (1999) 1889.

[309] *** F. K. Diakonos, P. Schmelcher, and O. Biham. Systematic computation of the least unstable periodic orbits in chaotic attractors. *Phys. Rev. Lett.* **81** (1998) 4349.

[310] K. Ikeda. Multiple-valued stationary state and its instability of the transmitted light by a ring cavity system. *Opt. Commun.* **30** (1979) 257.

[311] S. M. Hammel, C. K. R. T. Jones, and J. V. Moloney. Global dynamical behavior of the optical field in a ring cavity. *J. Opt. Soc. Am. B* **4** (1985) 552.

[312] ** F. K. Diakonos, D. Pingel, and P. Schmelcher. Analyzing Lyapunov spectra of chaotic dynamical systems. *Phys. Rev. E* **62** (2000) 4413.

[313] S. Wiggins. *Introduction to Applied Nonlinear Dynamical Systems and Chaos.* Springer, New York, 1996.

[314] R. S. Ellis. *Entropy, Large Deviations and Statistical Mechanics.* Springer, New York, 1985.

[315] H. Kantz and T. Schreiber. *Nonlinear time series analysis.* Cambridge Nonlinear Science Series 7. Cambridge University Press, Cambridge, 1997.

[316] F. Takens. Detecting strange attractors in fluid turbulence. In *Dynamical Systems and Turbulence*, D. Rand and L. S. Young, Eds. vol. 898 of *Lecture Notes in Mathematics.* Springer, New York, 1981.

[317] J. C. Roux, R. H. Simoyi, and H. L. Swinney. Observation of a strange attractor. *Physica D* **8** (1983) 257.

[318] J. P. Eckmann and D. Ruelle. Ergodic theory of chaos and strange attractors. *Rev. Mod. Phys.* **57** (1985) 617.

[319] *** D. Pingel, P. Schmelcher, and F. K. Diakonos. Detecting unstable periodic orbits in chaotic continuous-time dynamical systems. *Phys. Rev. E* **64** (2001) 026214.

[320] D. Gulick. *Encounters with Chaos.* McGraw-Hill, Inc., New York, 1992.

[321] G. Tanner, K. T. Hansen, and J. Main. The semiclassical resonance spectrum of hydrogen in a constant magnetic field. *Nonlinearity* **9** (1996) 1641.

[322] D. Wintgen and A. Hönig. Irregular wave functions of a hydrogen atom in a uniform magnetic field. *Phys. Rev. Lett.* **63** (1989) 1476.

[323] B. Eckhardt, G. Hose, and E. Pollak. Quantum mechanics of a classically chaotic system: Observations on scars, periodic orbits, and vibrational adiabaticity. *Phys. Rev. A* **39** (1989) 3776.

[324] * H. D. Meyer. Theory of the Lyapunov exponents of Hamiltonian systems and a numerical study on the transition from regular to irregular classical motion. *J. Chem. Phys.* **84** (1986) 3147.

[325] A. N. Kolmogorov. On conservation of conditionally periodic motions under small perturbations of the Hamiltonian. *Dokl. Akad. Nauk SSSR* **98** (1954) 527.

[326] V. I. Arnold. Small denominators and problems of stability of motion in classical and celestial mechanics. *Russ. Math. Surveys* **18** (1963) 85.

[327] J. Moser. *Stable and Random Motions in Dynamical Systems.* Princeton Univ. Press, Cambridge, MA, 1973.

[328] N. Bohr. *Philos. Mag.* **26** (1913) 488.

[329] I. Langmuir. *Phys. Rev.* **17** (1921) 339.

[330] J. H. V. Vleck. *Phil. Mag.* **44** (1922) 842.

[331] H. A. Kramers. *Z. Phys.* **13** (1923) 312.

[332] A. Einstein. *Verh. Dtsch. Phys. Ges.* **19** (1917) 82.

[333] J. B. Keller. *Ann. Phys. (N.Y.)* **4** (1958) 180.

[334] M. C. Gutzwiller. *J. Mat. Phys.* **8** (1967) 1979.

[335] M. C. Gutzwiller. Phase-integral approximation in momentum space and the bound states of an atom. II. *J. Mat. Phys.* **10** (1969) 1004.

[336] M. C. Gutzwiller. Energy spectrum according to classical mechanics. *J. Mat. Phys.* **11** (1970) 1791.

[337] J. G. Leopold and I. C. Perciva. The semiclassical two-electron atom and the old quantum theory. *J. Mat. Phys.* **13** (1980) 1037.

[338] M. S. Dimitrijević and P. V. Grujić. Langmuir's helium-like models revisited. *Z. Naturforsch. A* **39** (1984) 930.

[339] G. E. Wesenberg, D. W. Noid, and J. B. Delos. Re-examination of an early model of two-electron atoms. *Chem. Phys. Lett.* **118** (1985) 72.

[340] S. Watanabe. Kummer-function representation of ridge traveling waves. *Phys. Rev. A* **36** (1987) 1566.

[341] H. Klar. Equilibrium atomic structure: Rotating atoms. *Phys. Rev. Lett.* **57** (1986) 66.

[342] H. Klar. Equilibrium atomic structure: Rotating atoms. *Zeitschrift für Physik D* **3** (1986) 353.

[343] H. Klar. Novel motion in highly excited two-electron atoms. *J. Opt. Soc. Am. B* **4** (1987) 788.

[344] M. Poirier. Possible rigid rotations in two-electron atoms. *Phys. Rev. A* **40** (1989) 3498.

[345] G. Tanner, K. Richter, and J. Rost. The theory of two-electron atoms: Between ground state and complete fragmentation. *Rev. Mod. Phys.* **72** (2000) 497.

[346] * K. Richter. *Semiklassik von Zwei-Elektronen-Atomen.* PhD thesis Albert-Ludwigs-Universität Freiburg i.Br. 1991.

[347] * P. Schlagheck. *Das Drei-Körper-Coulombproblem unter periodischem Antrieb.* PhD thesis Max Planck Institut für Quantenoptik 1999.

[348] P. Schlagheck and A. Buchleitner. Nondispersive two-electron wave packets in driven helium. *Eur. Phys.* **22** (2003) 401.

[349] P. Schlagheck and A. Buchleitner. Algebraic decay of the survival probability in chaotic helium. *Phys. Rev. A* **63** (2001) 024701.

[350] P. Schlagheck and A. Buchleitner. Stable classical configurations in strongly driven helium. *Physica D* **131** (1999) 110.

[351] P. Schlagheck and A. Buchleitner. Nondispersive two-electron wave packets in the collinear driven helium atom. *Europhys. Lett.* **46** (1999) 24.

[352] P. Schlagheck and A. Buchleitner. Classical support for non-dispersive two-electron wave packets in the driven helium atom. *J. Phys. B* **31** (1998) L489.

[353] I. C. Percival. Planetary atoms. *Proc. R. Soc. Lond. A* **353** (1977) 289.

[354] J. G. Leopold and I. C. Percival. Microwave ionization and excitation of Rydberg atoms. *Phys. Rev. Lett.* **41** (1978) 944.

[355] P. Kustaanheimo and E. Stiefel. *J. Reine Angew. Math.* **218** (1965) 204.

[356] S. J. Aarseth and K. Zare. A regularization of the three-body problem. *Celest. Mech.* **10** (1974) 185.

[357] C. L. Siegel. *Ann. Math.* **42** (1941) 127.

[358] * P. Schlagheck, D. Pingel, and P. Schmelcher. Collinear helium under periodic driving: stabilisation of the asymmetric stretch orbit. to appear.

[359] E. M. Bollt and J. D. Skufca. Markov partitions. preprint 2002.

[360] D. Pingel, P. Schmelcher, and F. K. Diakonos. Theory and examples of the inverse Frobenius-Perron problem for complete chaotic maps. *Chaos* **9** (1999) 357.

[361] F. K. Diakonos and P. Schmelcher. On the construction of one-dimensional iterative maps from the invariant density: The dynamical route to the beta distribution. *Phys. Lett. A* **211** (1996) 199.

[362] F. K. Diakonos, D. Pingel, and P. Schmelcher. A stochastic approach to the construction of one-dimensional chaotic maps with prescribed statistical properties. *Phys. Lett. A* **264** (1999) 162.

[363] * F. K. Diakonos and P. Schmelcher. Turning point properties as a method for the characterization of the ergodic dynamics of one-dimensional iterative maps. *Chaos* **7** (1997) 239.

[364] * P. Schmelcher and F. K. Diakonos. A turning point analysis of the ergodic dynamics of iterative maps. *International Journal of Bifurcation and Chaos* **7** (1997) 2459.

[365] * F. K. Diakonos and P. Schmelcher. The turning point dynamics and the organization of chaos in iterative maps. *Nonlinear Phenomena in Complex Systems* **3** (2000) 81.

[366] M. C. Valsakumar, S. V. M. Satyanarayana, and S. Kanmani. Chaos, order statistics and unstable periodic orbits. *Journal of Physics A* **32** (1999) 6939.

[367] S. Ulam. *Problems in Modern Mathematics.* Interscience Publishers, New York, Ny, 1960.

[368] T.-Y. Li. Finite Approximation for the Frobenius-Perron operator. A Solution to Ulam's Conjecture. *J. Appox. Th.* **17** (1976) 177.

[369] A. Einstein. Über die von der molekularkinetischen Theorie der Wärme geforderte Bewegung von in ruhenden Flüssigkeiten suspendierten Teilchen. *Ann. d. Ph.* **17** (1905) 549.

[370] A. Boyarsky and M. Scarowsky. On a class of transitions which have unique absolutely continuous invariant measures. *Trans. Am. Math. Soc.* **255** (1979) 243.

[371] N. Friedman and A. Boyarsky. Matrices and eigenfunctions induced by Markov maps. *Lin. Alg. Appl.* **38** (1981) 141.

[372] W. Byers, P. Góra, and A. Boyarsky. Maximal absolutely continuous invariant measures for piecewise linear Markov transformations. *Ergod. Th. and Dynam. Sys.* **10** (1990) 645.

[373] P. Gaspard. Diffusion, effusion, and chaotic scattering. *J. Stat. Phys.* **68** (1992) 673.

[374] G. Strang and G. Fix. *An Analysis of the Finite Element Method.* Prentice–Hall, Englewood Cliffs, NJ, 1973.

[375] D. S. Burnett. *Finite Element Analysis: From Concepts to Applications.* Addison–Wesley, Reading, MA, 1987.

[376] D. Gottlieb and S. A. Orszag. *Numerical Analysis of Spectral Methods: Theory and Applications.* S.I.A.M., Philadelphia, 1977.

[377] C. Canuto, M. Y. Hussaini, A. Quarteroni, and T. A. Zang. *Spectral Methods in Fluid Dynamics.* Springer, New York, 1988.

[378] M. Abramowitz and I. A. Stegun. *Pocketbook of Mathematical Functions.* Verlag Harry Deutsch, Frankfurt a.M., 1984.

[379] G. Eilenberger. *Solitons.* Springer Series in Solid-State Sciences 19. Springer, Heidelberg, 1981.

[380] R. A. FitzHugh. *Biophys. J.* **1** (1961) 445.

[381] A. C. Newell and J. A. Whitehead. *J. Fluid Mech.* **38** (1969) 279.

[382] L. A. Segel. Distant side-walls cause slow amplitude modulation of cellular convection. *J. Fluid Mech.* **38** (1969) 203.

[383] K. Stewartson and J. T. Stuart. A non-linear instability theory for a wave system in plane Poiseuille flow. *J. Fluid Mech.* **48** (1971) 529.

[384] J. S. Russell. Report on Waves. *British Association Reports* (1844).

[385] G. I. Sivashinsky. Instabilities, pattern formation, and turbulence in flames. *Ann. Rev. Fluid Mech.* **15** (1983) 179.

[386] G. I. Sivashinsky and D. M. Michelson. On irregular wavy flow of a liquid film down a vertical plane. *Prog. Theor. Phys.* **63** (1980) 2112.

[387] Y. Kuramoto and T. Tsuzuki. On the formation of dissipative structures in the reaction-diffusion systems: Reductive perturbation approach. *Prog. Theor. Phys.* **54** (1975) 687.

[388] B. M. Boghosian, C. C. Chow, and T. Hwa. Hydrodynamics of the Kuramoto-Sivashinsky equation in two dimensions. *Phys. Rev. Lett.* **83** (1999) 5262.

10 Tables

$\cdot$	$\mathbf{C}_{0+}$	$\mathbf{C}_{1+}$	$\mathbf{C}_{2+}$	$\mathbf{C}_{3+}$	$\mathbf{C}_{0-}$	$\mathbf{C}_{1-}$	$\mathbf{C}_{2-}$	$\mathbf{C}_{3-}$
$\mathbf{C}_{0+}$	$\mathbf{C}_{0+}$	$\mathbf{C}_{1+}$	$\mathbf{C}_{2+}$	$\mathbf{C}_{3+}$	$\mathbf{C}_{0-}$	$\mathbf{C}_{1-}$	$\mathbf{C}_{2-}$	$\mathbf{C}_{3-}$
$\mathbf{C}_{1+}$	$\mathbf{C}_{1+}$	$\mathbf{C}_{2+}$	$\mathbf{C}_{3+}$	$\mathbf{C}_{0+}$	$\mathbf{C}_{3-}$	$\mathbf{C}_{0-}$	$\mathbf{C}_{1-}$	$\mathbf{C}_{2-}$
$\mathbf{C}_{2+}$	$\mathbf{C}_{2+}$	$\mathbf{C}_{3+}$	$\mathbf{C}_{0+}$	$\mathbf{C}_{1+}$	$\mathbf{C}_{2-}$	$\mathbf{C}_{3-}$	$\mathbf{C}_{0-}$	$\mathbf{C}_{1-}$
$\mathbf{C}_{3+}$	$\mathbf{C}_{3+}$	$\mathbf{C}_{0+}$	$\mathbf{C}_{1+}$	$\mathbf{C}_{2+}$	$\mathbf{C}_{1-}$	$\mathbf{C}_{2-}$	$\mathbf{C}_{3-}$	$\mathbf{C}_{0-}$
$\mathbf{C}_{0-}$	$\mathbf{C}_{0-}$	$\mathbf{C}_{1-}$	$\mathbf{C}_{2-}$	$\mathbf{C}_{3-}$	$\mathbf{C}_{0+}$	$\mathbf{C}_{1+}$	$\mathbf{C}_{2+}$	$\mathbf{C}_{3+}$
$\mathbf{C}_{1-}$	$\mathbf{C}_{1-}$	$\mathbf{C}_{2-}$	$\mathbf{C}_{3-}$	$\mathbf{C}_{0-}$	$\mathbf{C}_{3+}$	$\mathbf{C}_{0+}$	$\mathbf{C}_{1+}$	$\mathbf{C}_{2+}$
$\mathbf{C}_{2-}$	$\mathbf{C}_{2-}$	$\mathbf{C}_{3-}$	$\mathbf{C}_{0-}$	$\mathbf{C}_{1-}$	$\mathbf{C}_{2+}$	$\mathbf{C}_{3+}$	$\mathbf{C}_{0+}$	$\mathbf{C}_{1+}$
$\mathbf{C}_{3-}$	$\mathbf{C}_{3-}$	$\mathbf{C}_{0-}$	$\mathbf{C}_{1-}$	$\mathbf{C}_{2-}$	$\mathbf{C}_{1+}$	$\mathbf{C}_{2+}$	$\mathbf{C}_{3+}$	$\mathbf{C}_{0+}$

Table 1: Multiplication table of the 2×2–matrices $\mathbf{C}_{k\sigma}$

$\mathcal{C}^1$	$\mathcal{C}^2$	$\mathcal{C}^3$	$\nearrow$	$\mathcal{A}_{0+}$	$\mathcal{A}_{1+}$	$\mathcal{A}_{2+}$	$\mathcal{A}_{3+}$	$\mathcal{A}_{0-}$	$\mathcal{A}_{1-}$	$\mathcal{A}_{2-}$	$\mathcal{A}_{3-}$
			$\mathcal{A}_{0+}$	$\mathbf{C}_{0+}$	$\mathbf{C}_{1+}$	$\mathbf{C}_{2+}$	$\mathbf{C}_{3+}$	$\mathbf{C}_{0-}$	$\mathbf{C}_{1-}$	$\mathbf{C}_{2-}$	$\mathbf{C}_{3-}$
$*$		$*$	$\mathcal{A}_{1+}$	$\mathbf{C}_{3+}$	$\mathbf{C}_{0+}$	$\mathbf{C}_{1+}$	$\mathbf{C}_{2+}$	$\mathbf{C}_{1-}$	$\mathbf{C}_{2-}$	$\mathbf{C}_{3-}$	$\mathbf{C}_{0-}$
$*$	$*$	$*$	$\mathcal{A}_{2+}$	$\mathbf{C}_{2+}$	$\mathbf{C}_{3+}$	$\mathbf{C}_{0+}$	$\mathbf{C}_{1+}$	$\mathbf{C}_{2-}$	$\mathbf{C}_{3-}$	$\mathbf{C}_{0-}$	$\mathbf{C}_{1-}$
	$*$		$\mathcal{A}_{3+}$	$\mathbf{C}_{1+}$	$\mathbf{C}_{2+}$	$\mathbf{C}_{3+}$	$\mathbf{C}_{0+}$	$\mathbf{C}_{3-}$	$\mathbf{C}_{0-}$	$\mathbf{C}_{1-}$	$\mathbf{C}_{2-}$
$*$	$*$	$*$	$\mathcal{A}_{0-}$	$\mathbf{C}_{0-}$	$\mathbf{C}_{1-}$	$\mathbf{C}_{2-}$	$\mathbf{C}_{3-}$	$\mathbf{C}_{0+}$	$\mathbf{C}_{1+}$	$\mathbf{C}_{2+}$	$\mathbf{C}_{3+}$
$*$	$*$	$*$	$\mathcal{A}_{1-}$	$\mathbf{C}_{1-}$	$\mathbf{C}_{2-}$	$\mathbf{C}_{3-}$	$\mathbf{C}_{0-}$	$\mathbf{C}_{3+}$	$\mathbf{C}_{0+}$	$\mathbf{C}_{1+}$	$\mathbf{C}_{2+}$
$*$	$*$	$*$	$\mathcal{A}_{2-}$	$\mathbf{C}_{2-}$	$\mathbf{C}_{3-}$	$\mathbf{C}_{0-}$	$\mathbf{C}_{1-}$	$\mathbf{C}_{2+}$	$\mathbf{C}_{3+}$	$\mathbf{C}_{0+}$	$\mathbf{C}_{1+}$
$*$	$*$	$*$	$\mathcal{A}_{3-}$	$\mathbf{C}_{3-}$	$\mathbf{C}_{0-}$	$\mathbf{C}_{1-}$	$\mathbf{C}_{2-}$	$\mathbf{C}_{1+}$	$\mathbf{C}_{2+}$	$\mathbf{C}_{3+}$	$\mathbf{C}_{0+}$

Table 2: Transition matrices $\mathbf{C}_{k\sigma}$ necessary for transitions between different classes $\mathcal{A}_{l\tau}$ of stability matrices of fixed points. The first three columns indicate the combination of classes occurring in a two dimensional chaotic dynamical system.

period	number of primitive periodic orbits	number of fixed points	topological entropy
1	1	1	0.0
2	1	3	0.549
3	2	7	0.648
4	3	15	0.677
5	4	21	0.608
6	7	51	0.655
7	10	71	0.609
8	14	127	0.606
9	26	241	0.609
10	45	473	0.616
11	76	837	0.612
12	110	1383	0.603
13	194	2523	0.603
14	317	4512	0.601
15	566	8518	0.603

Table 3: Number of different primitive periodic orbits, the number of fixed points and the topological entropy for the periodic orbits of the Ikeda map for period $p = 1...15$

number of inter-sections	number of primitive periodic orbits	mean period	λ	number of converged points
2	1	0.941	0.1	1
3	2	1.394	0.1	3
4	3	1.843	0.1	11
5	6	2.305	0.05	17
6	9	2.756	0.01	144
7	18	3.219	0.01	40
8	30	3.676	0.001	192
9	56	4.136	0.001	687
10	99	4.595	0.001	1094
11	186	5.054	0.001	2523
12	335	5.514	0.0001	3773
13	630	5.974	0.0001	10498
14	1160	6.433	0.0001	11472

Table 4: Lorenz system: Properties of the periodic orbits with 2 through 14 intersection points with the Poincaré surface of section, the parameter λ and the minimal number of converged initial points N_i, sampled randomly from the attractor.

number of inter-sections	number of primitive periodic orbits	mean period	λ	number of converged points
1	29	10.814	0.005	482
2	14	15.248	0.005	1348
3	16	6.055	0.005	462
4	13	14.333	0.005	48
5	12	9.955	0.001	173
6	19	12.320	0.001	209
7	19	14.519	0.001	650
8	11	17.083	0.001	432
9	11	18.554	0.0005	126

Table 5: Hydrogen atom in magnetic field: Properties of periodic orbits with 1 to 9 intersections with the Poincaré surface, the parameter λ and the required number of converged initial points N_i.

No	Period $''12''$-Code	$''12''$-Code	$''+-''$-Code	λ
1	1	1	$+$	—
2	2	12	$-$	0.6011
3	3	112	$+--$	1.8604
4	4	1112	$++--$	2.3418
5	4	1122	$+-$	1.8622
6	5	11112	$+++--$	2.7207
7	5	11122	$++-+-$	5.1551
8	5	11212	$+----$	3.3424
9	6	111112	$++++--$	3.0323
10	6	111122	$+++-+-$	6.1393
11	6	111212	$++---$	4.3315
12	6	111222	$++-$	6.8573
13	6	112122	$+-+---$	5.0002
14	7	1111112	$++++$	3.2965
15	7	1111122	$+++-+-$	6.8485
16	7	1111212	$+++----$	5.1755
17	7	1111222	$+++-++-$	8.0225
18	7	1112112	$++--+--$	4.3409
19	7	1112122	$++---+-$	6.4432
20	7	1112212	$++-+---$	6.4432
21	7	1121122	$+-+-+--$	5.9547
22	7	1121212	$+-------$	4.6613

Table 6: Collinear periodic orbits of the helium atom up to length 7. Listed are prime orbits only. λ is the Lyapunov exponent of the corresponding orbit.

11 Figures

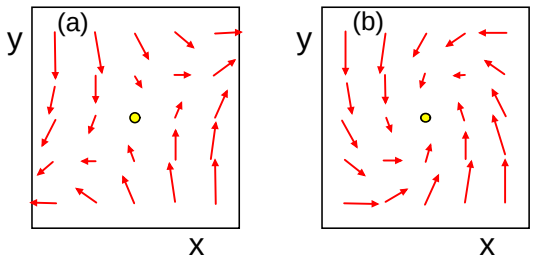

Figure 1: Stabilisation of a stationary point of a flow (a) by changing the sign of the x–component of the vector field (b). This corresponds to a multiplication of the vector field with the matrix $\left(\begin{smallmatrix} -1 & 0 \\ 0 & 1 \end{smallmatrix}\right)$.

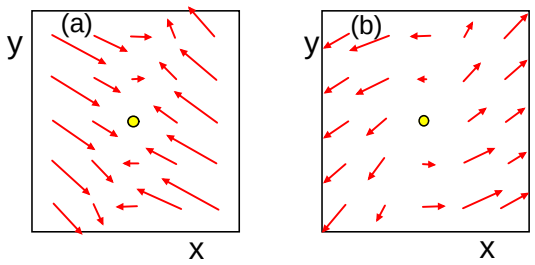

Figure 2: Stationary point of a flow as in Fig. 1 , but with different stability properties. The transformation of the vector field by multiplication with the matrix $\left(\begin{smallmatrix} -1 & 0 \\ 0 & 1 \end{smallmatrix}\right)$ results not in a stable stationary point in this case. A different transformation has to be applied in order to achieve stabilisation.

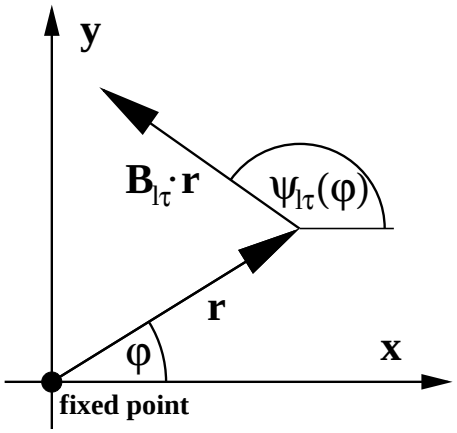

Figure 3: Definition of the polar angles ϕ and $\psi_{l\tau}(\phi)$ of the displacement $\mathbf{r} = (\cos\phi, \sin\phi)^T$ relative to the fixed point at $(0,0)$ and the flow $(\cos\psi_{l\tau}, \sin\psi_{l\tau})^T$in $\mathbf{r}$. $(k\sigma)$ indicate the particular stability transformation applied according to Eqn. (11).

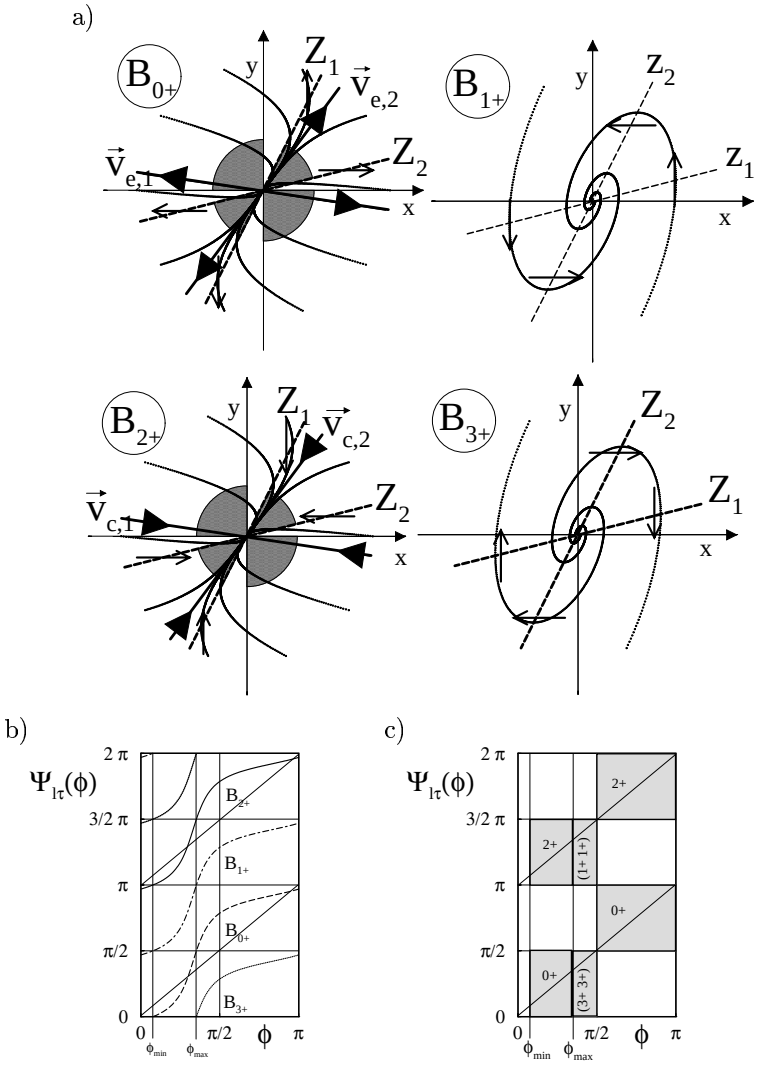

Figure 4: a) Phase portraits of a fixed point with $\det(\mathbf{B}_{l\tau}) > 0$, $0 < \phi_{min},\ \phi_{max} < \pi/2$, (x, y) being the coordinates with respect to the FP. The manifolds Z_1, Z_2 are displayed as long dashed lines. The direction of the flow on the Z_1, Z_2–lines is indicated by open arrows. Full arrows show the eigenvectors ($\vec{v}_e$, $\vec{v}_c$ for saddle points, $\vec{v}_{e,i}$, $\vec{v}_{c,i}$ for sources and sinks, respectively). Some trajectories indicate the flow around the FP. Sub-figures b) and c) show the corresponding $\psi_{l\tau}(\phi)$–diagrams. Areas shaded grey indicate the intervals of the locations of the eigenvectors, corresponding to the shaded boxes in c) which show these intervals for the four fixed points discussed. Indices $l\tau$ in the boxes correspond to the class $\mathcal{A}_{l\tau}$ of matrices whose real eigenvectors have polar angles in this particular interval of ϕ. Two indices given in brackets indicate the possibility of either two real eigenvalues with eigenvectors in this range (sink or source) or complex eigenvalues without real eigenvectors of the corresponding matrix (spiral points). For details of the figures a), b) and c) see section 4.1.1.

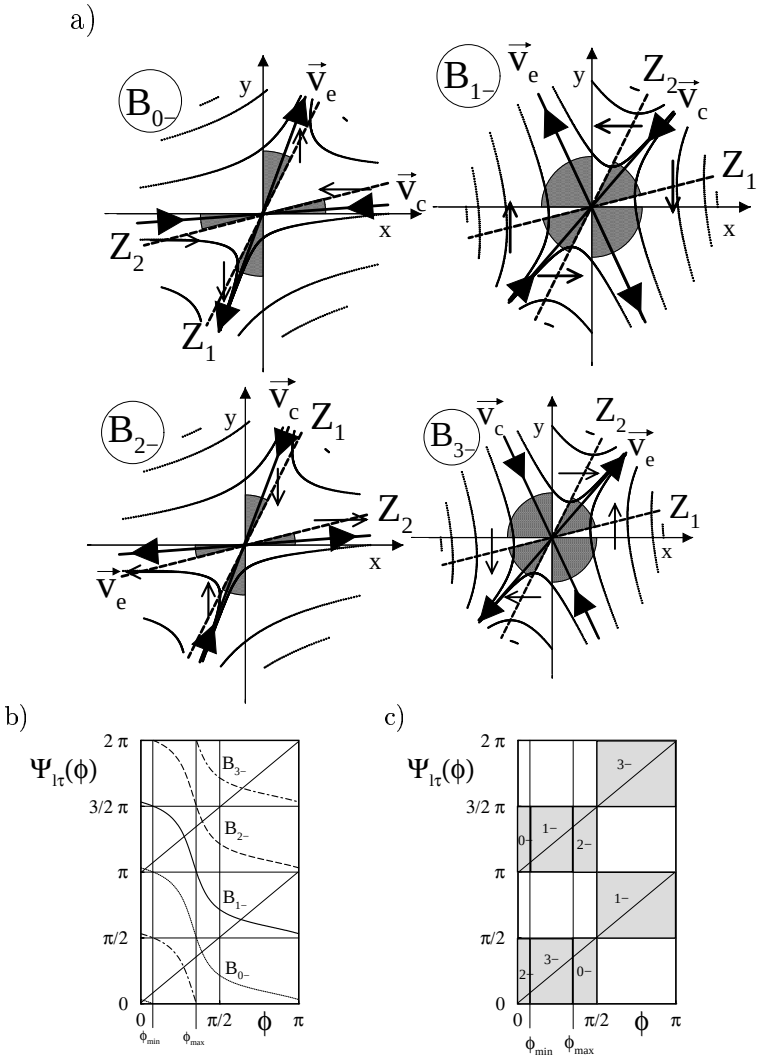

Figure 5: Phase portraits of a fixed point and corresponding $\psi_{l\tau}(\phi)$-diagrams as in Fig. 4, but with $\det(\mathbf{B}_{l\tau}) < 0$, $0 < \phi_{min},\ \phi_{max} < \pi/2$,

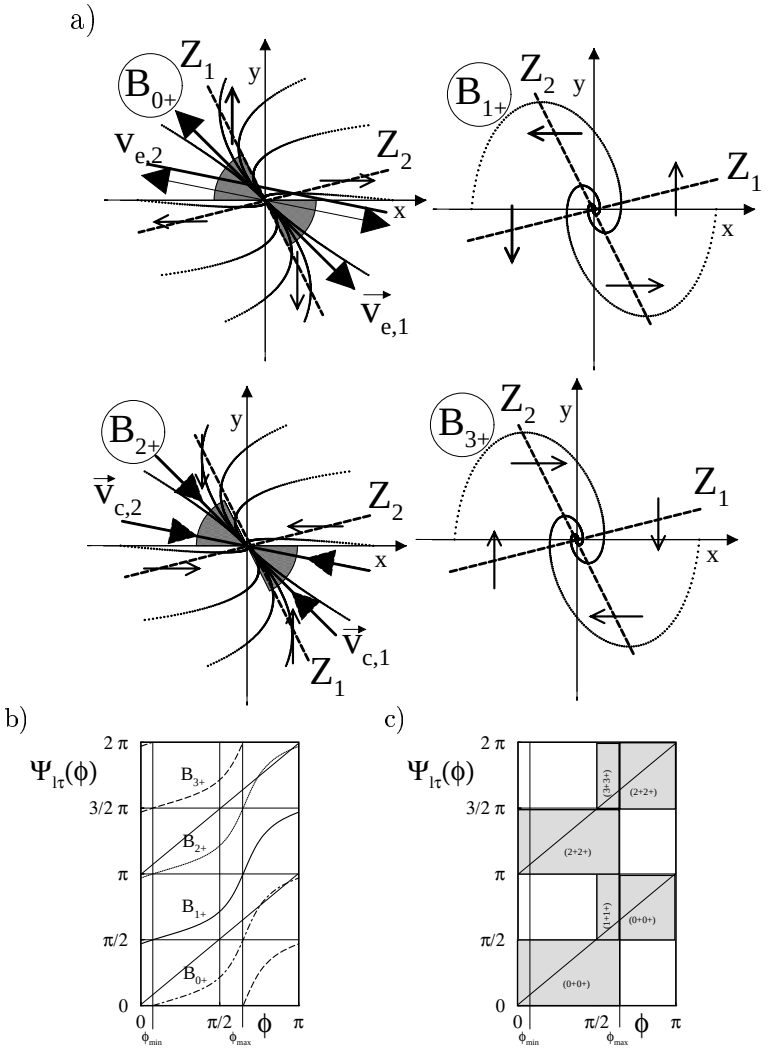

Figure 6: Phase portraits of a fixed point and corresponding $\psi_{l\tau}(\phi)$-diagrams as in Fig. 4, but with $\det(\mathbf{B}_{l\tau}) > 0$, $0 < \phi_{min} < \pi/2 < \phi_{max}$,

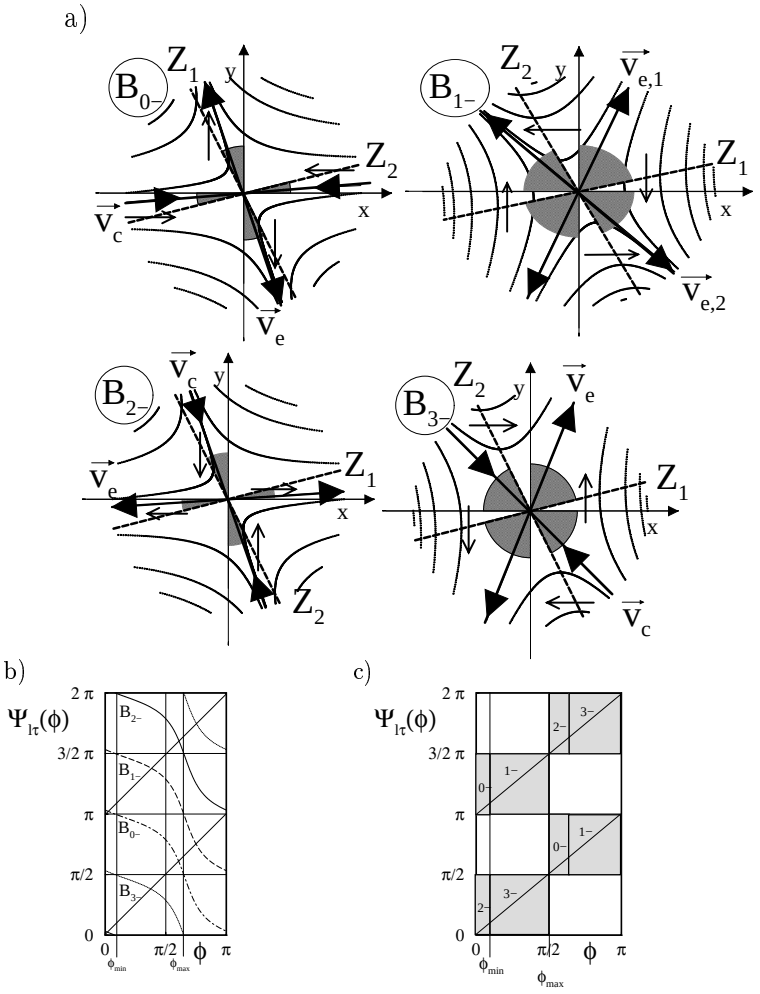

Figure 7: Phase portraits of a fixed point and corresponding $\psi_{l\tau}(\phi)$-diagrams as in Fig. 4, but with $\det(\mathbf{B}_{l\tau}) < 0$, $0 < \phi_{min} < \pi/2 < \phi_{max}$,

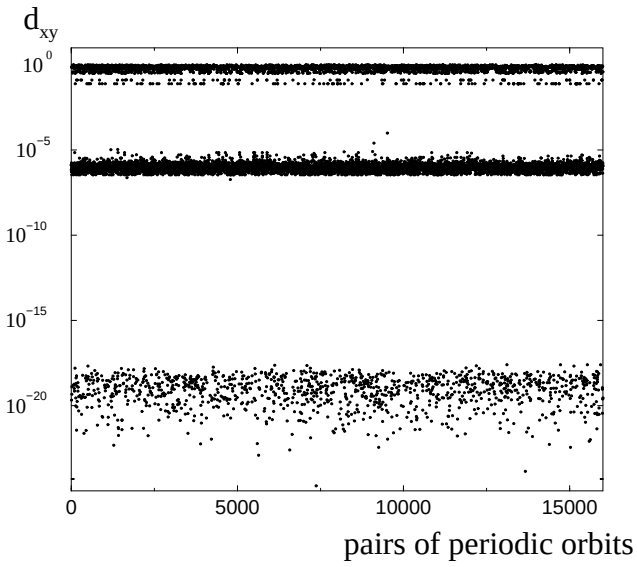

Figure 8: Distribution of the distances d_{xy} of periodic orbits of the Ikeda map of length $p = 15$, taken from the converged trajectories in N_1, as defined in Eqn. (15).

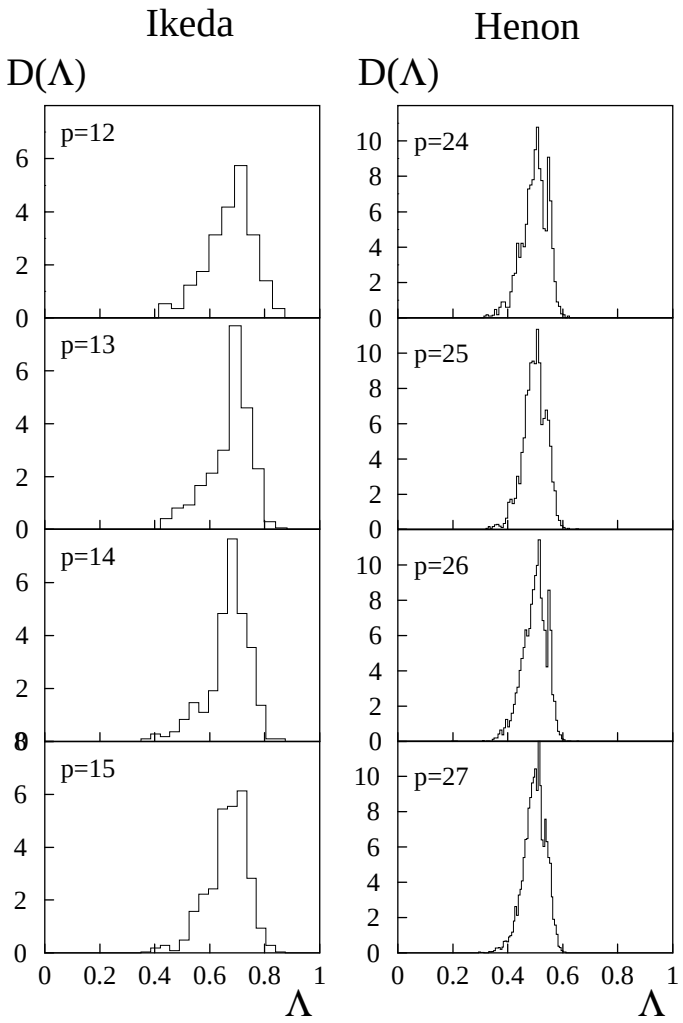

Figure 9: Normalised distributions of the Lyapunov exponents of the periodic orbits of the Ikeda map and Hénon map. Only primitive periodic orbits are shown.

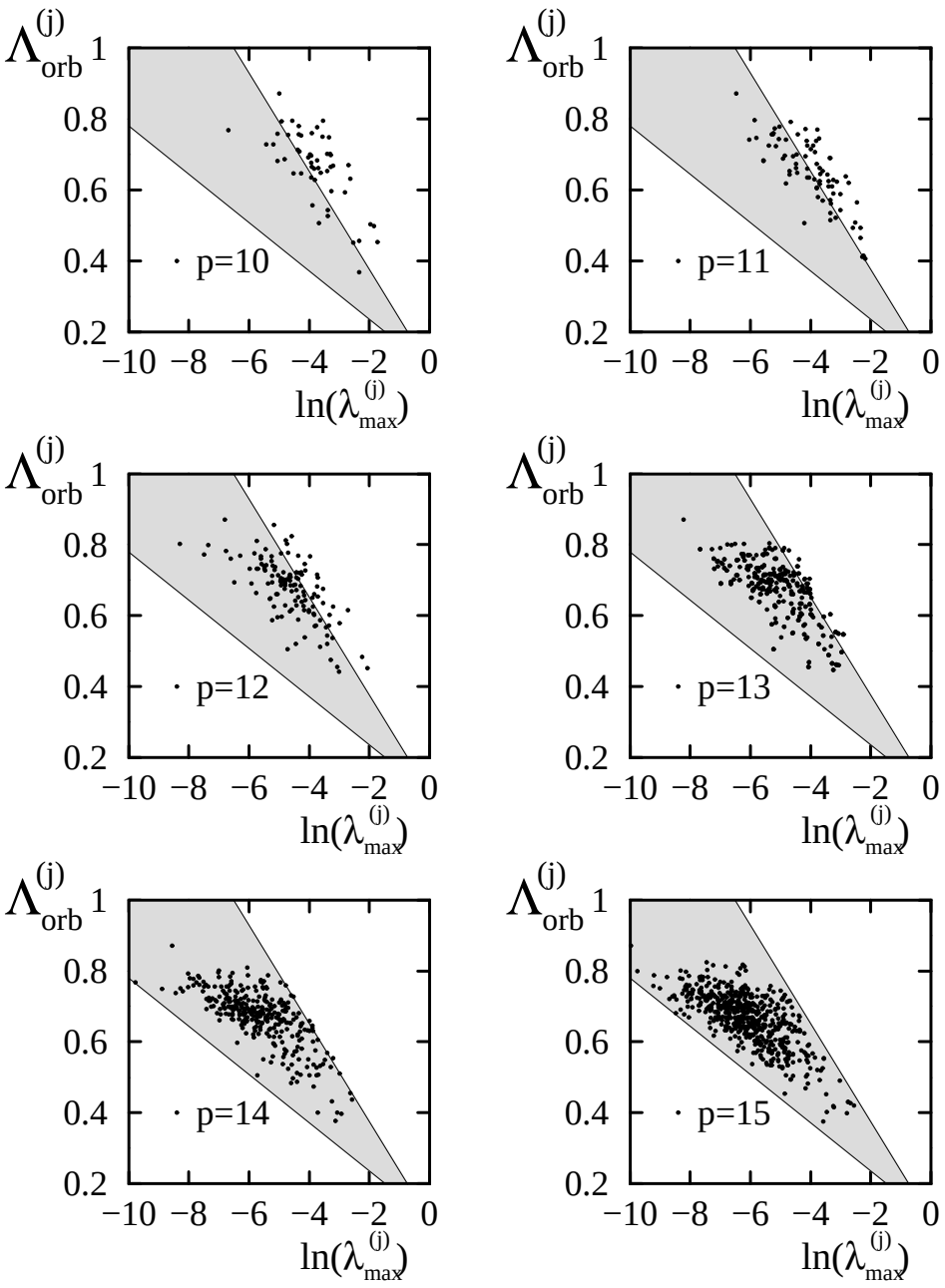

Figure 10: Distribution of Lyapunov exponents $\Lambda_{orb}^{(j)}$ of the stabilised periodic orbits versus the critical parameter $\lambda_{\max}^{(j)}$ for the Ikeda–map, period $p = 10...15$. The areas shaded grey approximately correspond to the distribution for $p = 15$. See section 5.3 for a definition of $\lambda_{\max}^{(j)}$.

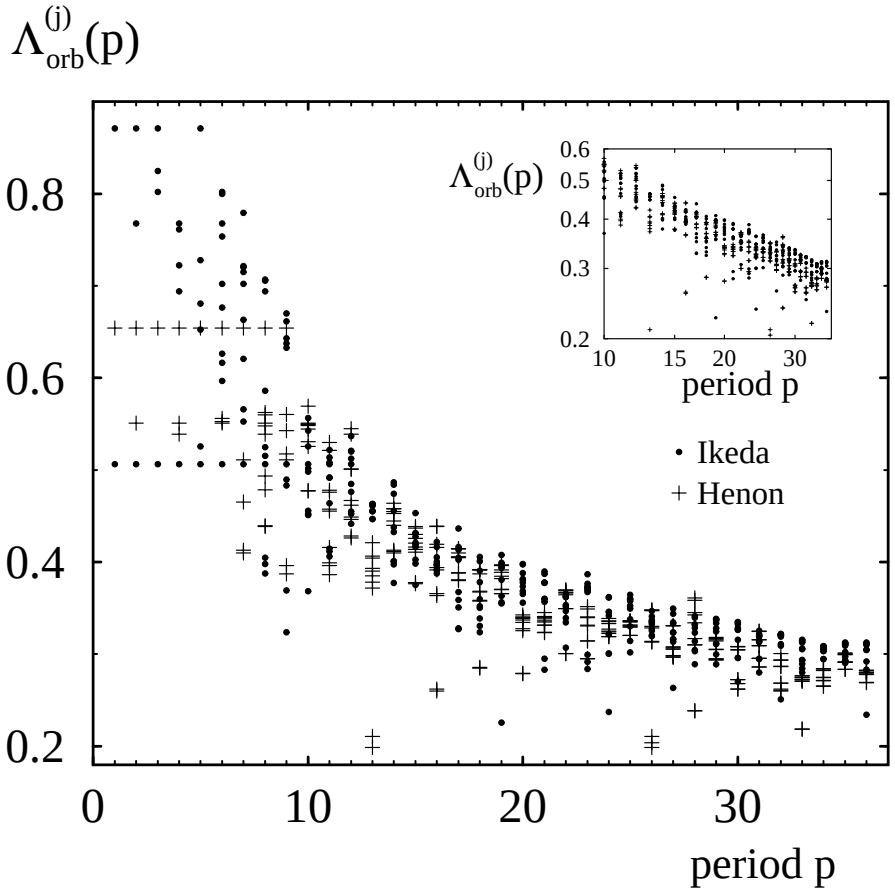

Figure 11: Lyapunov–exponents of the ten least unstable periodic orbits of the Ikeda map and Hénon map of length $p = 1...36$. The inset shows the same distribution for a log-log scale.

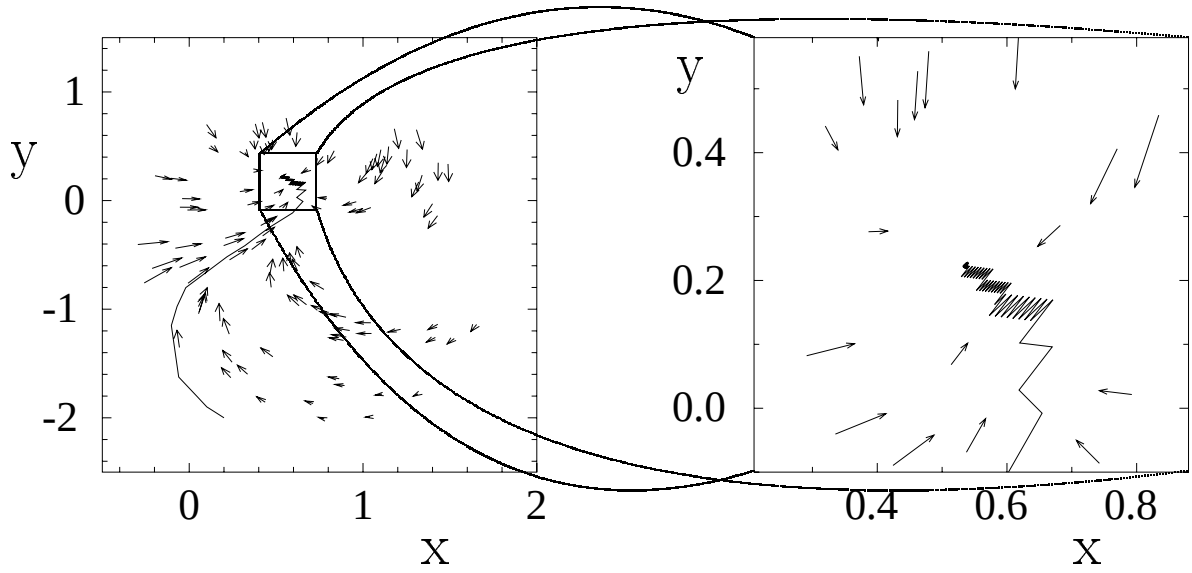

Figure 12: Trajectory of the stability transformed system as applied to a time series of 100 points of the Ikeda system with a zoom into the neighbourhood of the fixed point. The convergence and the adiabatic scaling of the trajectory is clearly seen.

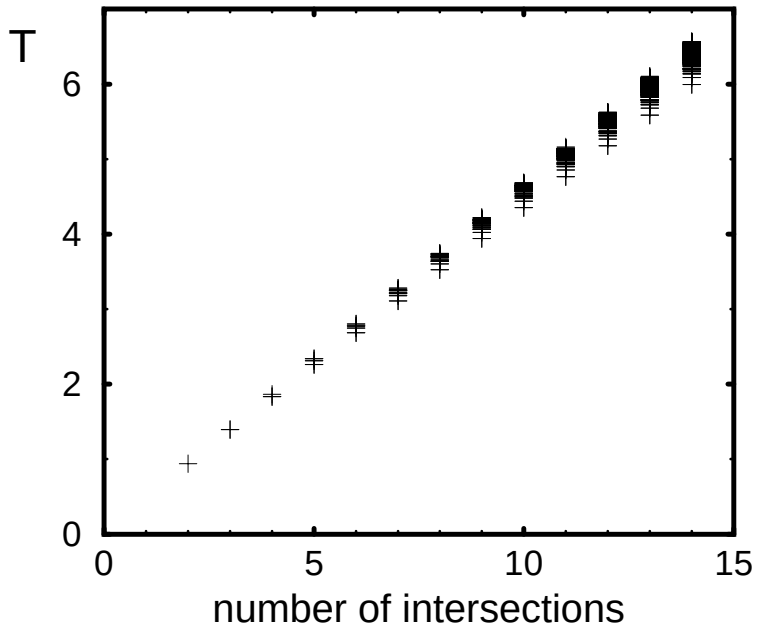

Figure 13: Lorenz system: The length T of the periodic orbits as function of the number of intersection points with the Poincaré surface of section.

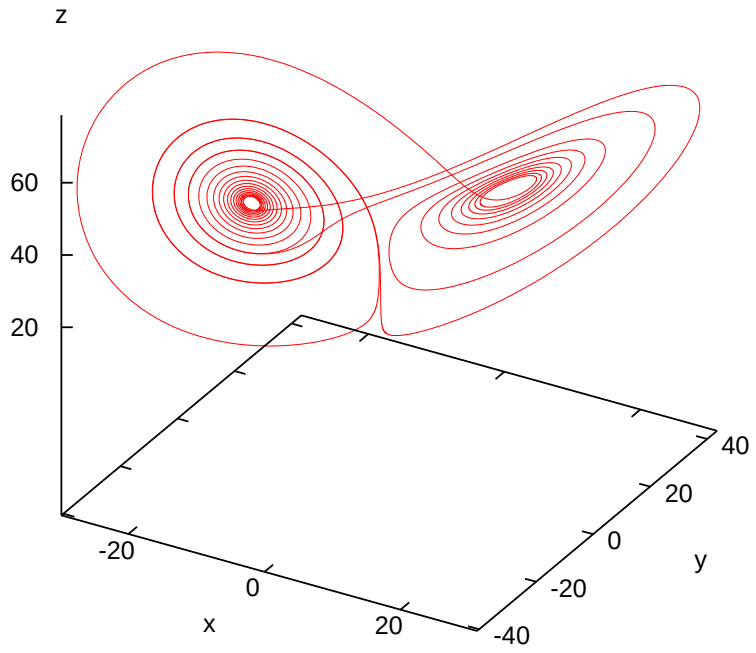

Figure 14: Lorenz system: Long periodic orbit with 30 intersection points with the Poincaré surface of section.

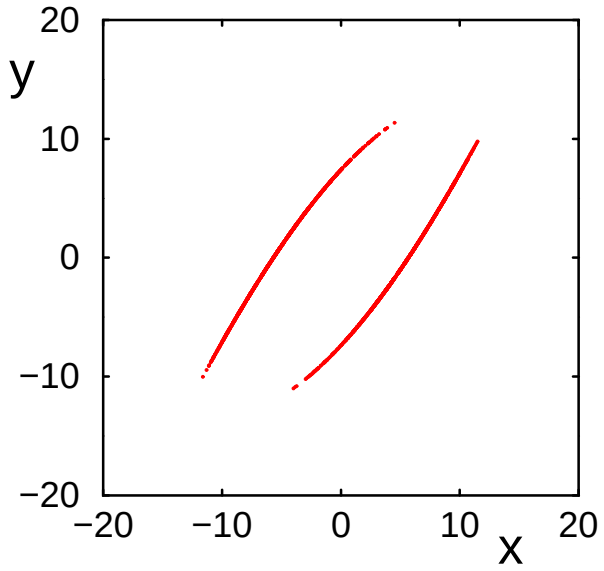

Figure 15: Lorenz system: Distribution of the intersections points in the Poincaré surface of section. Shown are periodic orbits of 2 through 14 intersections.

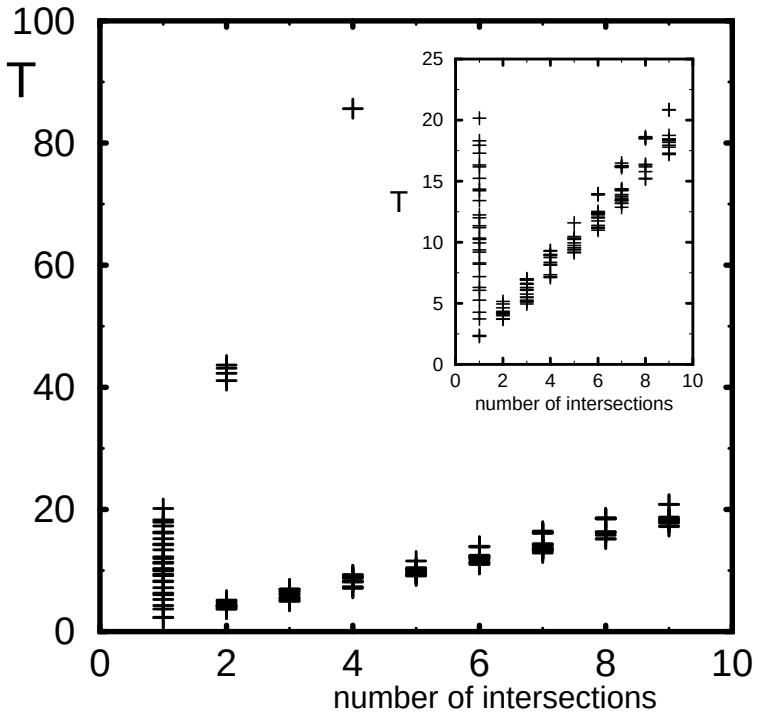

Figure 16: Hydrogen atom in magnetic field: Distribution of the length T of the periodic orbits versus the number of their intersections with the Poincaré surface of section. The inset shows a higher resolution for small values of T.

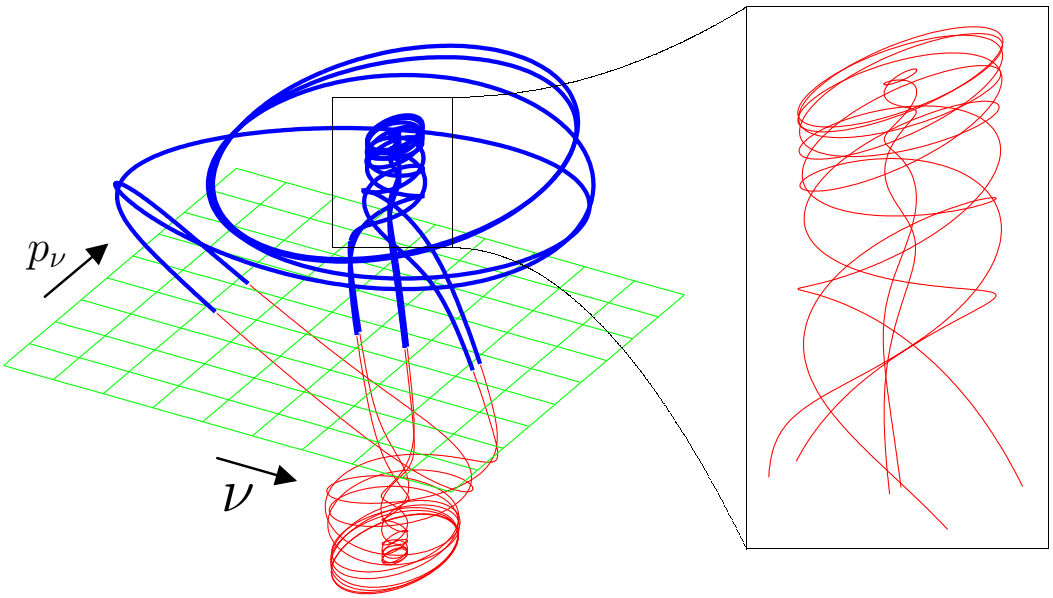

Figure 17: Hydrogen atom in magnetic field: Example of a long periodic orbit with just four intersections with the Poincaré surface of section. The dynamics below and above the surface is very complex

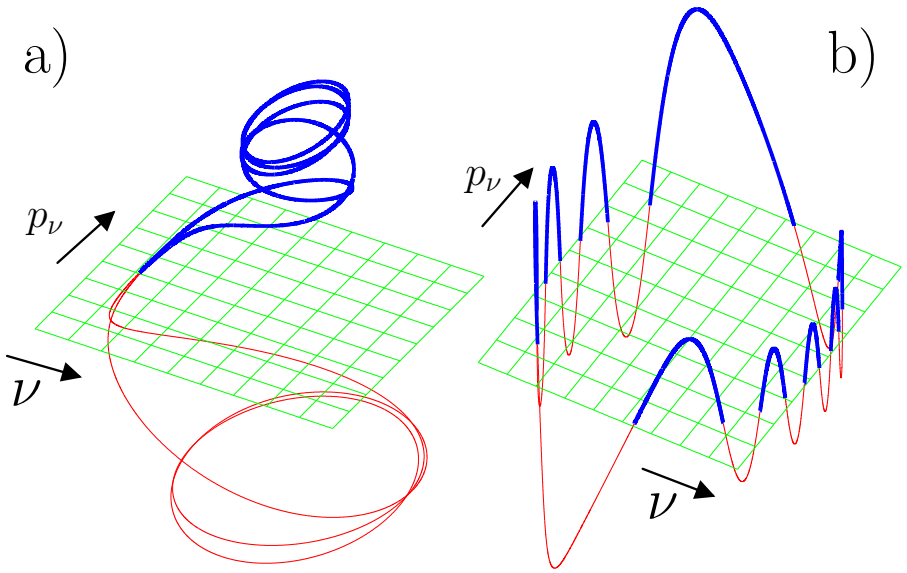

Figure 18: Hydrogen atom in magnetic field: Periodic orbit with a) a small number of intersections, located mainly above and below the Poincaré surface of section b) a large number of intersections, located mainly in the Poincaré surface of section

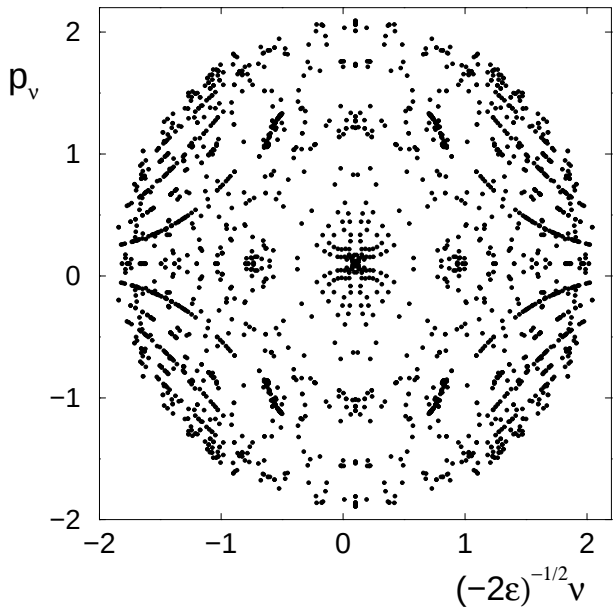

Figure 19: Hydrogen atom in magnetic field: Chaotic ergodic dynamics for a scaled energy of $\epsilon = -0.1$. Location of periodic orbits with 1 to 9 intersections in the Poincaré surface of section.

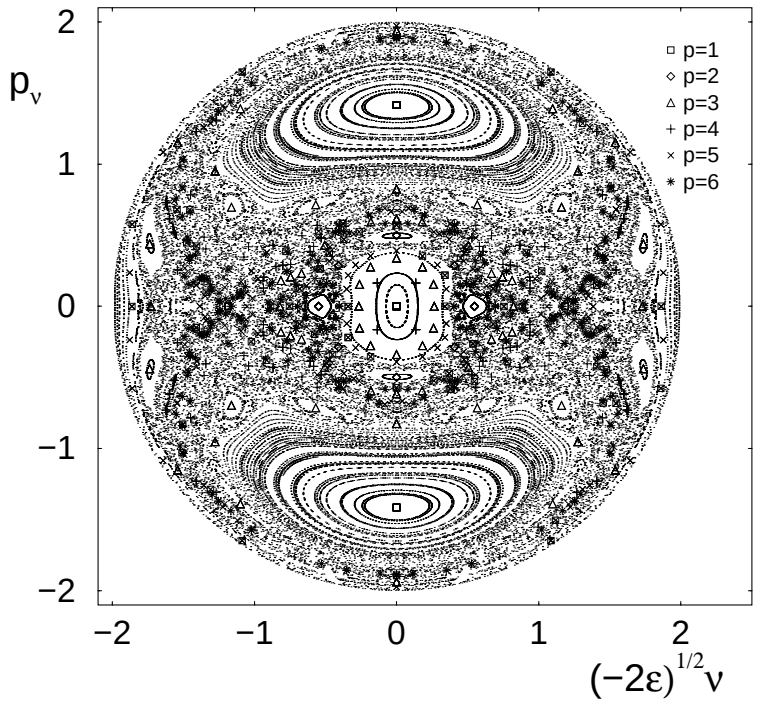

Figure 20: Hydrogen atom in magnetic field: Partially regular dynamics with mixed phase space for a scaled energy of $\epsilon = -0.4$. Shown are the positions of periodic orbits with 1 to 9 intersections in the Poincaré surface of section. The dots represent the intersection points of trajectories of the system with random initial conditions.

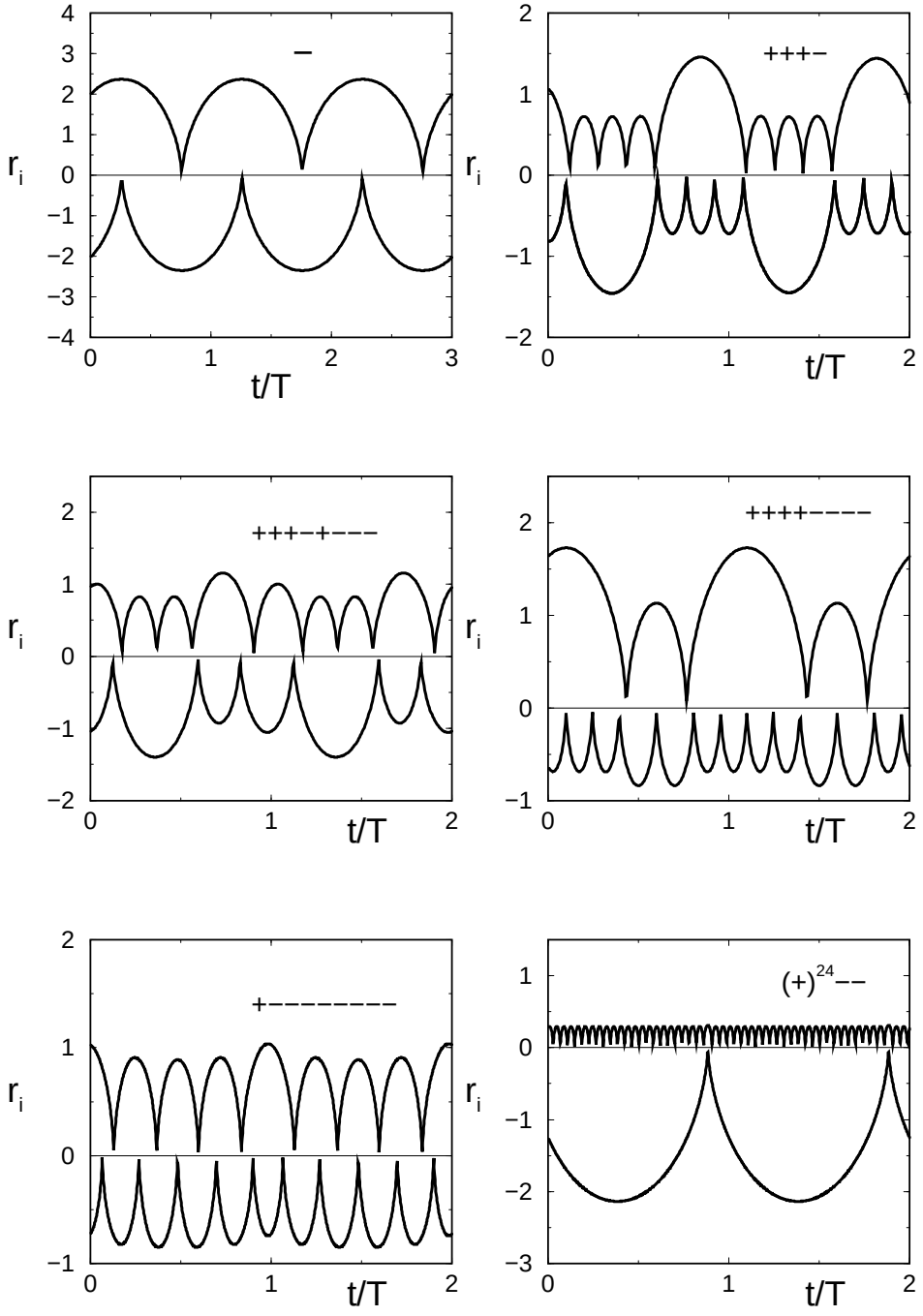

Figure 21: Time development of some periodic orbits of the collinear helium atom without external field. The nucleus is located at $r_i = 0$ (atomic units). The period of the orbits is $T = 2\pi$; the time evolution is shown for two periods. The symbolic code is the $''+-''$-alphabet. The orbit code with $''-''$ is the so-called asymmetric-stretch-orbit of the system. The periodic orbit with the symbolic code $''+-''$ shows a near-three-body-collision, which results in an orbit symmetric in r_1 and r_2.

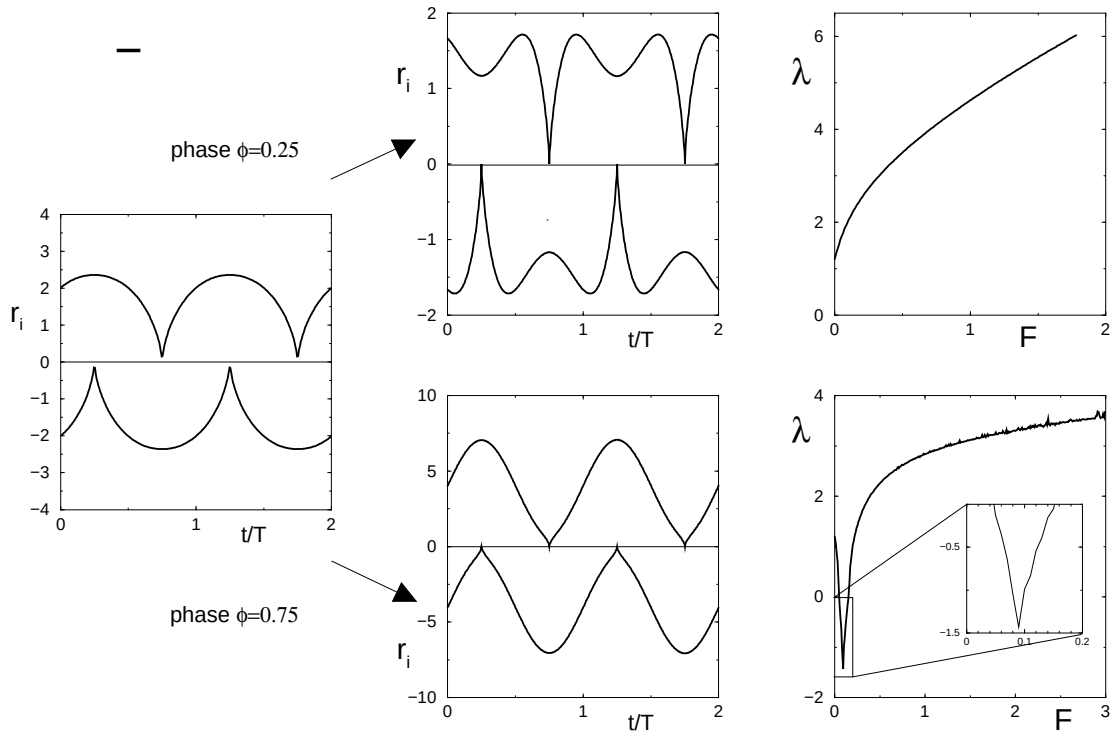

Figure 22: Asymmetric-stretch-orbit in the transition from zero to finite external field. The external field can have two phases, $\phi = 1/4$ and $\phi = 3/4$, with respect to the periodic orbit. Displayed are trajectories for both phases and the variation of the corresponding Lyapunov exponents with the field amplitude.

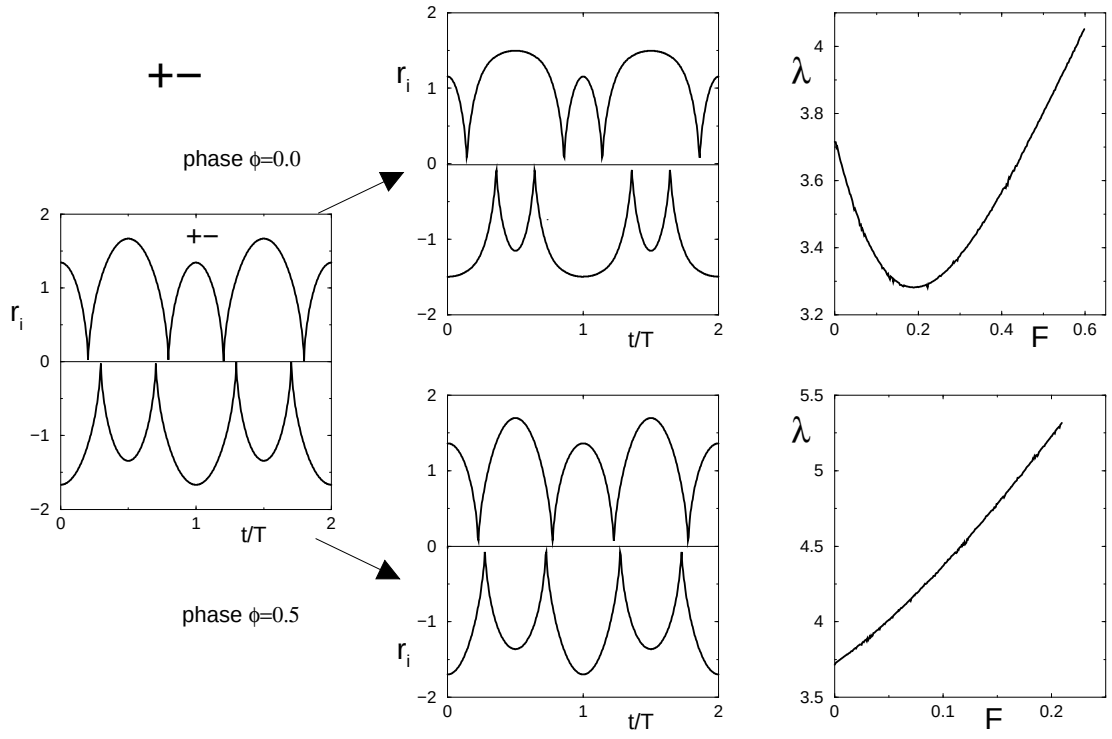

Figure 23: Periodic orbit with symbolic code $''+-''$ in the transition regime from zero to finite external field. The external field can have two phases, $\phi = 0$ and $\phi = 1/2$, with respect to the periodic orbit. Displayed are trajectories for both phases and the variation of the corresponding Lyapunov exponents with the field amplitude.

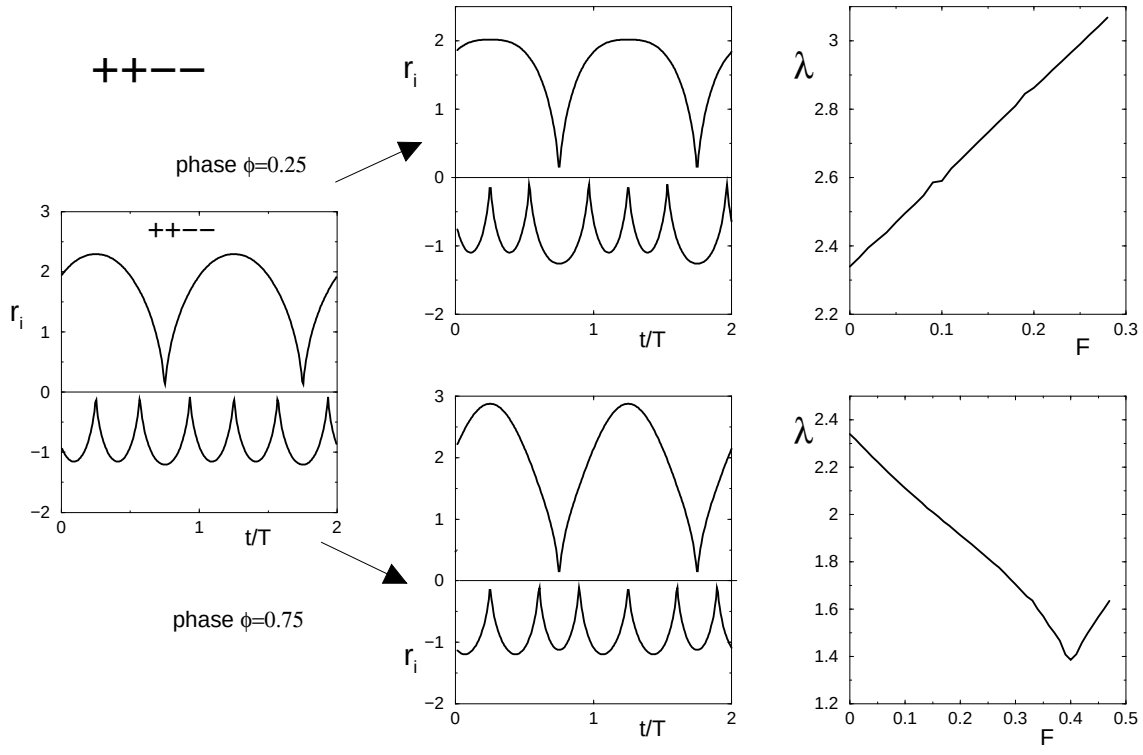

Figure 24: Periodic orbit with symbolic code $''++--''$ in the transition regime from zero to finite external field. The external field can have two phases, $\phi = 1/4$ and $\phi = 3/4$, with respect to the periodic orbit. Displayed are trajectories for both phases and the variation of the corresponding Lyapunov exponents with the field amplitude.

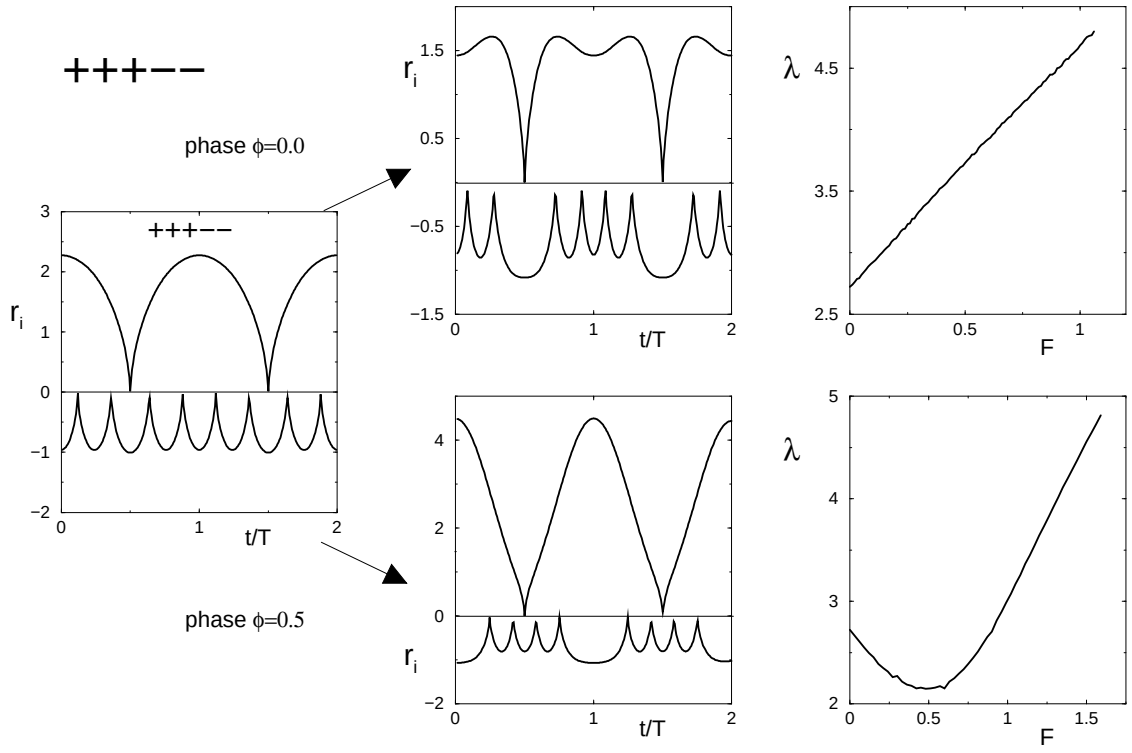

Figure 25: Periodic orbit with symbolic code $''+++--''$ in the transition regime from zero to finite external field. The external field can have two phases, $\phi = 0$ and $\phi = 1/2$, with respect to the periodic orbit. Displayed are trajectories for both phases and the variation of the corresponding Lyapunov exponents with the field amplitude.

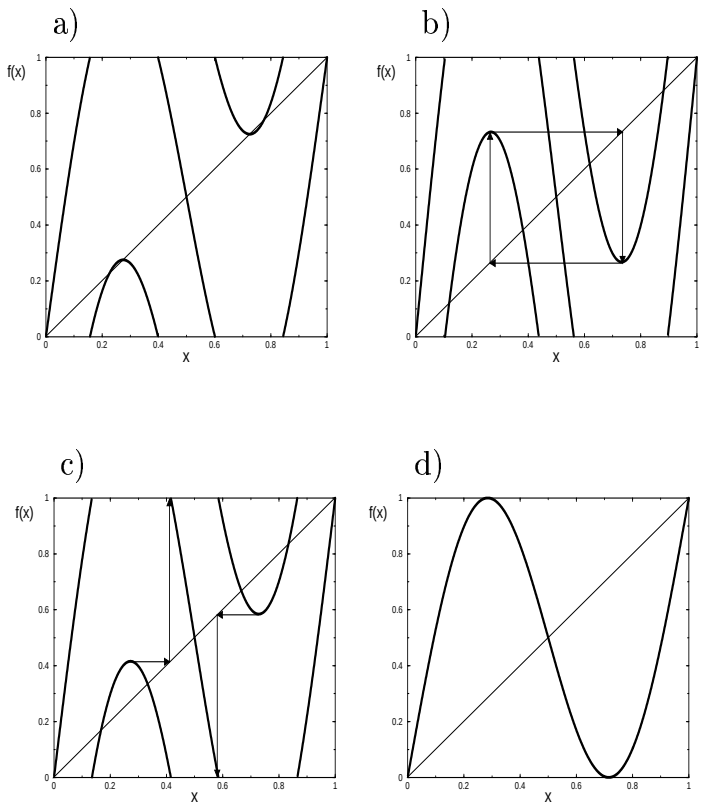

Figure 26: Example of a Markov partition of the sinusoidal map Eqn. (31). It is generated by trajectories that map the two extrema ϵ_1 and ϵ_2 either a) onto itself ($\epsilon_i \to \epsilon_i$), b) onto the corresponding other one ($\epsilon_1 \to \epsilon_2$, $\epsilon_2 \to \epsilon_1$), c) onto the trivial fixed points ($x = 0$, $x = 1$) of the map ($\epsilon_i \to 0,\ 1$). In d) the extrema ϵ_1 and ϵ_2 coincide with the trivial fixed points ($x = 0$, $x = 1$) of the map, which defines a Markov partition, too.

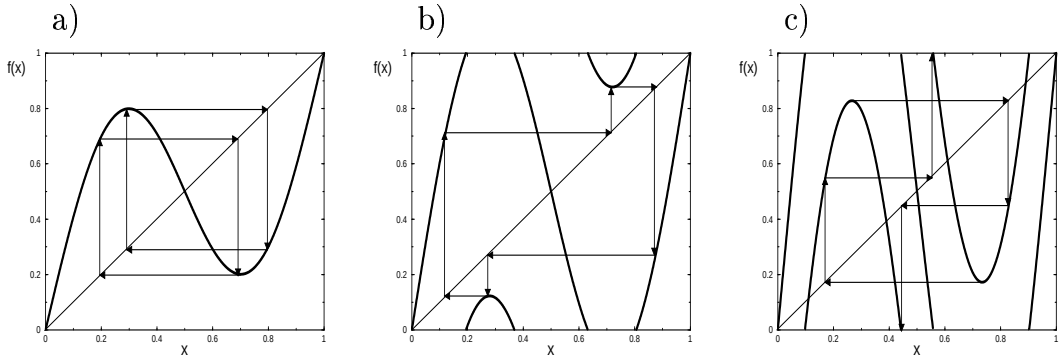

Figure 27: Some examples of Markov-Partitions of the sinusoidal map Eqn. (31) with a depth of iteration of $p = 2$. Both extrema ϵ_1 and ϵ_2 are mapped in $p = 2$ steps a) onto itself($\epsilon_i \to \epsilon_i$), b) onto the corresponding second extrema ($\epsilon_1 \to \epsilon_2$, $\epsilon_2 \to \epsilon_1$), c) onto the trivial fixed point of the map ($x = 0$, $x = 1$) ($\epsilon_i \to 0,\ 1$).

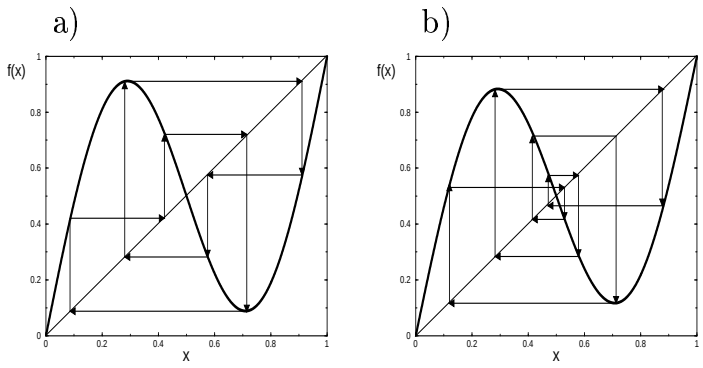

Figure 28: Example of a Markov-partition of the sinusoidal map Eqn. (31) with a depth of a) $p = 3$, b) $p = 4$. The extrema ϵ_1 and ϵ_2 are mapped onto each other after p iterations ($\epsilon_i \to \epsilon_i$).

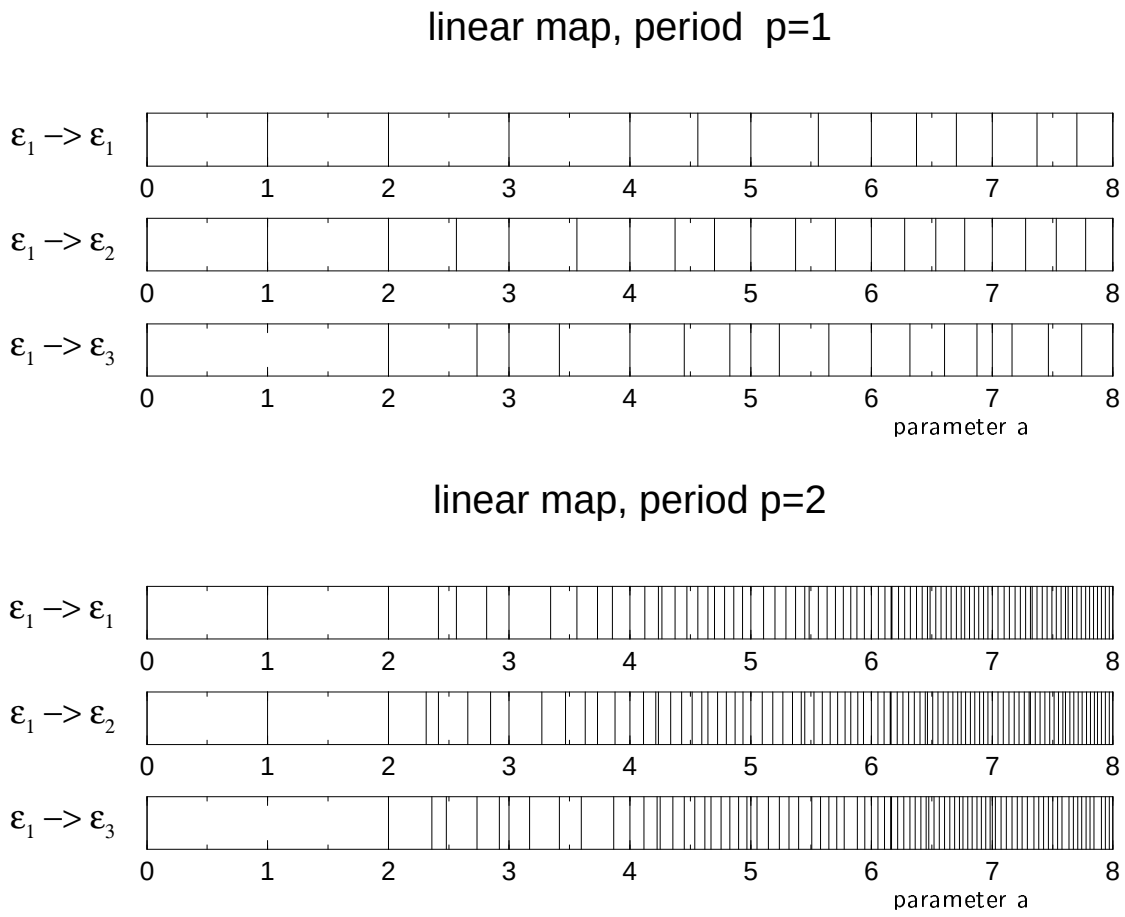

Figure 29: Distribution of the parameter values a corresponding to a Markov-partition of the linear map Eqn. (30). p is the the depth of the iteration and the fineness of the resulting partition. A depth of p corresponds to a partition with $2p+1$ regions. ϵ_1 and ϵ_2 are the two values of the extremum at $x = 0$, ϵ_3 is the trivial fixed point at $x = -1/2 \equiv 1/2$. The different possible transitions between the ϵ_i by the map $f_a^{(p)}$ determine the different classes of partitions.

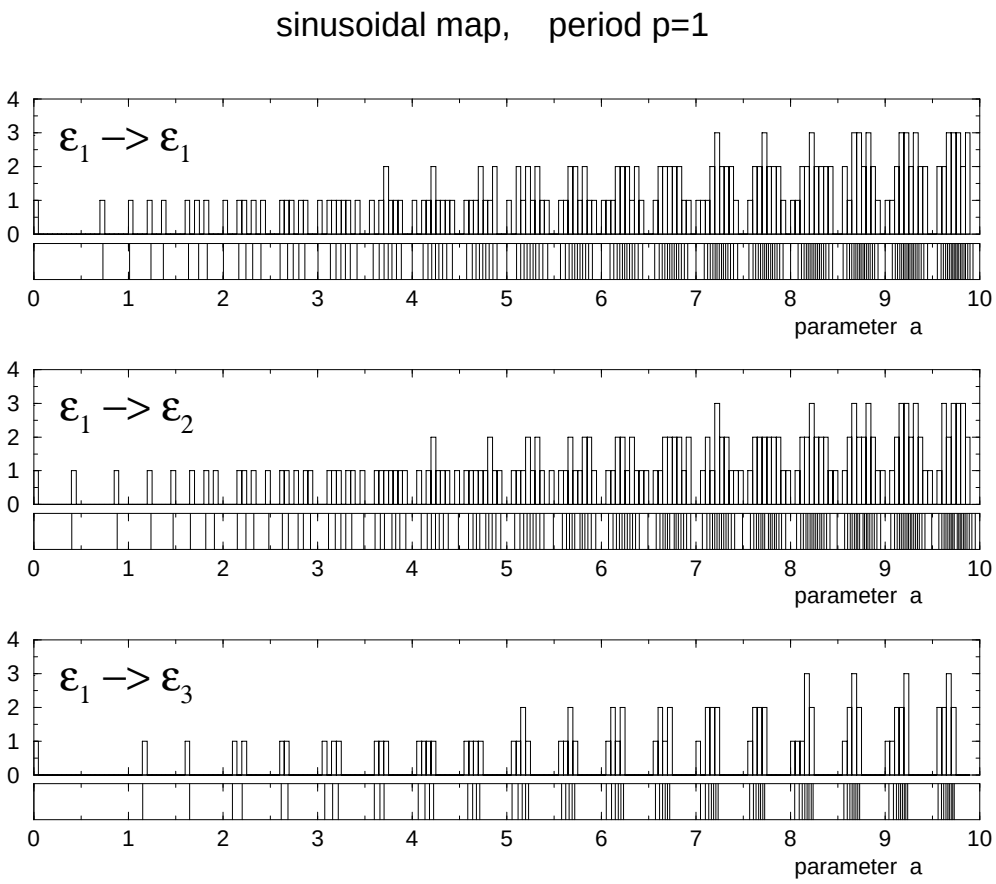

Figure 30: Distributions of the parameter values a corresponding to a Markov-partition of the sinusoidal map Eqn. (31) with a depth $p = 1$. The trivial fixed points of this map are $x = 0 \equiv 1$. For more details see Fig. 29. Because of the high density of the partitions in parameter space the distributions are given as histograms (bin width $\Delta x = 1/50$). The windows of the distribution at integer values of the parameter are due to a saddle-node bifurcation of the underlying map (see section 7.4.2).

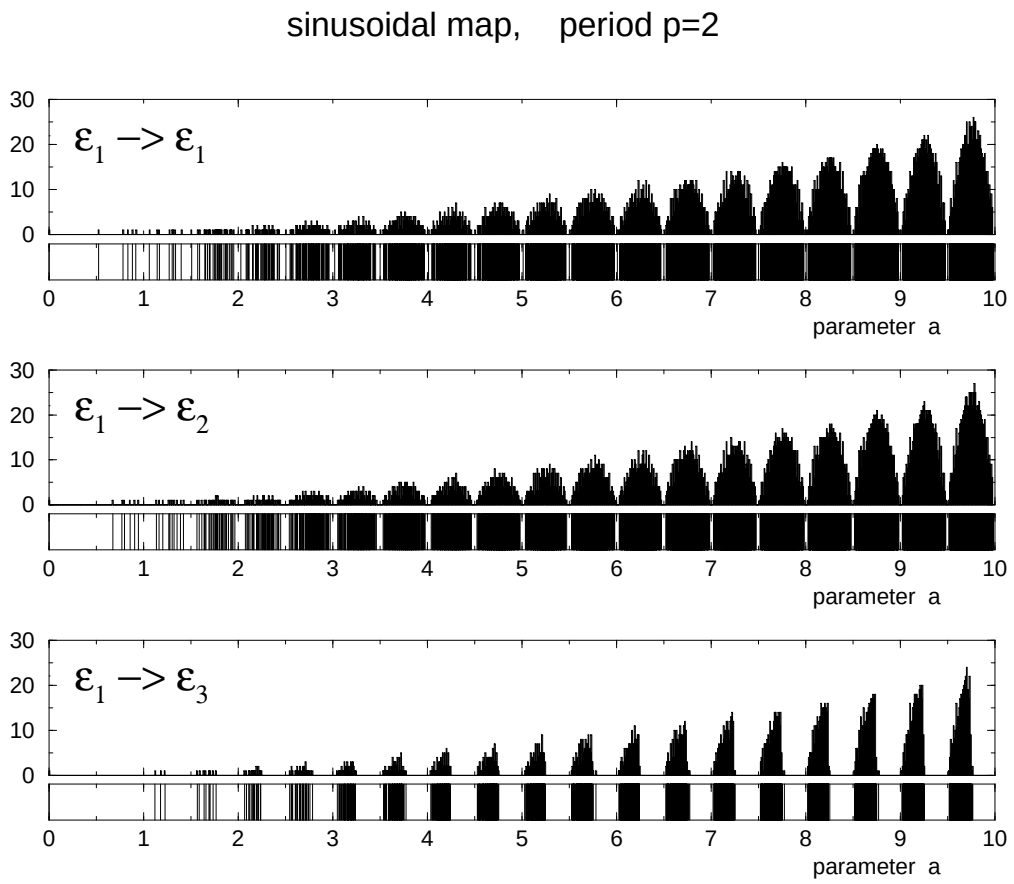

Figure 31: Distributions of the parameter values a corresponding to a Markov-partition of the sinusoidal map Eqn. (31) with a depth $p = 2$. Because of the high density of the partitions in parameter space the distributions are given as histograms (bin width $\Delta x = 1/50$).

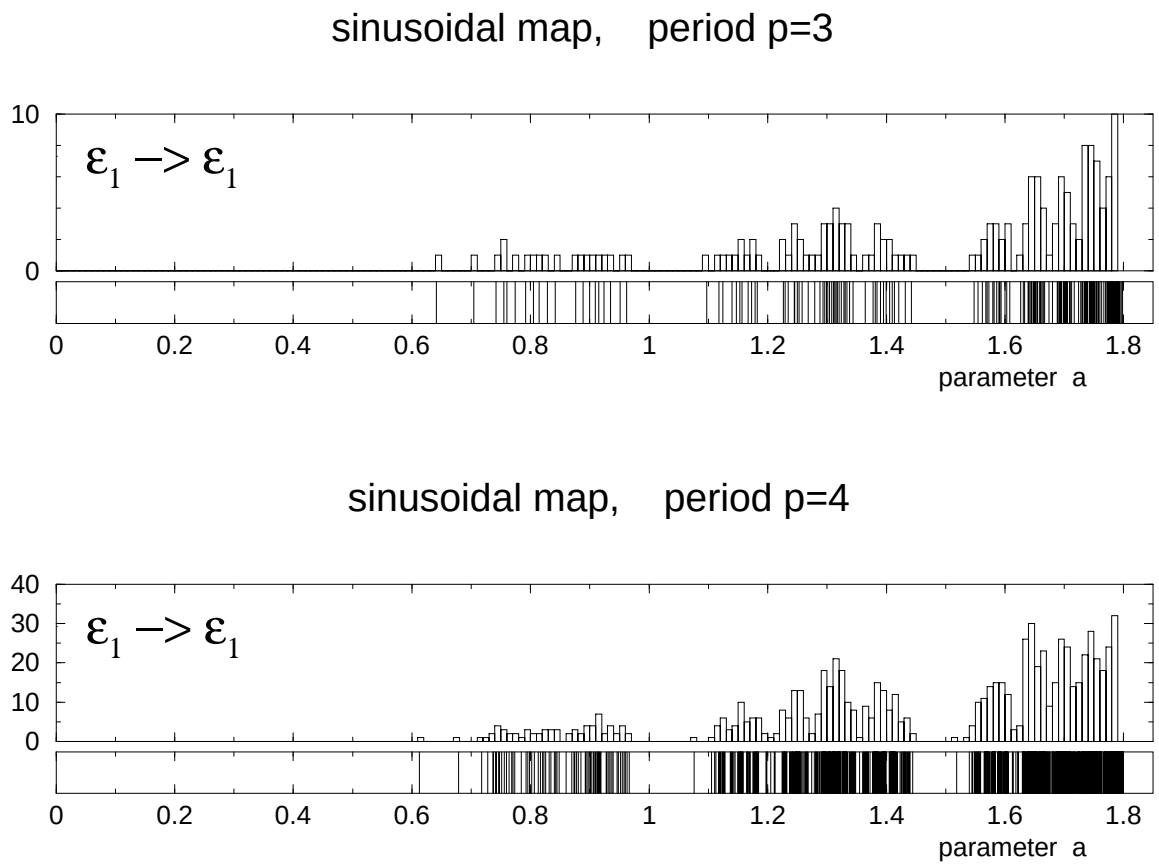

Figure 32: Distributions of the parameter values a corresponding to a Markov-partition of the sinusoidal map Eqn. 31 with a depth $p = 3$ and $p = 4$. Because of the high number of partitions for larger values of a the distribution is given only for the interval $a \in [0, 1.8]$ and or the transition $\epsilon_1 \to \epsilon_1$. The width of the bins is $\Delta x = 1/50$. For further details see Fig. 30

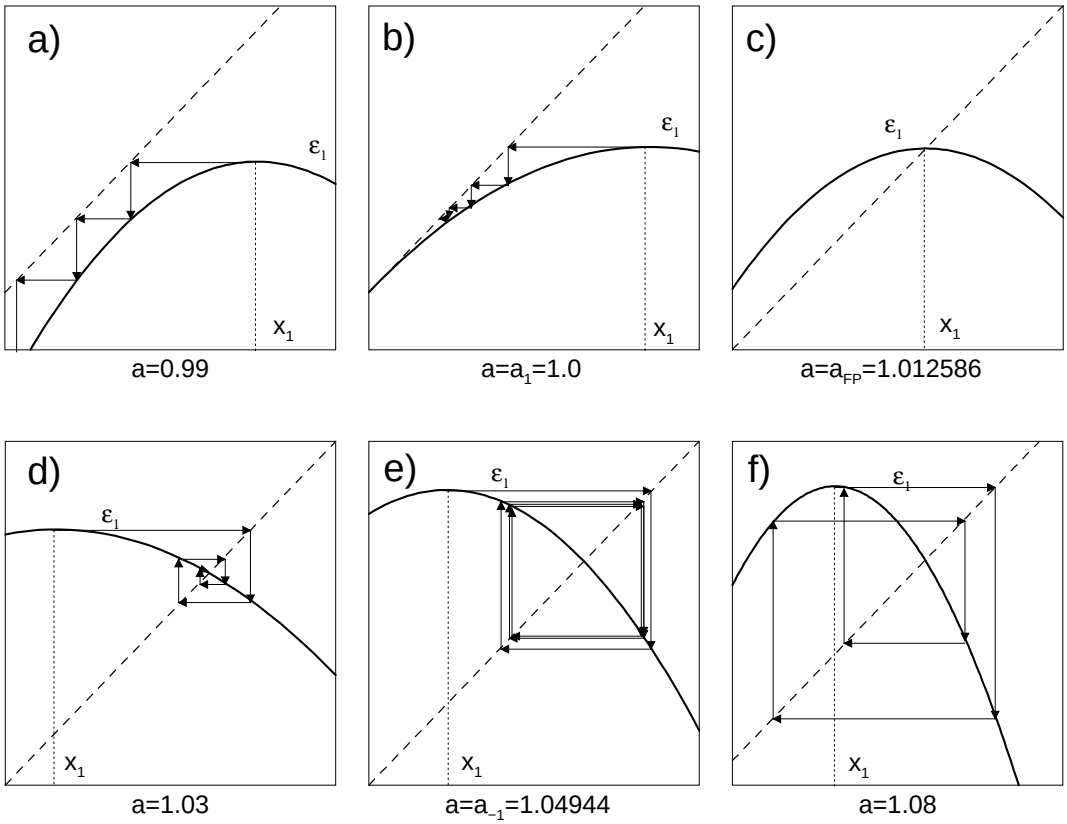

Figure 33: Sketch of the dynamics close to the saddle-node bifurcation at $a = a_1 = 1$. In the parameter interval $[a_1, a_{-1}]$ and close to the extremum the dynamics is dominated by the stable fixed point of the map, which attracts the trajectories starting at the extremum. It therefore prevents Markov-partitions except for the $\epsilon_1 \to \epsilon_1$-partition. This results in windows in the distribution of the partitions. (The dashed line is the function $y = x$).

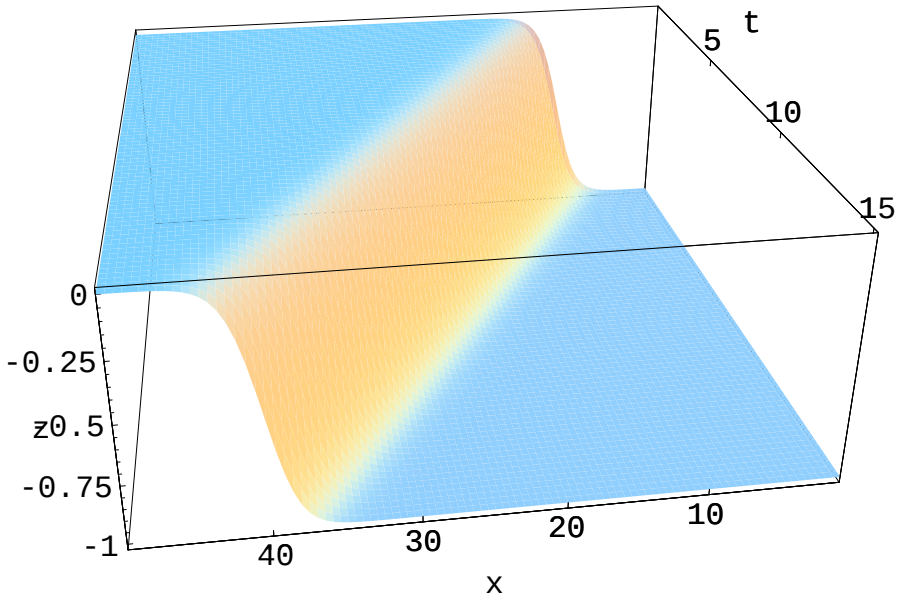

Figure 34: Time evolution of the Burgers system Eqn. (43) with the initial distribution $u_s(x,t) = -c/(1+\exp[c(x-x_o-ct)])$ with $c = 1.0$ and $x_o = 10.0$. The integration is performed on a spatial grid with $N = 100$ points and a time step $\Delta t = 0.2$.

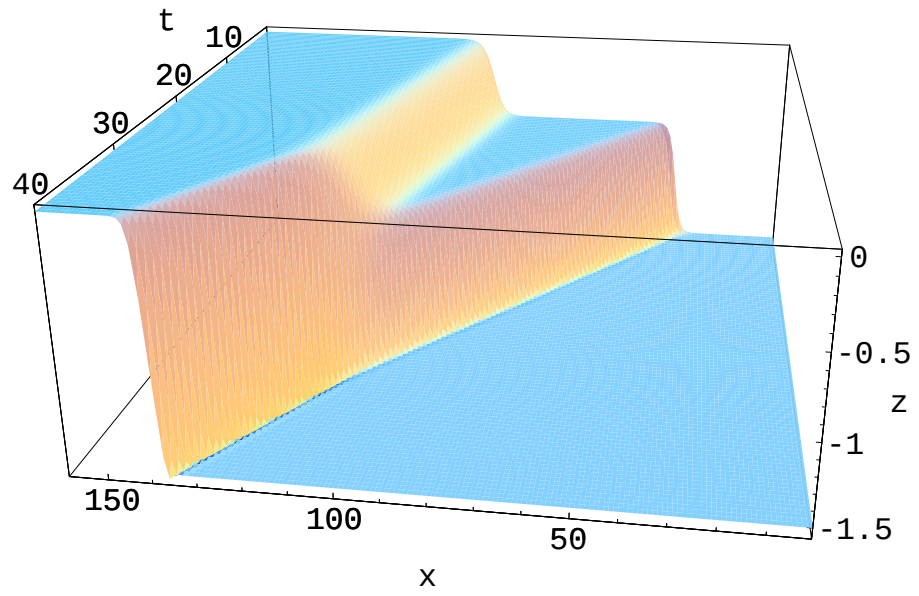

Figure 35: Time evolution of the Burgers system Eqn. (43). The initial distribution is a linear superposition $u_s(x,t) = -c_1/(1+\exp[c_1(x-x_1-c_1t)]) - c_2/(1+\exp[c_2(x-x_2-c_2t)])$ with $c_1 = 0.9$, $c_2 = 0.6$ and $x_1 = 34.0$, $x_2 = 93.5$. The integration is performed on a spatial grid with $N = 170$ points and a time step $\Delta t = 0.2$.

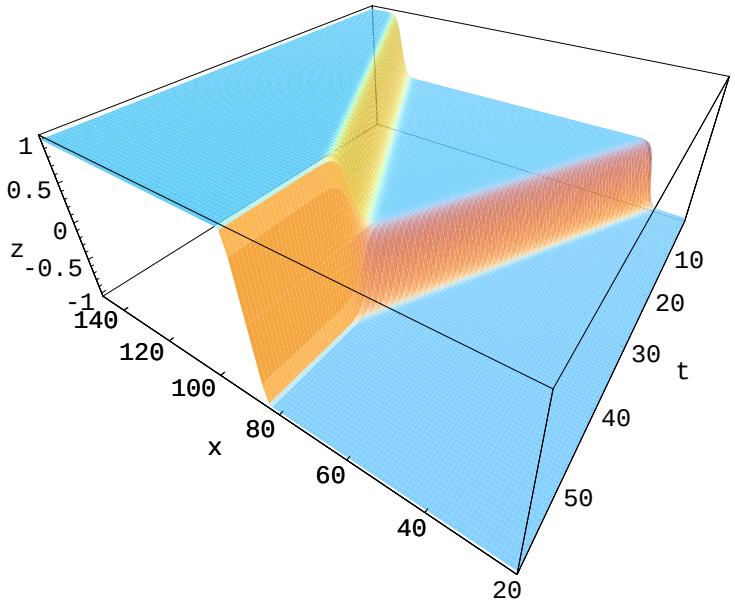

Figure 36: Time evolution of the Burgers system Eqn. (43). The initial distribution is a linear superposition $u_s(x,t) = -c_1/(1+\exp[c_1(x-x_1-c_1t)]) - c_2/(1+\exp[c_2(x-x_2-c_2t)])$ with $c_1 = 1.0$, $c_2 = -1.0$ and $x_1 = 34.0$, $x_2 = 136$. The integration is performed on a spatial grid with $N = 170$ points and a time step $\Delta t = 0.2$.

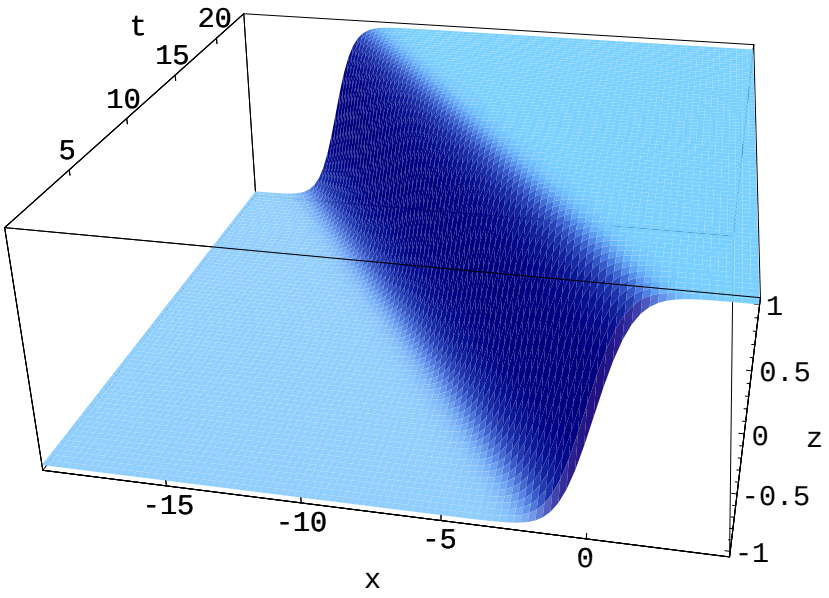

Figure 37: Time evolution of the Fitzhugh Nagumo system Eqn. (45). The initial distribution is given by $u = \tanh(x - at)$ Eqn. (46). The integration is performed on a spatial grid with $N = 100$ points and a time step $\Delta t = 0.2$.

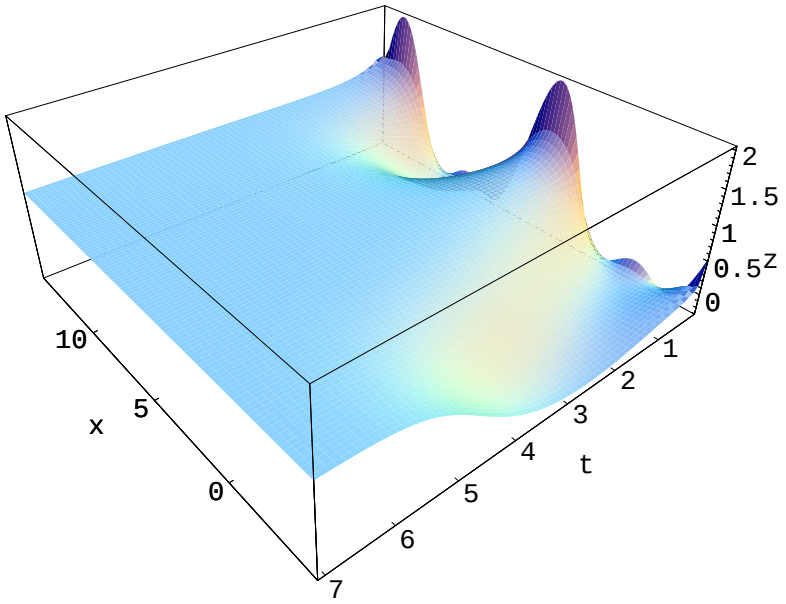

Figure 38: Time evolution of the real Ginzburg Landau system Eqn. (8.4.3). The initial distribution relaxes to the constant and stationary distribution $u(x,t) = 1$. The integration is performed on a spatial grid with $N = 100$ points and a time step $\Delta t = 0.1$.

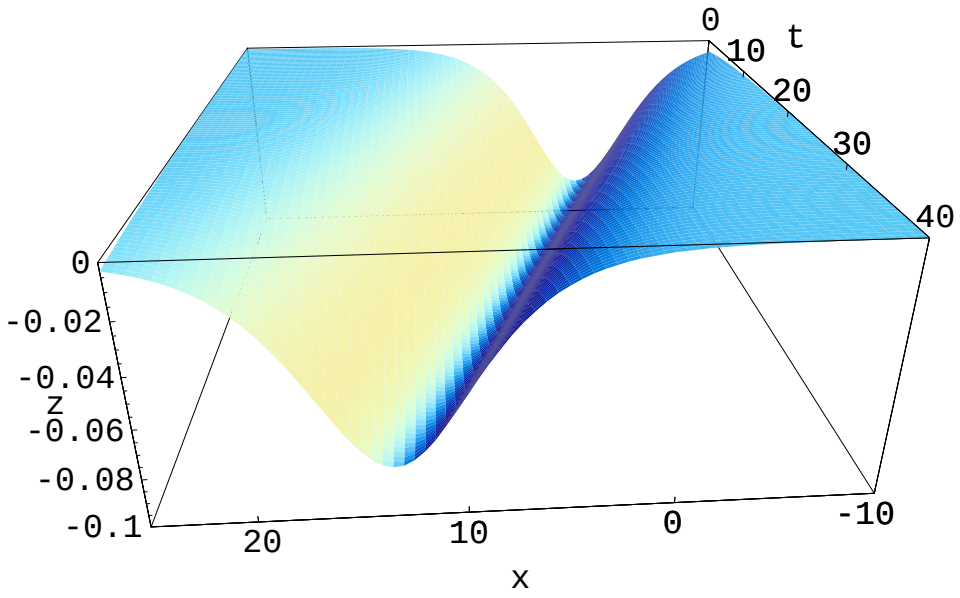

Figure 39: Time evolution of the Korteweg-de-Vries Eqn.(47). The initial condition is given by $u(x,t) = -\frac{q^2}{2}\frac{1}{\cosh^2[q(x-vt)]}$ (Eqn. (48)) with $q = 0.4$. Time evolution takes place on a spatial grid with $N = 120$ points and a time step $\Delta t = 0.1$.

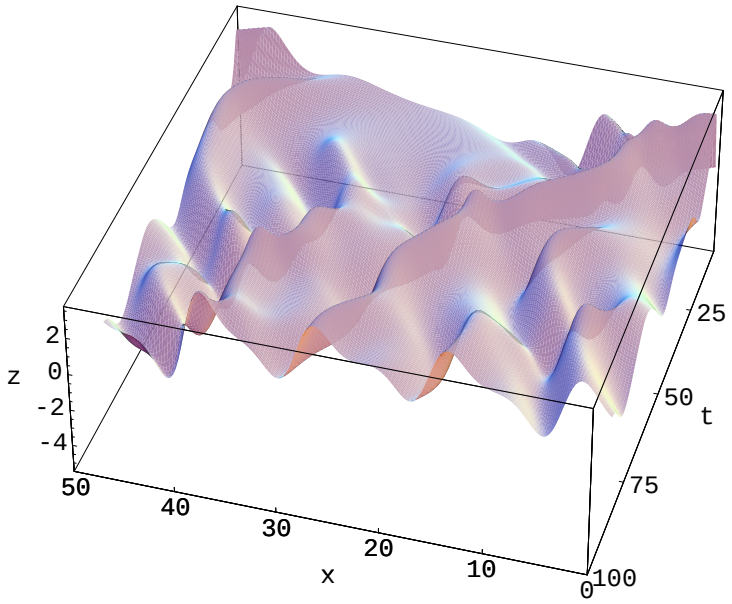

Figure 40: Time evolution of the Kuramoto Sivashinsky Eqn. (52) with a viscosity parameter of $\nu = 1.5$. The integration is performed on a spatial grid of $N = 170$ points and a time step $\Delta t = 0.1$.

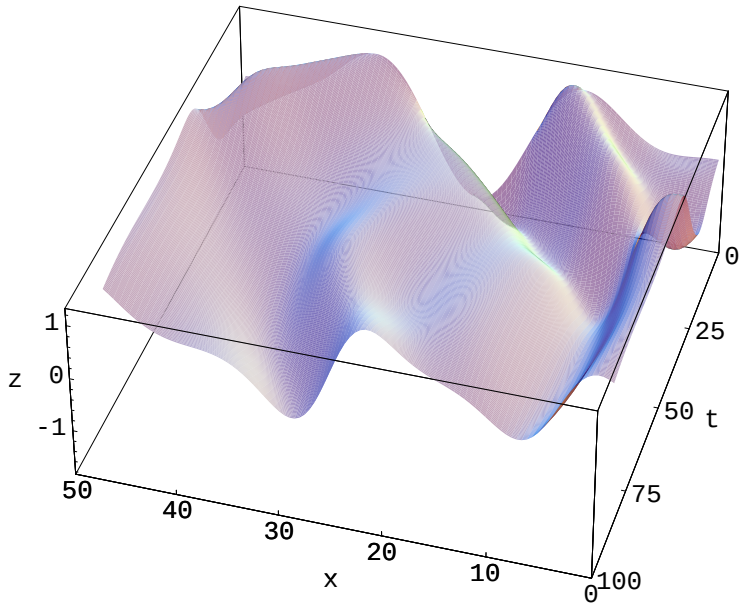

Figure 41: Time evolution of the Kuramoto Sivashinsky Eqn. (52) with a viscosity parameter of $\nu = 6.0$. The integration is performed on a spatial grid of $N = 100$ points and a time step $\Delta t = 0.1$.